DEVELOPMENT OF A SENSITIVE MID-INFRARED SPECTROMETER FOR THE STUDY OF COOLED MOLECULAR IONS

BY

MICHAEL W. PORAMBO

DISSERTATION

Submitted in partial fulfillment of the requirements
for the degree of Doctor of Philosophy in Chemistry
in the Graduate College of the
University of Illinois at Urbana-Champaign, 2015

Urbana, Illinois

Doctoral Committee:

Professor Benjamin McCall, Chair
Professor Martin Gruebele
Professor So Hirata
Professor Alexander Scheeline

ABSTRACT

The study of molecular ions is relevant to many areas of scientific interest. Mid-infrared laser spectroscopy functions as a useful tool for understanding the role of molecular ions in these areas. To this end, a broadly tunable mid-infrared difference frequency generation noise-immune cavity-enhanced optical heterodyne molecular spectroscopy (NICE-OHMS) system has been developed and characterized through rovibrational spectroscopy of methane. In addition, an attempt was made to use this spectrometer to probe molecular ions focused into an ion beam. Challenges inherent to laboratory molecular ion spectroscopy, such as quantum dilution at high internal temperatures and low ion number density, have been addressed through the development of an instrument that produces rotationally cooled molecular ions coupled to the highly sensitive spectroscopic technique NICE-OHMS. The instrument was first explored as an extension of an ion beam spectrometer by the integration of a continuous supersonic expansion discharge source for the production of the cooled molecular ions. Issues with the implementation led to the redesign of the instrument for spectroscopically probing a supersonic expansion discharge directly with NICE-OHMS. After implementing discharge modulation of the supersonic expansion source, spectra of rotationally cooled H_3^+ and HN_2^+ were acquired. This instrumental development and preliminary spectroscopy has paved the way for a new method for the sensitive spectroscopic study of cooled molecular ions that will aid further insight into these chemical species in many fields.

To Mom and Dad, for their love and support.

ACKNOWLEDGMENTS

I would first like to acknowledge and thank Professor Ben McCall for his mentorship, teaching, and advice throughout my graduate studies at the University of Illinois. Ben has been a patient and dedicated advisor, and I owe a lot to him. Not only has he taught me about spectroscopy, but he has taught me how to solve problems, work with others, and think scientifically. I would also like to thank him and his wife, Birgit, for being very gracious in opening up their home to the research group on many occasions, and for showing us that they cared about our success and welfare.

I also thank the other members of my committee: Professor Martin Gruebele, Professor So Hirata, and Professor Alexander Scheeline. They have also helped me throughout the PhD program as teachers/collaborators and as consultants with many keen insights on problems I encountered while performing experiments.

I am also deeply indebted to the many graduate students, undergraduate students, and postdocs I have had the privilege of working with over the years. I started research by working with Manori Perera, who was gracious enough to work with such a new student, and is an excellent teacher. Lauren Moore was very helpful in showing me how to align optics on my first project in the group. Although my time with Brian Tom was very short, I am indebted to him for his advice and instruction during a long multi-day experiment. It was fun working on the project with Bill Evans, having many great conversations about science. Andrew Mills and Brian Siller have been superb mentors to me as a junior graduate student, really instilling in me how to solve problems; I feel really lucky having worked with them. Holger Kreckel was also a good mentor to me in the early days. While I never had the opportunity to work directly with Kyle Crabtree, he was a mentor to me as an office mate who taught me a lot about how to be a successful graduate student. I am really thankful to Carrie Kauffman, a fellow alum of Lebanon Valley College, who

was my host during grad student recruitment weekend and a good friend throughout the first years of graduate school.

I have also had the honor of working with a lot of great students as a more senior graduate student. I really appreciate the dedication of then-undergraduates Joe Puhr and Craig Riccardo during some difficult moments on the project. I thank Jessica Pearson for all of the hard work and dedication she put into our experiments, and it was great to be lab partners with her. I also thank Courtney Talicska, who has also worked hard on the project and has made some of the toughest days of research downright fun.

I also thank the other graduate students in the McCall group during my time there, for all of the help and support they have given in practice talks, group meetings, and in many other ways. Brian Brumfield, Nick Indriolo, Jacob Stewart, David Friday, James Hodges, Brad Gibson, Adam Perry, Haochen Ke, Scott Dubowsky, Nicole Koeppen, Charlie Markus, and Dave Woon have also been excellent people to work with in the group, and I am grateful for the opportunity to work with them and to get to know them.

I would also like to thank Dr. Bob Springborn and Carolyn Springborn for their generous financial support through the Springborn Fellowship. I feel really honored to have been a part of this program, and it was an absolute pleasure to meet and talk with the Springborns when they came in to town. Their generosity has been inspiring. Likewise, I thank the NASA Earth and Space Science Fellowship program for providing financial support through the second half of my PhD studies.

Outside of the University of Illinois, I thank many people for their support in my studies. I would like to thank the teachers and mentors I had in college and high school for instilling in me an interest in science and the encouragement to pursue graduate studies. I especially thank my two high school chemistry teachers, Anthony Thoman and John Brenneman, and my undergraduate advisor, Dr. Anderson Marsh, for their mentorship and dedicated teaching. Finally, I would like to thank my family and friends for the wonderful and helpful support they have given me during the many years I have been in graduate school. I would especially like to acknowledge and thank my girlfriend, Colleen Ackermann, for the tremendous support and love she has given me throughout the preparation of my dissertation. I am very grateful for her constant encouragement. I also especially thank my siblings, Mark and Laura, and Mom and Dad for being a constant source of

support and encouragement. Thank you all; I could not have done it without you.

June 23, 2015

AMDG

TABLE OF CONTENTS

CHAPTER 1

INTRODUCTION

1.1 Molecular Ions in the Gas Phase

The properties and reactions of molecular (or polyatomic) ions are an active area of research in many branches of chemistry and physics. The gas phase properties and reactions of these ions in particular play important roles in various environments of scientific interest. For example, molecular ions significantly contribute to the chemistry of Earth's atmosphere [1, 2]. In addition, molecular ions play roles in combustion reactions as intermediates and products [3,4]. Molecular ions are also studied as the drivers of gas phase chemistry in the interstellar medium [5]. In the low density and temperature of the interstellar medium (10^2 and 10^3 cm^{-3}, 100 and 10 K for diffuse and dark clouds, respectively [6]), reactions between gaseous molecular ions and neutral molecules make up an entire chemical network in these regions [7]. Finally, there is interest in fundamental physical properties of exotic molecular ions, such as CH_5^+. The chemical structure and intramolecular dynamics of this molecular ion have evaded understanding for some time [8], but recent advances have begun to acquire useful understanding [9].

In many of these areas, spectroscopy is a useful tool to obtain data on these ions and gain scientific insights into their properties and chemical behavior. In certain circumstances (such as in studying the chemistry of molecular ions in molecular gas clouds light-years away), the extreme stand-off capability of spectroscopy makes it the only tool available! Spectroscopy can be useful for composition and concentration studies of molecular ions, and it can also be used for studies of the physical conditions of the environment of the sample. For example, H_3^+ [10], and OH^+, H_2O^+, and H_3O^+ [11] spectral data have been used to determine the rate of cosmic-ray ionization in interstellar environments. In many instances, laboratory spectral data is needed

to understand data obtained through astronomical observation or field measurements, and laser spectroscopy in particular offers advantages due to the high sensitivity and resolution it provides.

For an example of the utility of laboratory molecular ion spectroscopy, the interstellar detection of protonated formaldehyde, H_2COH^+, was greatly aided by spectra obtained in the laboratory. Protonated formaldehyde was hypothesized to be integral in the formation and destruction mechanism of interstellar formaldehyde [12], which had already been detected [13]. Laboratory infrared spectra of H_2COH^+ were used to obtain rotational transitions indirectly [14], and then refined with millimeter-wave spectroscopy [12]. With these accurate transitions acquired in the laboratory, protonated formaldehyde was positively detected in several locations of the interstellar medium [15]. This dependence on laboratory spectroscopy for interstellar detection extends to other molecular ions.

1.2 Challenges and Methods of Study

Many challenges, however, are inherent in laboratory molecular ion spectroscopy, and methods have been developed over the past few decades to overcome these challenges. These challenges include low ion number density, discriminating between ion and neutral spectral signals in a sample, and probing weak signals at high internal temperature.

In many gas discharge sources used to produce molecular ions for laboratory study, only a fraction of the precursor gas is ionized. Because only a fraction of the precursor is ionized, a larger sample of neutral molecules will be present in the sample. These may interfere with the weaker transition signals from the molecular ions; a way to separate or determine which signals come from which type of chemical species may be needed. One powerful method to overcome the problem of *ion-neutral discrimination* is velocity modulation spectroscopy (VMS) [16]. This effective method produces molecular ions in an AC glow discharge. Precursor gas flows through the discharge cell and is ionized between two high voltage electrodes which alternate in polarity at a given frequency. In this system, the absorption signals of the ions continuously Doppler shift in a periodic fashion at the frequency of the AC discharge. These modulating signals can be detected with a lock-in amplifier,

discriminating these signals from absorption signals due to neutral molecules. This method has been used successfully to acquire spectra of many molecular ions [16–20]. However, VMS by itself may not have the sensitivity to detect a *low number density* of ions in the source. With most of the gas remaining neutral during the discharge, a small number density of the sample is ionized, potentially resulting in a very weak signal. To surmount the issue of low number density, spectroscopic methods that work to increase the signal-to-noise ratio are also used for molecular ion spectroscopy. Cavity-enhanced techniques such as cavity ring-down spectroscopy (CRDS) [21, 22] and cavity-enhanced absorption spectroscopy (CEAS) [23–25] have increased sensitivity over direct absorption spectroscopy by increasing the optical pathlength through the sample by adding an optical cavity around it. In effect, the pathlength is increased hundreds or even thousands of times, depending on the reflectivities of the mirrors. Another way to increase the sensitivity of detection has been accomplished by decreasing the technical noise in the detected signal by frequency modulation spectroscopy (FMS) [26]. In this setup, the laser source is phase modulated, encoding the detected signal at a high RF frequency, which is less susceptible to $1/f$ noise. Very low noise with this system is possible, in principle only limited by shot noise.

These two techniques of enhancing the sensitivity have been combined in a method known as noise-immune cavity-enhanced optical heterodyne molecular spectroscopy (NICE-OHMS) [27, 28]. In NICE-OHMS, the sidebands caused by the FMS are spaced from the carrier at a frequency equal to a multiple of the optical cavity's free spectral range (FSR), allowing all laser modes to be coupled into the cavity. Thus, shot-noise-limited detection limits are combined with cavity enhancement for very large sensitivity (the highest sensitivity so far with this technique for spectroscopy has been reported as 5.6×10^{-12} cm^{-1} Hz$^{-1/2}$ [29]). This technique has been applied to the study of molecular ions in an ion beam in the near-infrared [30] and of a positive column discharge cell in the mid-infrared [20], where sensitivities of 2×10^{-11} cm^{-1} Hz$^{-1/2}$ and 9.8×10^{-10} cm^{-1} Hz$^{-1/2}$ were obtained, respectively. This technique is very powerful, then, for overcoming the issue of low number density in a molecular ion sample.

The final issue of *high internal ion temperature* can be overcome with techniques for lowering the temperature. Lower temperature samples will have increased signal, as fewer energy levels are populated (i.e., the partition func-

tion is lower), preventing the spectrum being spread out and "diluted" over many energy levels. A high resolution low temperature spectrum will then have fewer, but more intense lines than a high temperature spectrum. Low temperature molecular ion spectroscopy has been done with liquid nitrogen cooled positive column cells [8, 16, 20, 31–34] and hollow cathode discharge cells [35, 36]. However, supersonic expansion sources have the capability to obtain very low temperatures of molecules and clusters ($\sim$ 5 K [37]). Several types of supersonic expansion discharge sources (combining a supersonic expansion source with some electric discharge mechanism) have been used to obtain samples of low temperature molecular ions [38–44]. In both pulsed and continuous sources, the precursor gas is discharged while expanding from high pressure into vacuum through a small orifice (a pinhole or a slit). This adiabatically cools the ions that are formed in the discharge, lowering the partition function and lowering the sensitivity needed to observe spectral lines.

One advantage of a supersonic expansion source is that the expanded sample can be skimmed and focused into an ion beam. Ion beam spectroscopy in its own right possesses useful qualities for molecular ion spectroscopy. Like velocity modulation spectroscopy, an ion beam can be used to discriminate between ions and neutral molecules in the sample. In this case, the ions can be manipulated and physically separated from any neutral molecules present in the sample through the use of electrostatic ion optics and steering devices; the neutral molecules will not be affected by these electrostatic components. Very narrow spectroscopic linewidths can be obtained from ions in an ion beam due to the effect of kinematic compression (the high velocity ions have a narrow velocity distribution). The main disadvantage of an ion beam spectrometer is that a very low sample of ions are probed. Nevertheless, several ion beam spectrometers have been implemented with laser spectroscopy [30, 45–49]. One of the subjects of this dissertation regards attempts at integrating a supersonic expansion discharge source to the NICE-OHMS/velocity modulation ion beam spectrometer reported in [30], culminating in an instrument that combines all of the methods discussed to overcome the challenges inherent in molecular ion spectroscopy.

1.3 This Work

This dissertation will present original work on the development of a sensitive laser spectrometer for the study of cooled molecular ions in the mid-infrared region of the electromagnetic spectrum, using the aforementioned methods. The spectroscopy system of [30] was altered from near-infrared to mid-infrared operation. The description and characterization of this broadly tunable, mid-infrared NICE-OHMS spectrometer that was coupled to the ion beam instrumentation is given in Chapter 2. Characterization of the ion beam in the mid-infrared was then attempted on the simple molecular ions H_3^+ and HN_2^+ in the same hot ion source described in [30], which is discussed in Chapter 3. The interfacing of the supersonic expansion discharge source to the ion beam instrument will be discussed in Chapter 4. This chapter will include, for example, the design of beam skimmers, the required rearrangement of vacuum chambers in the system, initial supersonic expansion tests in this spectrometer, and issues with the source in this particular arrangement. Attempted preliminary detection of H_3^+ and HN_2^+ in the source with double-pass frequency modulation spectroscopy and cavity ring-down spectroscopy will also be discussed in this chapter. Chapter 5 will present the final rearrangement of the system for direct NICE-OHMS on the supersonic expansion discharge source and preliminary spectroscopy of H_3^+ and HN_2^+ in the system. Finally, Chapter 6 will summarize the work discussed in this dissertation and offer brief proposals for future work in this system.

CHAPTER 2

BROADLY TUNABLE MID-INFRARED NOISE-IMMUNE CAVITY-ENHANCED OPTICAL HETERODYNE MOLECULAR SPECTROMETER

Noise immune cavity enhanced optical heterodyne molecular spectroscopy (NICE-OHMS) is the most sensitive direct absorption technique developed. First reported by Ye et al. [27, 28], this technique combines the increased absorption due to path length enhancement of cavity enhanced absorption spectroscopy [24, 50] with the low noise of frequency modulation/heterodyne spectroscopy [26]. Not only does NICE-OHMS allow for high sensitivity detection, but it can also probe sub-Doppler saturation features. Rigorous theoretical analyses of the NICE-OHMS signal, both Doppler-broadened and sub-Doppler, have been reported in several works [51, 52]. Variants of NICE-OHMS setups have also been developed, such as wavelength-modulated NICE-OHMS [53] and the ion-specific velocity-modulation NICE-OHMS [19].

Additionally, NICE-OHMS has evolved through its integration with different laser systems. Nd:YAG [28], Ti:sapphire [54], laser diode [55], and fiber-laser [56, 57] based NICE-OHMS spectrometers have been built, but little work has been done on NICE-OHMS in the mid-infrared (3–10 μm) spectral region. To our knowledge, the only setup reported in this wavelength range is based on a quantum cascade laser (QCL) [58]. QCLs, however, suffer from limited tunability.

Other laser systems offer broader tunability in the mid-infrared. Difference frequency generation (DFG) produces a beam at the frequency difference between two input lasers using a nonlinear crystal, with the tunability only limited by the most tunable of the lasers and the transparency of the crystal. Similarly, continuous wave optical parametric oscillators (cw OPOs) emit mid-infrared radiation tunable from ∼2.3 to 4.6 μm. To extend its tunability

This chapter is adapted and reprinted with permission from Porambo, Michael W.; Siller, Brian M.; Pearson, Jessica M.; McCall, Benjamin J. 2012 Optics Letters 37(21) 4422-4424

in the mid-infrared, we have integrated NICE-OHMS with a DFG setup, enabling use of this unique, high-sensitivity spectroscopy continuously in the ∼3–5 μm region.

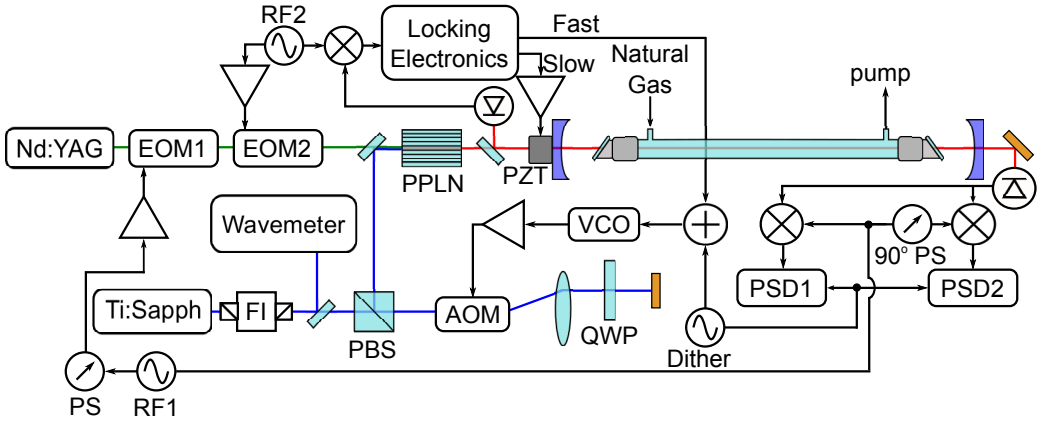

Figure 2.1: (Color online) Experimental Layout. FI: Faraday isolator; PBS: polarizing beam splitter; AOM: acousto optic modulator; QWP: quarter wave plate; VCO: voltage controlled oscillator; EOM: electro-optic modulator; PZT: piezoelectric transducer; RF: radio frequency generator; PS: phase shifter; PSD: phase sensitive detector; PPLN: periodically poled lithium niobate crystal; △: RF amplifier.

The experimental setup is illustrated in Fig. 2.1. A ring Ti:sapphire laser (Sirah-Matisse TS) whose wavelength is measured with a Bristol 621A-IR wavemeter is sent through a double-pass acousto-optic modulator (AOM) [59] that is resonant at ∼85 MHz, which redshifts the laser by ∼170 MHz and results in no change to the beam pointing upon altering the AOM driving frequency. A Nd:YAG laser (1064 nm) is passed through two electro-optic modulators (EOM). The first EOM (New Focus 4003, MgO:$LiNbO_3$) is resonant at ∼112.5 MHz and generates sidebands at the cavity free spectral range (FSR) used for heterodyne detection; the modulation index is 0.79. The second EOM (ThorLabs EO-PM-NR-C1, MgO:$LiNbO_3$) produces additional sidebands at ∼6 MHz, which are used to generate the error signal in a Pound-Drever-Hall locking scheme [60]. The processed error signal is split into two correction pathways. Slow corrections (up to 70 Hz) are sent to the cavity piezoelectric transducer (PZT), while fast corrections (up to 60 kHz) are sent to the voltage controlled oscillator (VCO) of the AOM. The Ti:sapphire and Nd:YAG are combined in a periodically poled lithium niobate (PPLN) crystal, which results in a mid-infrared beam at the differ-

ence between the frequencies of the two input lasers. This beam can be tuned between 2.8 and 4.8 μm by tuning the Ti:sapphire laser frequency (for NICE-OHMS, the wavelength-dependent reflectivity of the optical cavity mirrors limits the tuning range to 3.0–3.4 μm, but multiple mirror sets could be used to extend the tunability to 2.8–4.8 μm).

The mid-IR DFG is then coupled into a cavity with a finesse of $\sim$300. The cavity transmission is captured on a 120 MHz bandwidth InSb detector (Kolmar). Then, the signal is split and demodulated with two RF mixers that are both referenced to the heterodyne RF frequency, but are 90° out of phase with one another to separate the absorption and dispersion signals.

The sample cell used in this work was equipped with turbomolecular pumps and operated as a flow cell. Natural gas was leaked into the cell from the building supply. Light was coupled through CaF_2 Brewster windows on either end of the cell, which was isolated from the cavity mirrors to reduce vibrational noise.

Two different modulation techniques were performed during this work. The first was frequency modulated (fm)-NICE-OHMS. The second was wavelength modulated (wm)-NICE-OHMS, in which a 50 Hz dither was applied to the AOM VCO to induce a peak-to-peak modulation of 1.7 MHz, and phase sensitive detectors (that is, lock-in amplifiers) demodulated the resulting signal.

Demonstration and characterization of the DFG NICE-OHMS system was conducted by ro-vibrational spectroscopy of methane in natural gas. The heterodyne phase was adjusted such that one mixer output would be approximately tuned to the absorption phase and the other approximately tuned to the dispersion phase. A representative Doppler-broadened spectrum of a methane ro-vibrational transition (containing the absorption and dispersion channels) is shown in Fig. 2.2.

A fit equation based on Equation 1 of Ref. [61] was used to fit the data:

$$\begin{aligned} S = y_0 + A\Big[& \left(\chi_{-1}^{abs} - \chi_1^{abs}\right)\cos\theta \\ & + \left(2\chi_0^{disp} - \chi_1^{disp} - \chi_{-1}^{disp}\right)\sin\theta\Big] \end{aligned} \tag{2.1}$$

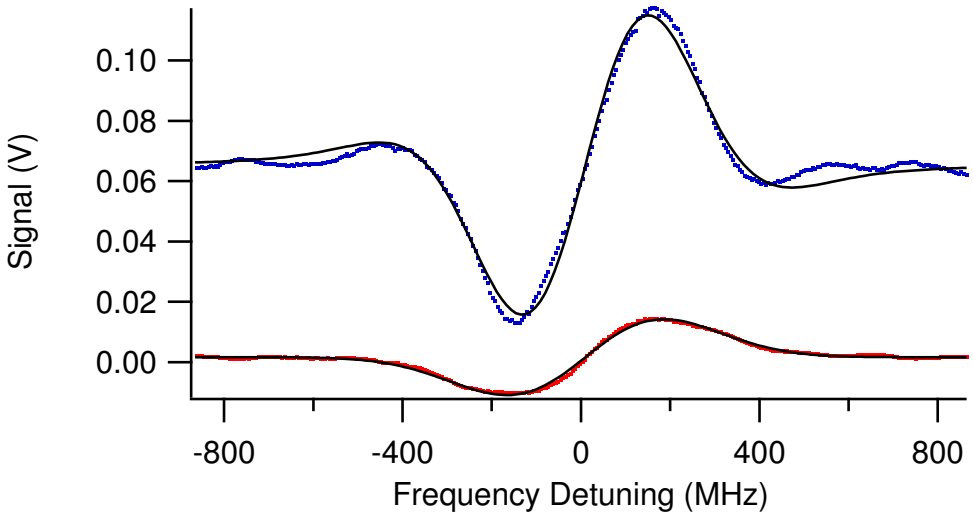

Figure 2.2: (Color online) Doppler-broadened fm-NICE-OHMS dispersion (top) and absorption (bottom) signals from the P(9) A_2 transition of the ν_3 fundamental band of CH_4 at a pressure of $\sim 6\times10^{-5}$ Torr. Raw data are given as dots, fits to the data are given in solid curves. The dispersion curve is offset vertically for clarity.

where

$$\chi_j^{abs} = \frac{1}{\sqrt{1+G}} e^{-x^2} \tag{2.2}$$

$$\chi_j^{disp} = \frac{2}{\sqrt{\pi}} e^{-x^2} \int_0^x e^{t^2} \mathrm{d}t \tag{2.3}$$

and $x = \frac{2\sqrt{\ln 2}(\Delta\nu + j\nu_m)}{\delta\nu}$. Furthermore, θ is the heterodyne detection phase, A is the amplitude, G is the saturation parameter, y_0 is an offset parameter, $\Delta\nu = \nu - \nu_0$ is the detuning of the source frequency ν from the transition line center ν_0, ν_m is the heterodyne modulation frequency, and $\delta\nu$ is the transition line width (FWHM). A global analysis fit was performed on both channels simultaneously with θ, ν_m, G, and A constrained to be equal for both detection channels and y_0 allowed to float independently. ν_m is held fixed at 112.5 MHz.

The fractional noise equivalent absorption (NEA) is calculated to be $\sim 1\times10^{-6}$ cm^{-1} $Hz^{-1/2}$ and $\sim 2\times10^{-7}$ cm^{-1} $Hz^{1/2}$ for the dispersion and absorption detection channels, respectively. Low frequency noise is observed in the baseline, which appear to be phase-dependent; this noise is more pronounced in the dispersion channel than in the absorption channel. This noise is sus-

pected to be from etalons in the optical setup, residual amplitude modulation due to the heterodyne EOM, or a combination of these. Both of these effects can be phase-dependent [62, 63], which may explain why one channel contains more noise. Attenuation of the absorption signal due to optical saturation is observed, consistent with published theoretical descriptions [51]. The saturation parameter was determined to be ∼70 by the global fit to the data.

Not only does this optical saturation attenuate the Doppler-broadened signal amplitude [51], but it also leads to sub-Doppler Lamb dips. The Lamb dips are the result of two modes of the phase-modulated light (a forward-propagating mode and a counter-propagating mode) interacting with the same velocity group of molecules. Lamb dips are observed in the Doppler-broadened spectrum at the line center for dispersion signals and at multiples of half the heterodyne frequency for both dispersion and absorption. As generally the center dispersion Lamb dip is the strongest of the Lamb dips, the scan parameters were varied to maximize the amplitude of this Lamb dip. Optimization of the center dispersion Lamb dip was aided by the fact that no Lamb dip at line center should be observed in the absorption detection phase; thus, the heterodyne phase was varied until the center Lamb dip in one detection channel was completely eliminated. An optimized center dispersion Lamb dip is shown in Fig. 2.3.

The sub-Doppler signals were obtained using wm-NICE-OHMS, as described earlier. Wavelength modulation broadened the sub-Doppler lineshape sufficiently to observe the signal while taking ∼350 kHz steps on the DFG (by tuning the Ti:sapphire laser). This detection scheme also results in higher sensitivity than that of fm-NICE-OHMS. With wm-NICE-OHMS, the NEA is calculated to be 6×10^{-9} cm^{-1} Hz$^{-1/2}$, which is about 250 times the shot noise limit. This value is about a factor of 60 less sensitive than what was observed for the QCL-based NICE-OHMS spectrometer [58].

Several issues seem to impact the ultimate sensitivity and performance of the spectrometer. Etalons formed between the transmission detector and the optical cavity and between the optical cavity and the DFG PPLN crystal decrease the sensitivity. For the Doppler-broadened scans, these etalons were significantly mitigated by using heat guns across the respective beam paths and averaging for ∼1 s per point, as accomplished in [64]. Furthermore, the lineshapes of the signals are somewhat distorted by drifts in the frequencies

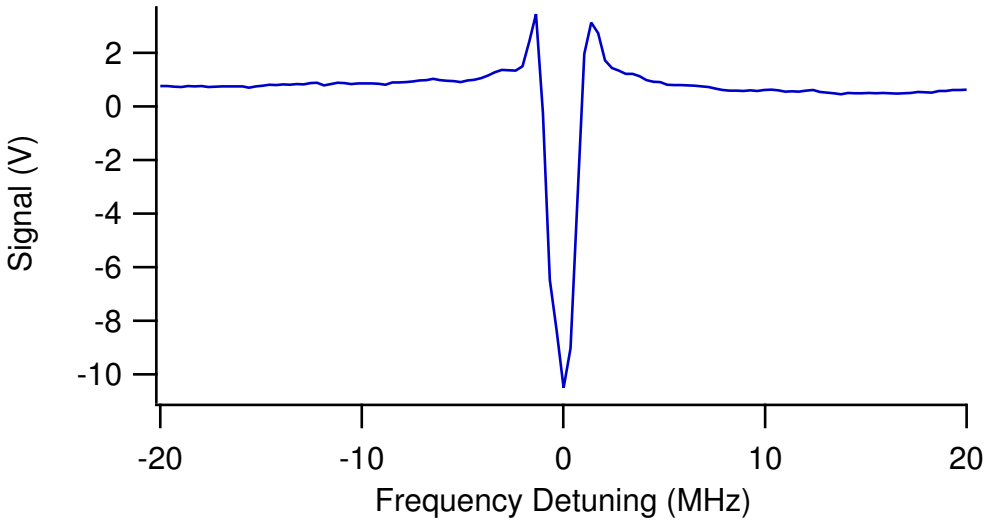

Figure 2.3: (Color online) Center dispersion Lamb dip of the P(12) A_1 transition of the ν_3 fundamental band of CH_4 observed at a pressure of $\sim 6 \times 10^{-5}$ Torr.

of the pump and signal lasers of the DFG process. To prevent this drifting in the future, we plan to stabilize the frequencies of both lasers by locking the Nd:YAG to an iodine hyperfine transition and the Ti:sapphire to an optical frequency comb.

In summary, we present the first broadly tunable NICE-OHMS spectrometer in the mid-infrared. Coherent mid-infrared radiation is produced through difference frequency generation with a Nd:YAG laser and a tunable Ti:sapphire laser combined in a periodically poled lithium niobate crystal. The instrument was characterized and optimized by probing ro-vibrational transitions of methane present in natural gas. Doppler-broadened fm-NICE-OHMS absorption and dispersion signals were acquired and fit. Sub-Doppler signals were observed using wm-NICE-OHMS. We have recently integrated this DFG NICE-OHMS system to the fast ion beam spectrometer described in [30]. Additionally, our research group has completed development of a similar mid-infrared NICE-OHMS system based on a cw OPO [20]. Both of these systems will be used to study ro-vibrational spectra of molecular ions.

The authors wish to thank Craig Riccardo and Joe Puhr for their help in acquiring spectra for this study. This work has been supported by the National Science Foundation (PHY-08-55633), the NASA Laboratory Astrophysics program (NNX08AN82G), and a David and Lucile Packard Fellow-

ship. M.W.P. has been supported by a Robert C. and Carolyn J. Springborn Fellowship from the University of Illinois.

CHAPTER 3

MID-INFRARED ION BEAM SPECTROSCOPY

3.1 Introduction

Spectroscopy in the mid-infrared is very advantageous, as many strong, fundamental rotation-vibration transitions of molecules and molecular ions occur in this part of the electromagnetic spectrum. With this in mind, the mid-IR DFG NICE-OHMS spectrometer described in Chapter 2 was coupled to the ion beam system described in [30]. This instrument would possess the advantages of an ion beam spectrometer (such as ion-neutral discrimination and mass information) applied to rovibrational spectroscopy.

Eventually, the goal was to integrate the continuous supersonic expansion discharge source into the ion beam system and perform mid-infrared spectroscopy on a skimmed ion beam from this source. However, as a preliminary first step, the mid-infrared spectrometer would be tried on the simple cold cathode source described in [30]. This source was already well-used, and trying this source first would allow optimization of the ion beam measurements in the mid-infrared before addressing the need to skim a supersonic expansion. The preliminary work would involve acquiring the spectra of H_3^+ and HN_2^+, two molecular ions that have been well-studied in the mid-infrared and are relatively easy to produce. Once these spectra were optimized, the source would be exchanged for the supersonic expansion source.

However, spectra of these ions were not obtained. The sensitivity and stability issues with the instrument precluded the acquisition of lines from these ions within a reasonable amount of time. This non-detection will be discussed.

3.2 Ion Beam Spectrometer

The ion beam spectrometer is described in [30] (reprinted in Appendix A). A brief description is given here.

The ion source is mounted in the first chamber of the system. Ions produced in the source are extracted and focused with electrostatic ion optics into a fast ion beam. The beam is steered into the next chamber, which houses a custom electrostatic bender [65]. This bender, composed of two curved parallel plates, bends the ion beam 90° into the next set of chambers. This bending of the beam effects rigorous ion-neutral discrimination, as the charged ion beam is directed into the next section of the instrument to be probed by the laser while any neutral molecules fly straight into the wall of the instrument. The ions are probed in the overlap section of the instrument, where the laser beam for spectroscopic detection is overlapped with the ion beam with the help of movable apertures. In this region, the ion beam traverses through a cylindrical metal drift tube as it is being probed by the laser. A square wave voltage modulation is applied to this drift tube to velocity modulate the ions for lock-in detection. The ion beam is then bent another 90° into a time-of-flight (TOF) mass spectrometer.

The ion source for the preliminary studies was a simple cold cathode source, as described in detail in Appendix A. Precursor gas flows into the back of the source, consisting of two Ultra-Torr electrodes connected by a glass tube. The two electrodes are floated (front and back) to 2–6 kV and 5.5–9.5 kV, respectively, in the cathodic extraction setup, and 3.80 kV and 0.300 kV in the anodic extraction setup. The different setups determine which molecular ions are more abundant in some plasmas. The near-infrared rovibronic spectroscopy on N_2^+ described in Appendix A made use of the cathodic extraction setup, but the setups are easily switched by changing the polarity of the power supply floating the back electrode.

The ion beam spectrometer offers several advantages for the spectroscopic study of molecular ions. The separation of ions in the beam from neutral molecules before the overlap region effects rigorous ion-neutral discrimination. The beam is coupled to a mass spectrometer for mass data that complements the optical spectra. The optical spectra themselves contain mass information in the form of Doppler-split lines, with the splitting magnitude proportional to the carrier mass. The main disadvantage of this type of in-

strument is the very low number density of ions being probed ($\sim 10^6$ cm^{-3}). This disadvantage is overcome with the highly sensitive technique NICE-OHMS. After demonstrating NICE-OHMS on the ion beam spectrometer in the near-infrared (with a scan range of 700–1100 nm), the same system was interfaced with the mid-infrared DFG NICE-OHMS spectrometer described in Chapter 2, allowing all the potential benefits to be applied to rovibrational spectroscopy.

3.3 Mass Spectrometry and Ion Beam Optimization

A useful feature of the ion beam system is its time-of-flight (TOF) mass spectrometer. Mass spectral data were used to measure the beam energy and beam energy spread of N_2^+ ions in the near-infrared work [30]. In addition, the intensity of the mass signals are used as a real-time diagnostic of the ion beam composition; the intensities from different ions change with source conditions. This way, optimum H_3^+ and HN_2^+ amounts can be determined and spectroscopy can be attempted.

As the mass spectrometer has been described in previous work [30, 66], only a brief description will be given here. The ion beam enters the mass spectrometer after the second 90° electrostatic bender, as shown in Fig. 3.1.

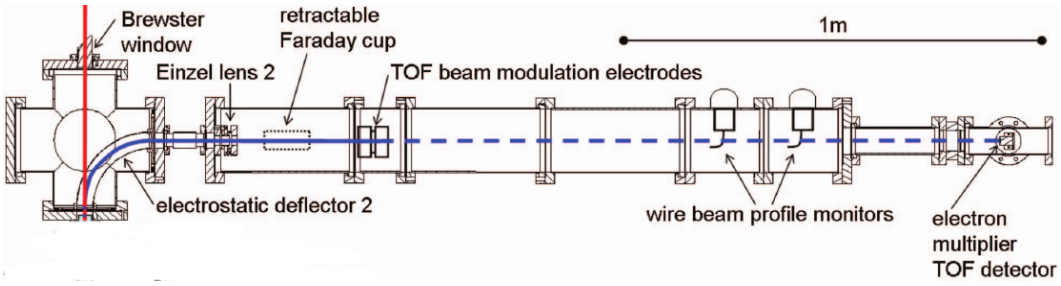

Figure 3.1: A diagram of the time-of-flight mass spectrometer used on the ion beam instrument for beam energy studies and source diagnostics. Reprinted and adapted with permission from Fig. 1 of Mills, Andrew A.; Siller, Brian M.; Porambo, Michael W.; Perera, Manori; Kreckel, Holger; and McCall, Benjamin J., *J. Chem. Phys.*, 135, 224201, (2011). Copyright 2011, American Institute of Physics.

The ion beam is modulated by two electrodes that reverse polarity at a given frequency, causing the beam to "sweep" up and down across a small aperture downstream. This sweeping across the aperture results in a packet

of ions traversing the time-of-flight tube, which has a length of 1.53 m. The ion packet is detected by an electron multiplier ion detector (SGE 14823H) after this drift region. Commercial beam position monitors (National Electrostatics Corp., Model No. 2HA003680) are used to align the modulated ion beam precisely to the axis of the tube. The output of the ion detector is read on a high bandwidth digital oscilloscope (Tektronix DPO2014). Because ions of different masses will have different velocities in the time-of-flight tube, they will reach the detector at different times, which will be indicated by different signals on the oscilloscope (see Fig. 3.2).

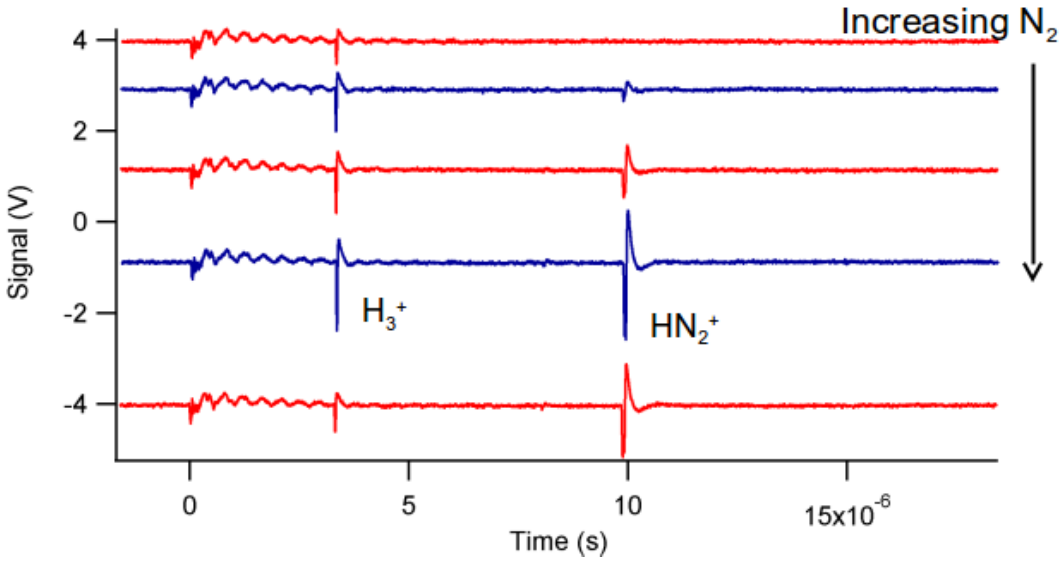

Figure 3.2: Mass spectra of a mostly hydrogenic ion beam with increasing amounts of N_2 added to the cold cathode source, showing the change in composition of the ion beam.

The beam provides an excellent diagnostic tool to optimize ion source conditions for the production of certain ions of interest. As shown in Fig. 3.2, as conditions in the source change, the mass spectral signals will alter in real time. The ion signal of interest can then be optimized by varying different parameters of the source, as shown for N_2 pressure here. It is also used to check that the ion of interest is in fact present in the ion beam when no optical spectrum has yet been obtained.

Another use for the mass spectrometer is to measure the energy of the ion beam and the uncertainty of that energy. In ion beam spectroscopy, this can be useful, as the spectral lines will be Doppler-shifted by an amount

dependent on the magnitude of the beam energy, as shown in Equation 3.1:

$$\nu_{\pm} = \nu_0 \sqrt{\frac{1 \pm v/c}{1 \mp v/c}} \tag{3.1}$$

where $\nu_{\pm}$ is the blue or red-shifted transition frequency, ν_0 is the rest frequency, v is the velocity of the ion beam, and c is the speed of light. The beam energy, which is related to the velocity of the ion beam simply by $E = \frac{1}{2}mv^2$, will direct the choice of spectroscopic scan window (though the accuracy of this is questionable, as will be discussed later). The velocity v of a certain species in the beam of mass m can be determined from the recorded flight time in the mass spectrometer and the length of the TOF tube. The beam energy spread is determined by recording flight times of several single ions one at a time, constructing a histogram of the corresponding beam energy values (or corresponding voltage values, related by $E = qV$, where q is the charge of the electron), and determining the standard deviation of a fitted Gaussian function. This value indicates the expected linewidth of the optical spectral signal one should obtain in the ion beam (in addition to the energy spread, Doppler broadening should contribute to the linewidth, but this will be narrowed by kinematic compression in the fast ion beam). Fig. 3.3 shows the beam energy spread obtained for the HN_2^+ ion in the ion beam.

As a diagnostic tool, the mass spectrometer showed that the cold cathode source can produce H_3^+ and HN_2^+, as shown in Fig. 3.2. Pure hydrogen was flowed through the source to produce H_3^+ and H_2^+. The relative abundances of each could be varied by changing conditions of the source, mainly the backing pressure and geometry of the electrodes (cathodic extraction vs. anodic extraction). HN_2^+ was synthesized by leaking in a tiny amount of nitrogen gas into the hydrogen before the source. A gas-mixing manifold was used for this purpose. The mass spectrometer results showed that the source could very easily produce both H_3^+ and HN_2^+ for spectroscopic study.

Two ways are used to measure the beam energy without a spectroscopic ion signal: the mass spectral signal and the voltage reading of the final electrode in the source. From the time-of-flight from the mass spectral signal, the velocity, and thus, the beam energy and initial voltage can be obtained by

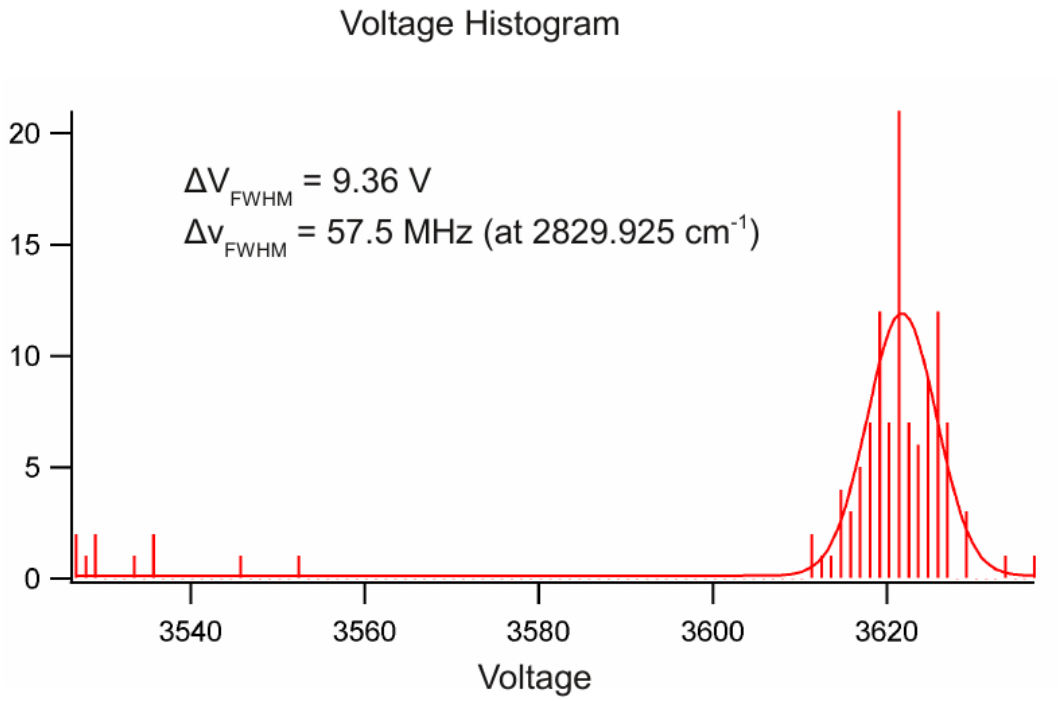

Figure 3.3: Histogram of the beam voltage of HN_2^+ in the ion beam and a Gaussian fit to the data, giving the optimum beam voltage spread as a full width half maximum (FWHM) width. The beam energy is often referred to in terms of the voltage applied to the ions to initially accelerate them, which is related to the kinetic energy of the beam by $E = qV$, where E is the kinetic energy, q is the fundamental charge, and V is the applied voltage. Thus, the beam voltage and voltage spread is directly proportional to the beam energy and energy spread.

the equation:

$$E = qV = \frac{1}{2}mv^2 \tag{3.2}$$

where q is the charge of an electron, V is the voltage applied to the last electrode, m is the ion mass, and v is the velocity. It was found in the work in the near-infrared [30] that the value from the voltage probe corresponded with the frequency of the spectral signal more closely than the mass spectroscopy beam energy. One difference implemented between the work on N_2^+ in the near-infrared and this work on H_3^+ in the mid-infrared is that the position of the electrodes have been flipped. In producing N_2^+, the anode was further upstream than the cathode. This setup worked well for producing H_2^+ with a hydrogenic plasma. To produce a useful amount of H_3^+, the cathode was placed further upstream in the source simply by switching the polarity of the

discharge power supply in the source. In this "anodic extraction" setup, it was questioned whether the voltage probe would still be the best indicator of the ion beam energy, or if readings from the mass spectrometer would be closer. An experiment was performed to measure the beam energy with both methods in both extraction setups (anodic and cathodic extraction). The results, shown in Table 3.1, indicate that the voltage probe has the more repeatable reading. The irreproducibility between different setups on the mass spectrometer readings may be due to shifts in the beam caused by changes to the ion optics that were required for peaking up the beam when going from the cathodic extraction setup to the anodic one.

	Anodic extraction	Cathodic extraction
Voltage probe reading	3.80 kV	3.80 kV
Mass spectrometer reading	3.68 kV	3.70 kV

Table 3.1: Beam voltage determined in both the anodic and cathodic ion source setup using the voltage probe on the cathode and anode, respectively, and by measuring the time-of-flight of an H_3^+ mass spectral signal.

In addition, the work from the N_2^+ showed that the optical spectral lines were shifted from the frequency expected from the voltage probe by an amount corresponding to 200 V. This information was used to scan for H_3^+ with NICE-OHMS, but again, no signal was obtained.

3.4 Optical Spectroscopy of the Ion Beam

Preliminary spectroscopic studies of the ion beam in the mid-infrared were performed. For this preliminary step, efforts were concentrated on obtaining spectra of H_3^+, a simple ion that was easily produced. The TOF mass spectrometer demonstrated that H_3^+ could be produced at a relatively high abundance. An attempt at probing the R(3,3)^l line of the ν_2 band of H_3^+ was made around 2825 cm^{-1} (red-shifted from the rest frequency by the high velocity of the ion beam).

First, cavity-enhanced velocity modulation spectroscopy (CEVMS) [67] was attempted on H_3^+. This system is very similar to the NICE-OHMS technique described in Chapter 2; however, the laser is not phase-modulated

for frequency modulation spectroscopy. Due to technical issues at the time (the bandwidth of the InSb detector used for NICE-OHMS needed to be adjusted), the FMS components had to be bypassed, resulting in higher noise. However, the signal enhancement from the cavity should have been enough to see something.

Two methods of scanning the H_3^+ ion beam sample using CEVMS were employed. One method involved scanning the wavelength of the laser, as described in Appendix A. For the second method, in an effort to quickly beat down the noise by ensemble averaging several scans, the offset of the velocity modulation signal on the drift tube is modulated at a frequency of ~ 5 Hz by an amplitude of ± 25 V in a reverse sawtooth wave. This method was also briefly tried in the near-infrared ion beam spectroscopy work. Figure 3.4 shows a conceptual schematic of this method, where the higher frequency velocity modulation signal is summed onto the reverse sawtooth ramp with an operational amplifier-based summing amplifier circuit for sweeping the ion beam velocity (and thus the Doppler shift of the ion transitions) while also quickly velocity modulating the ions. Similar methods of sweeping an ion beam on to resonance with a fixed laser wavelength have been used in the past [48, 49]. The scan range at this velocity is about 940 MHz. The advantage of this method is that the ion beam could be scanned quickly and repeatedly, with several scans rapidly ensemble averaged on an oscilloscope. The disadvantage compared to scanning the laser wavelength is that only a small wavelength range could be scanned using the drift tube sweeping, limited by the voltage range of the summing amplifier circuit. An averaged scan is shown in Figure 3.5.

For both scanning methods (the laser or the drift tube), no H_3^+ signal was obtained with CEVMS. Several steps were taken to increase the sensitivity of the instrument in order to observe a signal. Analysis of the noise with the laser scanning method indicated that the sensitivity in terms of a noise equivalent absorption (NEA) was around 10^{-6} for CEVMS, which would require the ion beam current to be around 4–5 μA in order to see a signal. It was also found that scanning the laser produced a factor of 10 lower noise than observed by scanning the drift tube in a comparable period of time. Therefore, source conditions were varied to produce a current of 4–5 μA while scanning the laser. The hole diameter in the front ferrule affects the beam current, where a larger diameter gives more current. A current of 5–

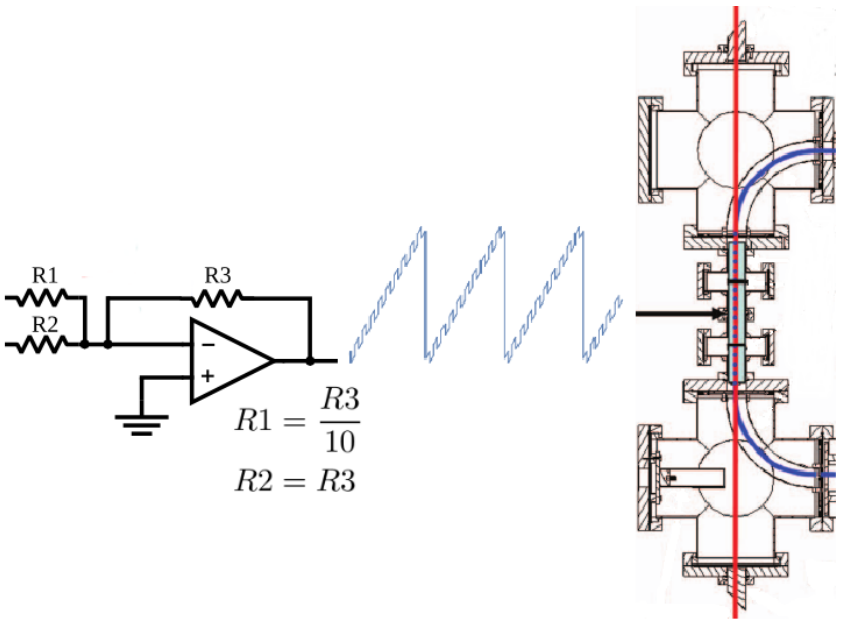

Figure 3.4: Conceptual schematic showing how the drift tube was scanned while still effecting velocity modulation. The arrow points to the drift tube (light blue) in the overlap region of the ion beam spectrometer. Ion beam spectrometer image reprinted and adapted with permission from Fig. 1 of Mills, Andrew A.; Siller, Brian M.; Porambo, Michael W.; Perera, Manori; Kreckel, Holger; and McCall, Benjamin J., *J. Chem. Phys.*, 135, 224201, (2011). Copyright 2011, American Institute of Physics.

7 μA was observed through the alignment apertures with a hole diameter of 1.5 mm. In addition, the ballast resistance to the source was adjusted to 50 kΩ. The NEA with this setup was 2×10^{-7}; a signal-to-noise ratio of 6 was expected for the H_3^+ transition at 2825 cm^{-1}.

In addition to high noise, another issue that plagued this setup was instability in the ion source, where electric arcs would form from locations on the source to other parts of the vacuum chamber or the plasma would visibly "flicker," modulating in intensity. Generally, the beam current would decrease soon after observing the flicker. Several variables were explored to prevent these occurrences. The ferrule where ions were extracted was made sure to be flush to the metal cap holding it, preventing any sharp edges where the electric charge density would build up and cause an arc. It was discovered that the Teflon gas inlet tube constricted due to heat from the source, which was surmised also to contribute to source instability. A "stent" in the form of a spring or a small stainless steel tube was placed in the gas inlet tube of the

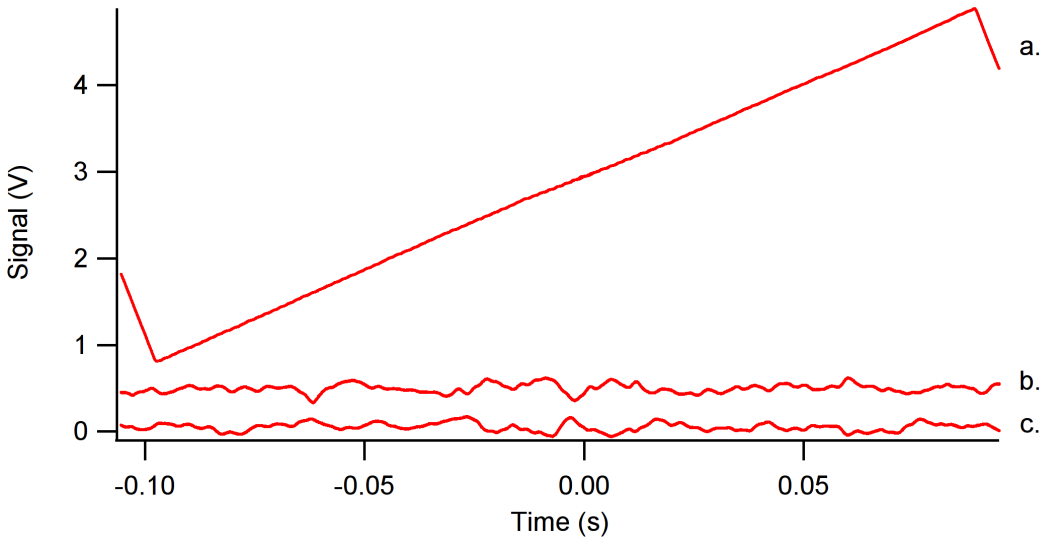

Figure 3.5: Plot of averaged scans from scanning the drift tube with an H_3^+ ion beam around 2824 cm^{-1}. a.: the scanning ramp applied to the drift tube. b. and c.: the output of lock-in amplifiers referenced to the velocity modulation frequency applied on top of the sweep.

source to keep the tube open as the temperature increased with the source being used. These measures also contributed to getting the beam current up to 5–7 μA. No H_3^+ signal was observed after these changes, however.

The spectroscopy setup was changed to NICE-OHMS for added sensitivity. Surprisingly, the sensitivity was just as low as CEVMS, which may be due to poor detector noise rejection. A detector with sufficient bandwidth is necessary to acquire the NICE-OHMS signal at the large modulation frequency. The detector used for NICE-OHMS needed adjustment to obtain any sensitivity at the necessary bandwidth, and a higher bandwidth detector seems to be offset by poor noise rejection. At this point, arcing and instability in the ion source was mitigated by replacing the Teflon tube on the back cathode with a stainless steel tube. The idea was to prevent the heat from the source partially melting the Teflon tube and constricting the flow; the steel tube should be more effective than a stent. In order to increase the sensitivity, several NICE-OHMS spectra of the ion beam were acquired and co-added to decrease the noise. However, the instability of the source precluded enough scans to be collected for sufficient ensemble averaging. Scans obtained by scanning the drift tube were also attempted, but unsuccessful.

3.5 Discussion of Non-Detection

No signals were obtained from the ion beam using the mid-infrared DFG spectrometer. Both CEVMS and NICE-OHMS with velocity modulation of the ion beam were attempted, with no success.

The non-detection of H_3^+ in the mid-infrared DFG spectrometer appears to be due to an insufficient sensitivity to detect the small number density of ions in the ion beam. The highest ion beam current recorded through the apertures was 7 μA. This corresponds to an ion density, N, of 1.25×10^7 ions cm^{-3}, given an ion beam size of 3 mm in diameter. The expected linewidth is 40 MHz, obtained from taking the linewidth observed in N_2^+ (120 MHz) and scaling the Doppler width by the different masses and frequencies (120 MHz $\times \sqrt{\frac{28 \text{ amu}}{3 \text{ amu}}} \times \frac{2829.925 \text{ cm}^{-1}}{10859.34392 \text{ cm}^{-1}} \approx 96$ MHz). The expected maximum fractional absorption signal, then, can be calculated by:

$$\begin{aligned} \text{Fractional Absorption} = (S \times F_{band})(L \times \frac{F}{\pi})(N)(\frac{1}{2.129 \times \frac{\Delta\nu}{2}}) \\ \times (J_0(0.79) \times J_1(0.79)) \end{aligned} \quad (3.3)$$

where S is the band strength in cm/ion, L is the pathlength (length of laser/ion beam overlap) in cm, F is the finesse, N is the ion number density in cm^{-3}, J_0 and J_1 are Bessel functions evaluated at the modulation index 0.79 giving the modulation losses from the heterodyne spectroscopy, F_{band} is the "fraction of band" of the rovibrational line (defined below), and $\Delta\nu$ is the FWHM linewidth of the signal in cm^{-1}, assuming a Gaussian profile.

S is calculated from the transition dipole moment of the ν_2 band of H_3^+, μ = 0.160 D [7], with the equation [66]:

$$S = 2.5066\nu\mu^2 \quad (3.4)$$

where ν is the band origin frequency of 2521 cm^{-1}. The band strength in km/mol, then, can be calculated as:

$$S = 2.5006 \times 2521 \text{ cm}^{-1} \times (0.160 \text{ D})^2 \quad (3.5)$$

$$= 161 \text{ km/mol} \quad (3.6)$$

This value can be expressed in cm/ion:

$$161 \text{ km/mol} \times \frac{10^5 \text{ cm}}{1 \text{ km}} \times \frac{1 \text{ mol}}{6.022 \times 10^{23} \text{ ions}} = 2.68 \times 10^{-17} \text{ cm/ion} \quad (3.7)$$

To obtain the fraction of band in the R(3,3)^l line, the line intensity of that transition at the expected temperature of the ion beam is divided by the sum of the line intensities for all the lines in the band at that temperature. Using the H_3^+ Online Intensity Calculator [68], the line intensity for the R(3,3)^l line was calculated to be 61.8 cm^{-2} atm^{-1} at rotational and vibrational temperatures of 750 K (estimated from the temperature determined on the N_2^+ ion beam (Appendix A). The sum of the intensities of the lines in the ν_2 band was calculated to be 1490 cm^{-2} atm^{-1}. Therefore, F_{band} is calculated to be 61.8 cm^{-2} atm^{-1}/1490 cm^{-2} atm^{-1}, or 0.0414. Multiplying by the band strength of 2.68×10^{-17} cm/ion gives a line strength of 1.11×10^{-18} cm/ion.

The total optical pathlength $L \times \frac{F}{\pi}$ is calculated from the overlap length, $L = 27$ cm, and the finesse, $F = 250$. The total optical pathlength is then 2150 cm.

With the number density of 1.25×10^7 cm^{-3} and the expected linewidth of 96 MHz = 0.00307 cm^{-1}, the expected fractional signal can be calculated:

$$\begin{aligned}
\text{Fractional Absorption} &= (S \times F_{band})(L\frac{F}{\pi})(N)(\frac{1}{2.129 * (\Delta\nu/2)}) \\
&\quad \times J_0(0.79)J_1(0.79) \\
&= (1.11 \times 10^{-18} \text{ cm/ion})(2150 \text{ cm})(1.25 \times 10^7 \text{ cm}^{-3}) \\
&\quad \times (\frac{1}{2.129 \times (0.00307 \text{ cm}^{-1}/2)})(J_0(0.79) \times J_1(0.79)) \\
&= 2.83 \times 10^{-6}
\end{aligned}$$

This expected fractional absorption can then be compared to the smallest noise obtained with the ion beam experiment. The smallest noise recorded was 2×10^{-7}. This was obtained by taking the standard deviation of the noise in a flat portion of a scan and converting it into a fractional noise equivalent absorption. A correction to this value needs to be made by multiplying it by a factor of 10 to account for the gain ratio between the AC signal and the DC signal. Thus, the lowest noise obtained in this setup was $\approx 2 \times 10^{-6}$. Dividing the expected fractional absorption by this value gives a signal-to-noise ratio around 1, which would not be detectable. Additionally, the observed signal

in the near-infrared studies of the ion beam was a factor of ~ 6 below what was expected, as reported in Appendix A. Therefore, this setup was not sensitive enough to detect the H_3^+ sample in the ion beam.

As discussed in Chapter 4, one of the issues that seems to limit the sensitivity is the noise at high frequency of the InSb detector used in the NICE-OHMS experiment. The InSb system requires a high bandwidth to detect the FMS signals at 113 MHz, but the high bandwidth limits the noise rejection. Thus, it appears that the fundamental shot noise limit may not be technically feasible with this system. A different detection system with high noise rejection at high frequency may be a way to decrease this technical noise enough to see a signal from H_3^+ in an ion beam system such as this.

3.6 Summary

In summary, mid-infrared spectroscopy was attempted on a fast ion beam using a cold cathode ion source for preliminary studies. The spectroscopic targets in the mid-infrared were HN_2^+ and H_3^+, both of which were confirmed to have been produced using the time-of-flight mass spectrometer attached to the ion beam system. The mass spectrometer gives information on the beam energy and beam energy spread, but it was surmised that a direct measurement of the source would give a more accurate reading of the beam energy. Spectroscopy of the ion beam was tried with both cavity-enhanced velocity modulation spectroscopy (CEVMS) and noise-immune cavity-enhanced optical heterodyne molecular spectroscopy (NICE-OHMS). Two methods of acquiring scans with these techniques were used: one where the wavelength of the laser was scanned and another where the Doppler shift of the ion absorption signal was scanned. Lower than expected sensitivity of both CEVMS and NICE-OHMS, combined with instability of the cold cathode source during operation, prevented detection of an H_3^+ signal. Assuming the highest current obtained in the experiment so far, the expected signal is calculated to be about a factor of 3 larger than the observed lowest noise. While this should be detectable, an unexplained factor of 6 in the work of Appendix A may preclude the detection of a signal at the sensitivity observed here. It is expected that if some technical issues in this experimental setup are addressed (better noise rejection in the detection system and more stability in

the ion source), a signal can be detected in the mid-infrared with this ion beam spectrometer.

CHAPTER 4

TOWARD SCRIBES AND PRELIMINARY SPECTROSCOPY OF THE SUPERSONIC EXPANSION DISCHARGE SOURCE

4.1 Introduction

As mentioned in Chapter 1, one of the challenges of performing laboratory spectroscopy of molecular ions is the high internal temperature of the sample. Many ion sources, such as traditional glow discharge gas cells, produce ions at relatively high rotational temperatures. Even with cryogenic cooling, the rotational temperature of molecular ions are still about 170–200 K, depending on the molecular ion [69, 70]. Analysis of the near-infrared N_2^+ signals from the ion beam yielded a rotational temperature of ∼750 K [30]; in this study, the ions were produced by a cold cathode source.

High internal temperature can be detrimental to spectroscopy of these systems because of quantum dilution. At higher rotational temperatures, for example, a greater number of rotational states will be occupied than would be at lower temperature. Put another way, the rotational partition function is greater at higher temperature. The effect on the rovibrational spectrum is that, at higher temperature, the transition intensities overall will be smaller and more numerous. At lower rotational temperature, fewer transitions will be present, and they will be stronger. This is illustrated in Figure 4.1. This quantum dilution is especially debilitating for large or fluxional molecules and molecular ions. Therefore, spectroscopy on low temperature samples of these types of molecules are desirable.

In addition to cryogenic cooling of glow discharge sources, there are other methods to produce molecular ions at low temperature. Ion traps, for example, have been used to produce H_3O^+ and CH_5^+ down to about 4 K [75]. Action spectroscopy can be performed to obtain mass spectral signals as a function of laser wavelength [9]. Buffer gas cooling has also been used for the production of cold samples [76, 77]. For direct absorption spectroscopy, su-

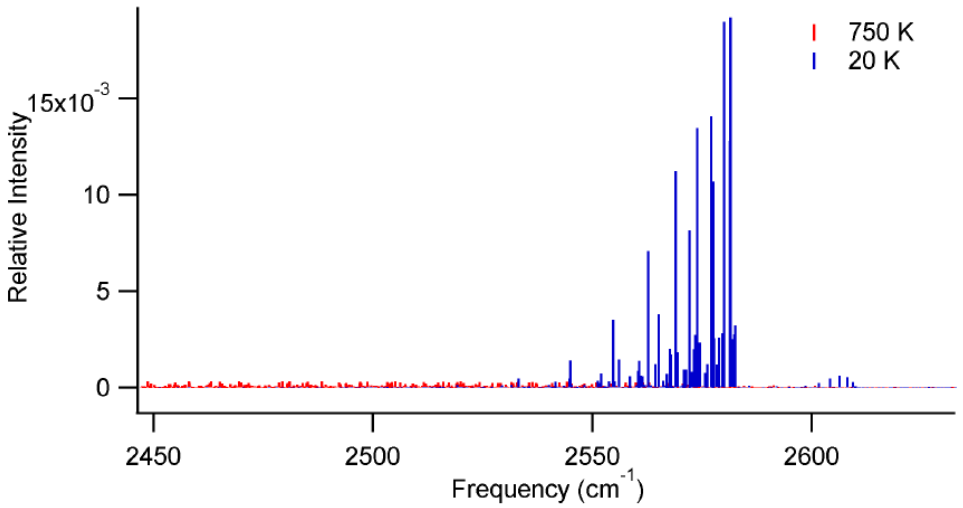

Figure 4.1: Simulated spectra of H_2CO^+ at two different rotational temperatures, demonstrating the simplification of the spectrum and increase of signal strength at lower temperature. The spectra were simulated with PGOPHER [71]. The band origin was obtained from Reference [72], the rotational constants were obtained from Reference [73], and centrifugal distortion constants were estimated from Reference [74] and references therein.

personic expansion discharge sources have been used in a variety of designs. Corona-type discharges [39, 41, 78] have been employed in the past, where a discharge is struck as gas flows over a needle-like electrode in the throat of the source. The issue of clogging of the throat can be overcome with the gas flowing through two electrodes. Geometries include slit-based sources [43] and pinhole sources [44, 79]. One of the benefits of the supersonic expansion discharge source is that primary ions can be probed. Because of the high velocity of the ions through the discharge region, primary ions will not have enough time to react with other species in the expansion, allowing them to be probed. These same species are not as readily producible in traditional glow discharge sources.

In order to take advantage of a cooled molecular ion sample for ion beam spectroscopy, an attempt at integrating the continuous supersonic expansion discharge source described in Reference [44] into the ion beam spectrometer of Appendix A was made. The attempted integration involved mounting the source in the chamber, machining and mounting beam skimmers to extract the cooled molecular ions from the expansion, and rearranging the

instrument to effect the necessary pumping for an effective expansion and extracted beam. The ultimate goal was to form a cooled ion beam that would be probed by the NICE-OHMS technique in the overlap region of the spectrometer. Before actually extracting a beam and performing NICE-OHMS on it, spectroscopic tests of the expansion itself were attempted along with tests of the ion transmission through the skimmers. It was found through vacuum conductance calculations that the pressure required to get a useful expansion would result in too high of a pressure in the subsequent chamber where the ion optics focus and direct the beam. Therefore, initial tests were attempted in the first two vacuum chambers separately from the rest of the ion beam spectrometer to test the source spectroscopically. Double-pass wavelength modulated frequency modulation spectroscopy was attempted first; plans were also made to probe the source with cavity ring-down spectroscopy. Ultimately, the setup was altered again to use the highly sensitive NICE-OHMS technique on the supersonic expansion directly, abandoning the ion beam spectrometer for the present.

4.2 Supersonic Expansion Discharge Source

A supersonic expansion discharge source is an effective way of cooling molecular ions to low temperatures. In a supersonic expansion, gas at room temperature and high backing pressure is forced through a narrow orifice (a pinhole or a slit) into vacuum. The collisions in the orifice convert random translational motion into directed motion, lowering the translational temperature. In addition, collisions here de-excite the rotational and vibrational levels, lowering their temperatures as well. The gas expands into vacuum with no change in entropy, resulting in an adiabatic expansion. In the literature, a distinction is made between two types of expansion: low chamber pressure and high chamber pressure expansions [80]. Low chamber pressure systems require diffusion pumps to keep the chamber pressure low ($\sim 10^{-4}$ Torr). In this setup, the expansion occurs with no shock structure. In high chamber pressure systems, often known as Campargue expansions [81], the high background pressure ($\sim$100 mTorr) results in a shock wave forming around the expansion, consisting of a barrel shock on the sides of the expansion and a Mach disk at the end. The interior of this shock wave contains the "zone

of silence," where the cooled molecules are unaffected by the background gas [81]. This type of expansion requires less stringent vacuum conditions.

The Campargue-type expansion was utilized in the present work using a continuous supersonic expansion discharge source. A brief description of this discharge source is presented here; a more thorough description is found in Reference [44]. The modular design consists of a 1.33" stainless steel CF flange welded to a 1/4" stainless steel tube that acts as the inlet and the anode. This piece is connected to another CF flange with a pinhole in the center, sealed by a copper gasket. A Macor spacer separates this anode from a small stainless steel or tungsten cathode that is sealed with o-rings to the spacer and a Macor cap. The dimensions of the channel through which gas flows goes from 0.5 mm inner diameter in the anode to 4.1 mm inner diameter at the end of the Macor cap, with the aperture of the cathode and cap flared. About 15–30 psig of precursor gas is applied to the source. The high pressure gas flows out of the nozzle and expands into the source vacuum chamber pumped by a Leybold RUTA 13000 three stage Roots blower system, with a nominal pumping speed of 13,000 m^3/hr (or $\approx$ 3600 L/s). A shock wave structure forms at a relatively high chamber pressure of $\sim$100 mTorr. The chamber pressure is adjustable by varying the opening of the gate valve between the Roots blower and the chamber. A discharge is struck between the two electrodes by holding the anode at ground and applying a high negative voltage ($\sim$1 kV) to the cathode. This way, ionization occurs in the throat of the nozzle and the formed ions are cooled through adiabatic expansion. H_3^+ spectra had been obtained previously with cavity ring-down spectroscopy, and the rotational temperature of the H_3^+ sample was estimated to be 80–110 K [44].

Properly skimmed, the cooled ions from the expansion source can be extracted and formed into an ion beam, and this was the ultimate goal of the ion beam spectrometer. Rather than the cold cathode source described in Chapter 3, the supersonic expansion discharge source [44] would be the source of ions for the ion beam spectrometer. After extracting the cooled ions from the zone of silence with a beam skimmer, the ions would be focused and steered with ion optics into a fast ion beam, bent 90° with the custom electrostatic bender [65], and probed by a laser beam for high resolution spectroscopy. This system would be known as Sensitive, Cooled, Resolved Ion BEam Spectroscopy (SCRIBES). The instrument would couple the advantages of an ion

beam spectrometer (ion-neutral discrimination, Doppler-shifted lines with mass information, and a mass spectrometer) with the advantages of probing a cooled molecular ion sample.

4.3 Proposed Integration of the Supersonic Source with the Ion Beam Instrument

4.3.1 Proposed Instrument Arrangement

Figure 4.2 shows the intended layout for SCRIBES. Compared to the ion beam spectrometer of Appendix A, this system has an additional six-way cross housing another electrostatic bender [65] that would bend the ions another 90°. This was planned due to technical reasons for attaching the Roots blower vacuum pump system to the source chamber. Because of the

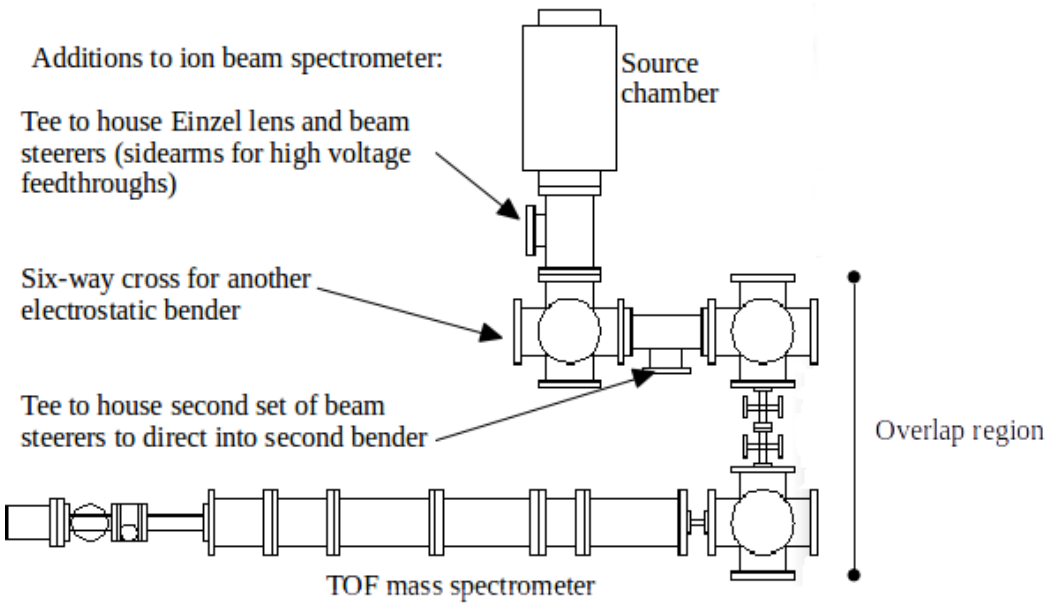

Figure 4.2: Proposal for the layout of SCRIBES. Due to technical limitations in the laboratory, a third bender would be added to steer the ion beam away from the ion source and toward the second bender before the overlap region with the laser beam. Figure not drawn exactly to scale.

location of the pipe connecting the Roots blower system on the outside of the laboratory to the source chamber, the location of the source chamber in the laboratory is fixed. The optics table had to fit around the overlap region, but

could not do so if the source chamber fed directly into the bender before the overlap region, as depicted in Appendix A. Therefore, the source chamber would be rotated 90° from its orientation in Appendix A, and another bender would be used to steer the ion beam to the overlap region, as shown here. The Einzel lens and steerers would be placed in vacuum tees, powered via SHV feedthroughs on the side-arms.

4.3.2 Source Mounting

A mounting apparatus for the supersonic source was designed by adapting the mount for the cold cathode source. This mount is shown in Figure 4.3. The supersonic expansion source is connected via a 1/4" Swagelok union to the Teflon gas inlet line (an Ultra-Torr union was considered for easy detachment, but is only rated for 20 psig). The inlet line is threaded through the stainless steel tube used to translate the source in the direction of gas flow and through the translation plate to which this tube is attached. The translation plate can be slid back and forth on aluminum rods connected to the inside of the vacuum flange on the source chamber. Plastic spacers are placed around the bolts connecting the translation plate and the end of the stainless steel inlet tube to ensure even mounting. To prevent drooping, the Swagelok union is mounted in an aluminum cylinder attached to the translation plate with cap screws. The bolts on the back of the supersonic expansion source head rest in holes on the front of the aluminum cylinder (much later, the aluminum cylinder was modified to allow for attachment of the supersonic source directly onto the aluminum cylinder through one set of bolts on the source). This design allows for easy translation of the source axially toward and away from the probe laser. The entire mount can be translated vertically and horizontally on the outside face of the vacuum flange.

4.3.3 Beam Skimmers

In order to extract the cooled ions in the expansion for the ion beam, a beam skimmer needs to be mounted downstream of the nozzle. The skimmer is a conical piece of metal or some other material aerodynamically designed to

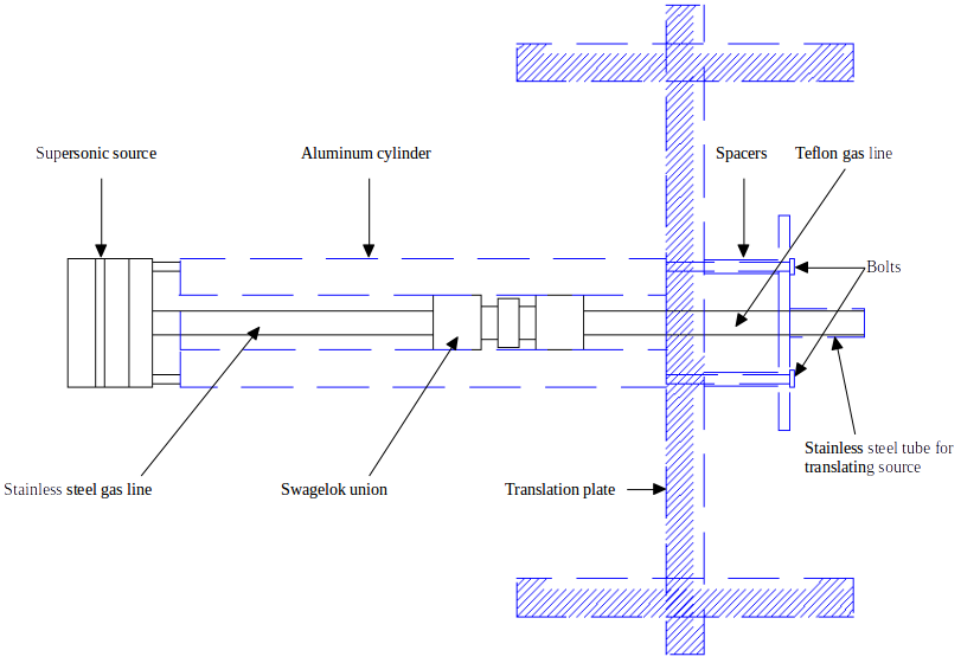

Figure 4.3: Schematic of the mount for the supersonic expansion discharge source.

insert into the zone of silence with minimal disruption of the shock structure. Careful design of the beam skimmer prevents shock waves from forming at the entrance to the skimmer, which would disrupt the cooling of the sample. Regarding the geometry of the skimmer, the angles of the interior and exterior walls are crucial for obtaining useful transmission [82]. Too obtuse angles will cause a shock wave to form at the skimmer orifice, disrupting the temperature of the sample and reducing the intensity of sample transmitted through the skimmer. Too acute angles do not leave enough room for the sample that is skimmed to continue expanding without hitting the interior of the skimmer, likewise raising the temperature and affecting the beam energy. In addition, for the study of molecular ions, the skimmer would have to be conductive and electrically float.

Given these considerations, electrical discharge machined (EDM) graphite beam skimmers were designed and manufactured. Graphite was chosen as an inexpensive, easily machinable alternative to high-end commercial metal beam skimmers; a study found that the performance of graphite skimmers is comparable to commercial metal skimmers [82]. Two skimmers were manufactured based on successful designs published in References [82] and [83].

Schematics of these skimmers are shown in Figure 4.4, and a photo is shown in Figure 4.5. The "long" skimmer is based on the design of Reference [82].

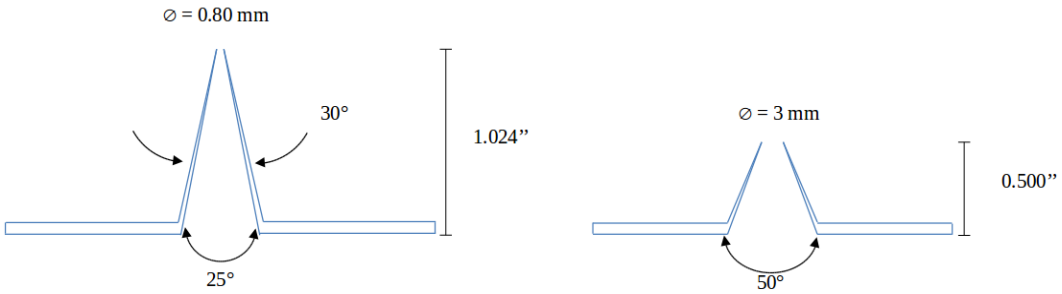

Figure 4.4: Diagrams of the two EDM graphite skimmers that were manufactured for SCRIBES.

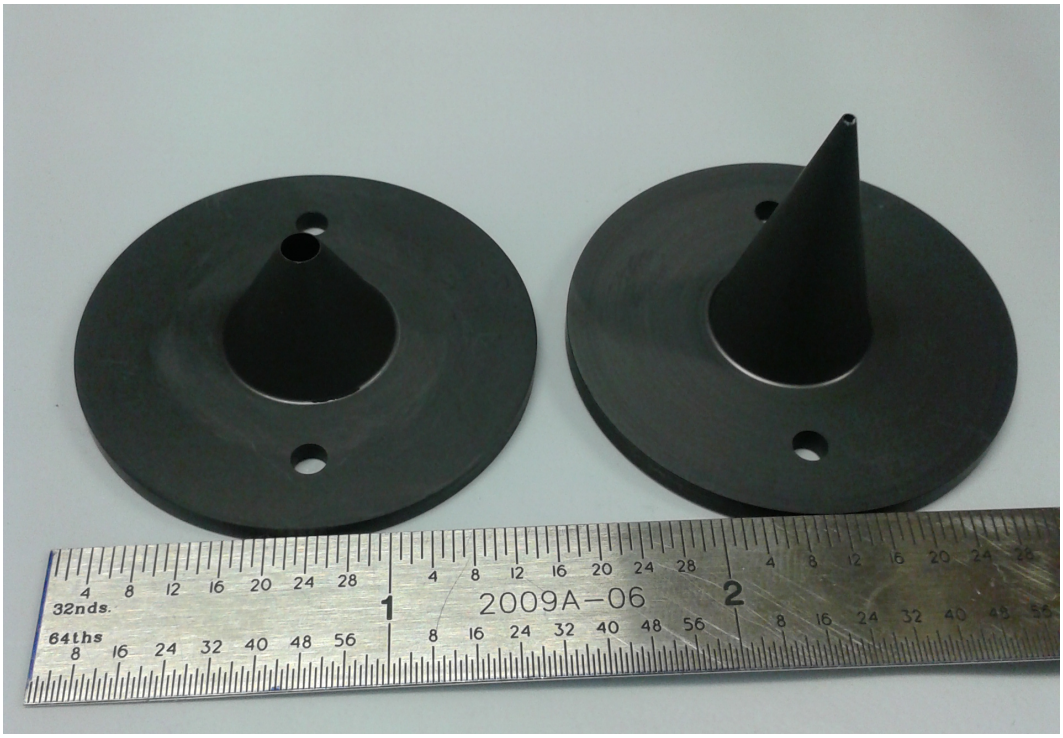

Figure 4.5: Photo of the short and long graphite beam skimmers.

The length from the base to the orifice is 1.024 in, with an interior angle of 25° and an exterior angle of 30°. The diameter of the orifice is 0.80 mm, with the lip machined to be very sharp (lip radius ~ 1 μm). A sharp orifice is beneficial, as scattering interference from the lip will be minimized. The "short" skimmer, based on a design from Reference [83], is only 0.500 in long from orifice to base and has a larger orifice of 3 mm in diameter. The interior

angle is a larger 50°. From an HN_2^+ expansion skimmed with such a skimmer, an ion beam with a rotational temperature of 78 ± 20 K was obtained previously [83]. It was also found that as the length of the skimmer decreases and the diameter of the orifice increases, the ion current transmitted through the skimmer should increase [83].

A custom mount/gasket was designed for mounting the skimmers in the instrument. The mount also was used to seal the source chamber from the next chamber housing the ion optics; differential pumping between the two chambers could then be realized. The mount was made out of Teflon to electrically isolate the skimmer from the side wall of the source chamber. The skimmer was floated by attaching an insulated wire with a ring connector to the base of the skimmer using one of the #4-40 mounting screws. Because of the softness of the material, metal inserts were placed in the threaded mounting holes of the Teflon mount. An o-ring seals the connection between the mount and the sidewall. The mount was attached to the extraction plate already mounted in the chamber by drilling tapped holes into the extraction plate and attaching the mount with cap screws. A schematic of the mount is shown in Figure 4.6, with a photo depicting the short skimmer attached to the mount in Figure 4.7.

The ion current transmitted through the long skimmer was investigated with a hydrogenic plasma, though arcing in the chamber precluded a conclusive value at small skimmer-source distance. The long skimmer was mounted in the source chamber, and the ion current was read from a Faraday cup immediately downstream of the skimmer in a six-way cross attached directly to the source chamber (see Section 4.3.4). At a skimmer-nozzle distance of ~ 2 in, a stable beam current of ≈ 2 μA was observed. However, at closer distances the pressure in the six-way cross chamber became too high for its turbomolecular pump to operate safely, and arcing was observed in the source chamber. A current reading of 0.6 μA was observed, but due to arcing, the value may not be trustworthy.

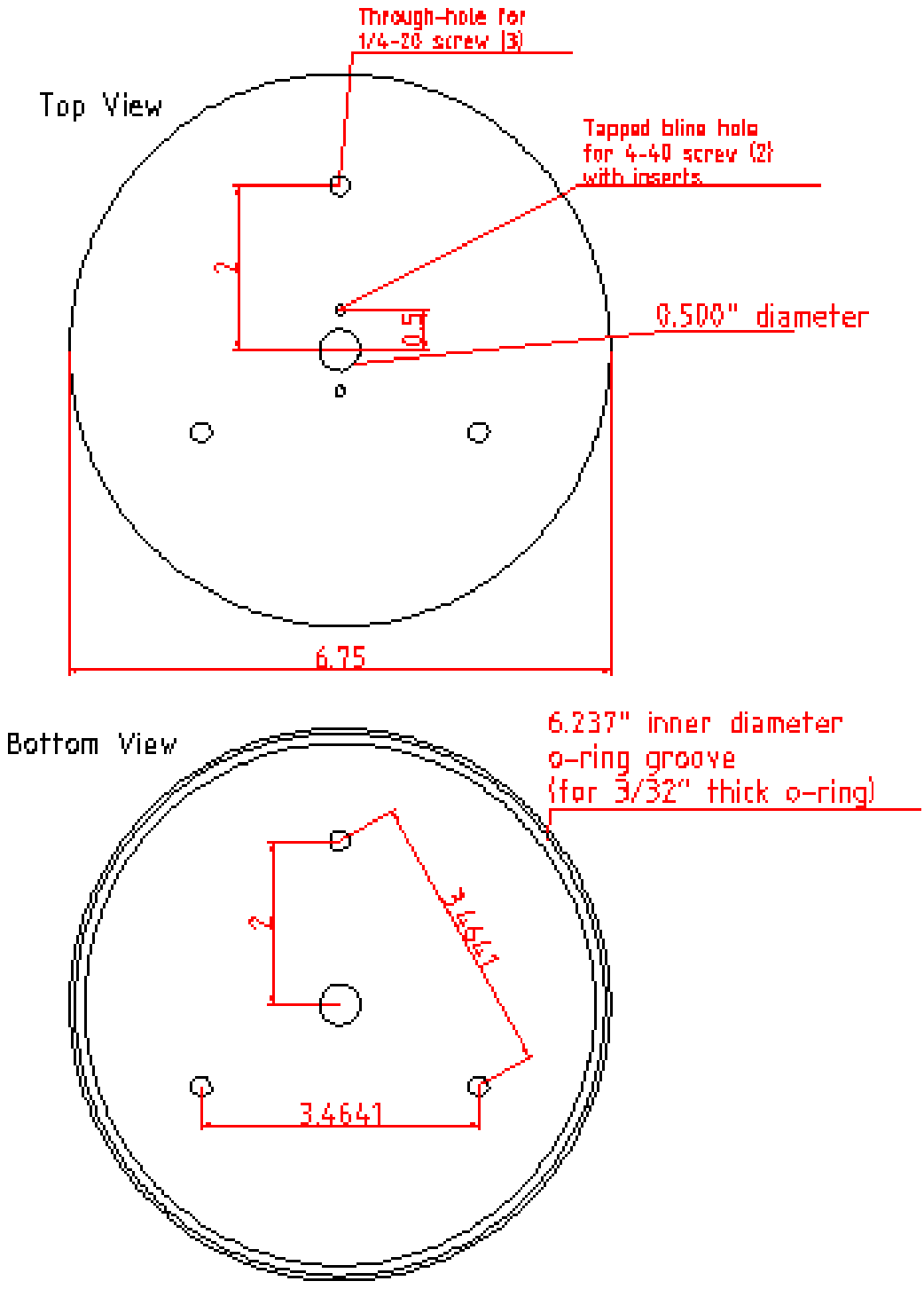

Figure 4.6: Schematic of the Teflon mount/gasket for attaching the skimmer.

Figure 4.7: The short skimmer on the Teflon mount in the source chamber.

4.3.4 Vacuum Chamber Rearrangement and Estimated Pressure

With a mount for the supersonic expansion discharge source, skimmers, and a skimmer mount, the source could be integrated with the ion beam instrument

to complete SCRIBES. In addition to these items, the vacuum chambers comprising the ion beam instrument had to be rearranged according to the plan outlined in Figure 4.2. In this setup, the source chamber would be pumped by the Roots blower system, attached via a steel pipe and ISO 250 bellows to the source chamber. The first six-way cross in Figure 4.2 would be pumped by the 2000 L/s turbomolecular pump originally on the source chamber (though the effective pumping speed would be greatly diminished by the conductance of the adapter). The remaining two six-way crosses would be evacuated by 500 L/s turbomolecular pumps.

However, a calculation of the estimated pressure in the vacuum chambers with the supersonic expansion source running indicated that the pressure would be too high downstream of the skimmer, with an estimated pressure of 50 mTorr (assuming the short skimmer with the wider diameter is used). The details of the calculation are shown in Appendix D. Too high of a pressure would cause two debilitating issues: the turbomolecular pumps would not run, and electrical arcing would occur among the ion optics, disrupting the skimmed ion beam. Therefore, the expansion was tested in a simpler arrangement first with only the source chamber attached to a six-way cross pumped by a 500 L/s turbomolecular pump. Rather than building the instrument up as proposed in Figure 4.2, for the time being only the source chamber was moved into the proper location and orientation. The source chamber was then attached to a six-way cross, as shown in Figure 4.8. This is also the configuration with which the long beam skimmer was tested.

One issue that needed to be addressed was the predicted contraction of the bellows connecting the source chamber with the Roots blower pipe. The ISO 250 bellows have an inner diameter of ≈10 in. The force from the atmosphere, then, on the chamber while under vacuum is:

$$\begin{aligned} \text{Force} &= \text{Pressure} \times \text{Area} \\ &= 14.7 \text{ lb/in}^2 \times \pi(\frac{10 \text{ in}}{2})^2 \\ &= 1,154 \text{ lb} \end{aligned} \tag{4.1}$$

This would surely contract and destroy the bellows when the Roots blower is running. To prevent this, the source chamber was transferred and attached to a Unistrut frame and a brace was constructed out of Unistrut to brace this frame to the Roots blower pipe, as depicted in Figure 4.8. The bellows were

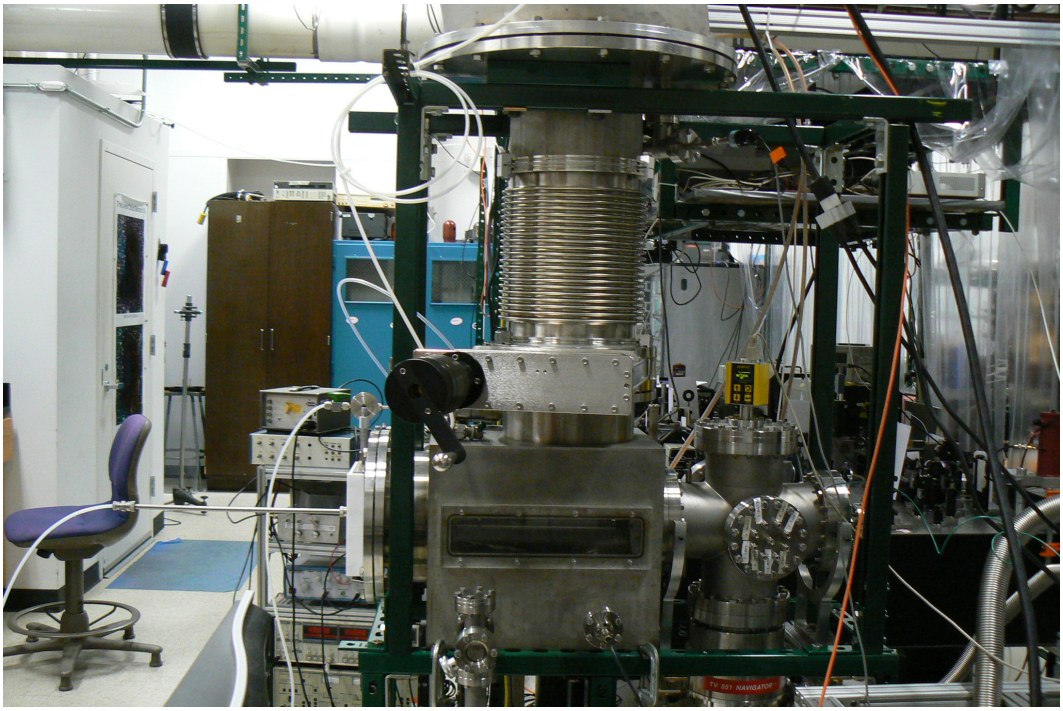

Figure 4.8: Photo of the vacuum chamber setup for preliminary tests of the supersonic expansion source. A brace was constructed out of Unistrut to prevent the chamber from crushing the bellows when the Roots blower is running.

eventually replaced with a rigid, custom-length vacuum nipple to securely suspend the source chamber without the need for a brace.

4.4 Preliminary Supersonic Source Tests

Prior to the skimmer tests and attempting to make an ion beam, spectroscopy was performed on the supersonic expansion discharge itself with the arrangement depicted in Figure 4.8. The goal was to investigate the conditions in this apparatus for successful performance and to verify the rotational cooling in the source when positioned in this new setup. After the supersonic source would be optimized in this configuration for rotational temperature, optimizing the transmission through the skimmer and forming the ion beam would have been the next step. With a strong ion beam and subsequent optimization of the pressure downstream of the skimmer to prevent arcing, the long-term goal was to use the ion optics and benders to direct the ion beam

into the overlap region. Here, the highly sensitive technique of NICE-OHMS would be used to obtain spectral lines of an ion beam and determine the rotational temperature of the sample. Any change in the temperature of the ions between the supersonic expansion and the overlap region of the instrument would be of great interest, and the minimization of any heating would have to be addressed. Therefore, an estimate of the rotational temperature of a molecular ion in the expansion that could also be studied in the overlap region would be useful.

For initial optimization of the source conditions, two simple discharges were used. Hydrogen was used as the precursor gas for one expansion, making primarily H_2^+ and H_3^+. In another discharge, nitrogen was flowed into the source to primarily make N_2^+. As in Reference [44], the source is powered by floating the cathode to a high negative voltage through a 10 kΩ ballast resistor. A nitrogenic expansion is shown in Figure 4.9, and parameters for obtaining nitrogenic and hydrogenic expansions are shown in Table 4.1. The

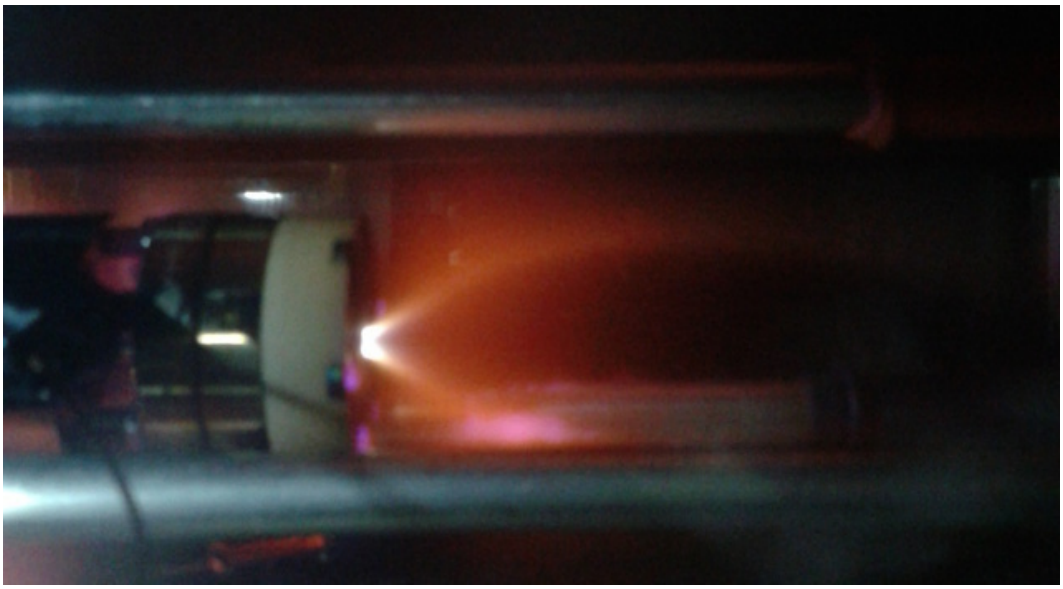

Figure 4.9: Supersonic expansion discharge source with nitrogen discharge.

chamber pressure in these expansions was kept in the 100 mTorr range by varying the position of the gate valve between the source chamber and the Roots blower pipe. This pressure range was critical for getting a well-defined barrel shock in both types of expansions. Arcing was observed to parts of the source mount and the screw heads of the skimmer mount (the skimmer was removed for these initial tests). Electrical tape was placed on parts of

Optimized Parameters for the Supersonic Expansion

Gas	Discharge voltage (V)	Discharge current (mA)	Backing pressure (psig)
Nitrogen	−960	36	22
Hydrogen	−1220	54	15

Table 4.1: Initial parameters for obtaining well-defined supersonic expansion discharges. Note: the discharge voltage is the voltage read from the power supply, not the voltage after the ballast resistor.

the source mount and plastic caps were added to the screw heads to prevent this arcing.

Initial spectroscopy was attempted with double-pass wavelength modulated frequency modulation spectroscopy (wm-FMS). Calculations indicated that a double-pass setup with heterodyne detection of the signal should be sufficient for obtaining an HN_2^+ signal. The setup is shown in Figure 4.10. The phase-modulated mid-IR DFG radiation is coupled into the source cham-

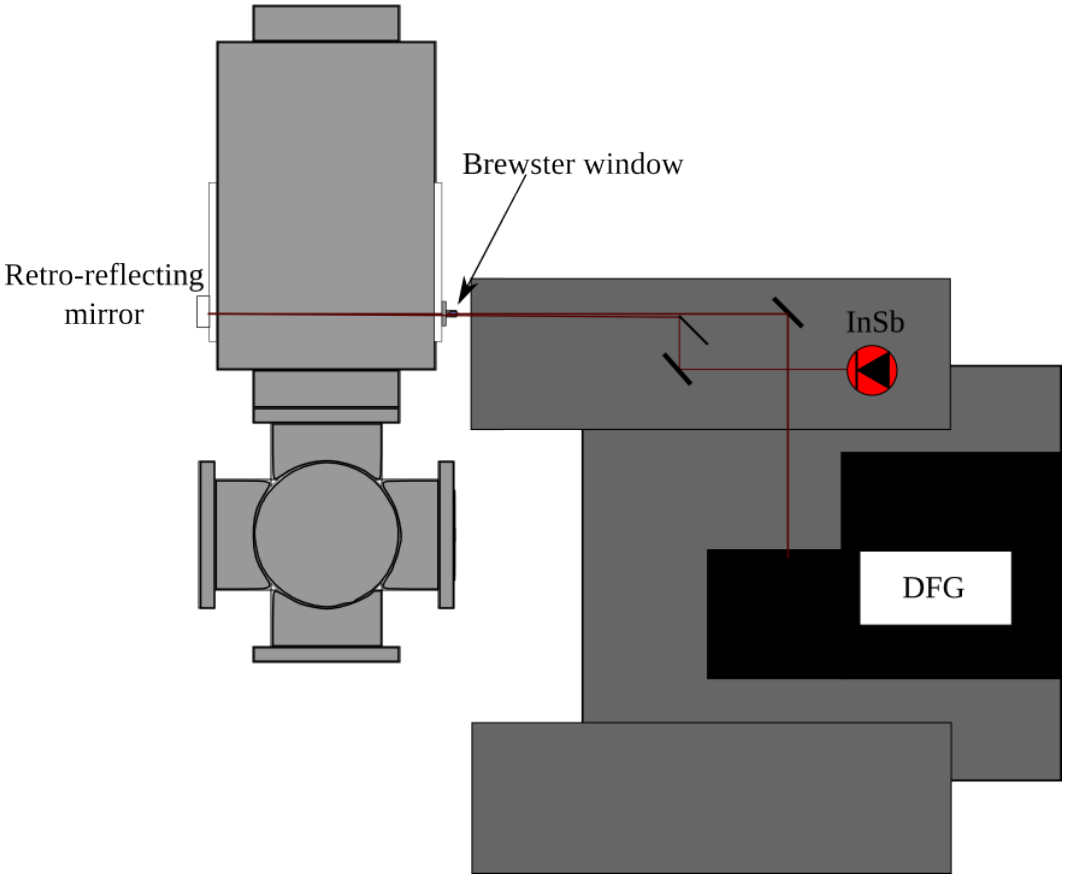

Figure 4.10: Double-pass wm-FMS setup.

ber through a CaF_2 window mounted at Brewster's angle. The DFG probes the supersonic expansion at a perpendicular angle and is then retro-reflected at a small angle (≈0.7° from the incident beam) from a plane mirror mounted inside the source chamber on the far side. The reflected beam is directed to a cooled InSb detector. The signal is demodulated using two electronic mixers set to 90° part in phase space at the frequency of phase modulation (≈ 113 MHz), as described in Chapter 2. For wavelength modulation, an 85–100 kHz sine wave was applied to the Nd:YAG laser in the DFG system to modulate the wavelength of the DFG radiation probing the sample. After demodulation of the 113 MHz signal with the mixers, the signal is demodulated again at 85–100 kHz with two lock-in amplifiers.

A variety of targets were attempted in this setup. The first target was HN_2^+. The DFG was set to record the R(1) line of the ν_1 band of HN_2^+ at ≈3240 cm^{-1}. HN_2^+ was chosen because of its low rotational constant (1.5539 cm^{-1} [84]), which indicated that the ion would cool to a lower temperature than H_3^+ (which has a rotational constant of 43.5605 cm^{-1} [85]). The HN_2^+ was produced by combining H_2 and N_2 in a tee and controlling the flow rate of each gas with commercial mass flow controllers (MKS M100B and Model 247 power supply/display). The flow rate ratio of H_2:N_2 was set to 3:1, based on the work of Reference [86]. When no signal was obtained, the mass flow controllers were abandoned for a primarily hydrogenic discharge straight from a hydrogen cylinder with a small amount of nitrogen leaked into the line straight from its cylinder with a tee. No spectral signal was obtained through this method either. H_3^+, then, was the next ion target. Although it had already been studied in the source and does not cool to as low a temperature as HN_2^+, H_3^+ can be synthesized more easily by simply flowing hydrogen through the source. The DFG was set to scan the Q(1,0) transition of the ν_2 band at 2529.724 cm^{-1}. In order to increase the signal, the wavelength modulation amplitude was increased to a value closer to the linewidth of the transition (≈ 500 MHz, based on Reference [44]). This required amplifying the signal to the Nd:YAG with a piezo driver. With this piezo driver, the full range of the Nd:YAG internal piezo could be modulated, resulting in a modulation amplitude of 100–200 MHz. It was expected that this amplitude would be enough to observe a signal. However, no signal was observed.

Because of the inability to see a signal with wm-FMS, cavity ring-down spectroscopy (CRDS) was explored as an alternative. CRDS would possess

higher sensitivity, and it was used to detect H_3^+ from the same supersonic expansion discharge source [44]. H_3^+ would be the first target for CRDS of the source, verifying with the same spectroscopy the temperature obtained in Reference [44]. Then, as with wm-FMS, spectroscopy of a molecular ion that cools to a lower temperature would be probed. Because the transitions of HN_2^+ are outside the reflectivity specifications of the ring-down mirrors that cover the H_3^+ ν_2 band, SH^+ was proposed as an alternative. Its fundamental vibrational band has lines from 2265–2599 cm^{-1} [87], accessible with the DFG and within the specifications of the ring-down mirrors (2298–2793 cm^{-1}). The SH^+ could be made through a He/H_2S discharge [87, 88].

However, due to concerns about the complexity of the instrument at this point and the realization that many scientifically interesting molecular ion targets could be detected in the supersonic expansion discharge source directly without the ion beam, the sensitive technique of NICE-OHMS was implemented on the source directly. As the direct absorption technique with, in principle, the greatest sensitivity, NICE-OHMS would enable the detection of even smaller number densities in the source than CRDS. The complexity of this system would be greatly diminished, as no steering through another set of steerers and the possibility of heating during transmission would be encountered.

4.5 NICE-OHMS of the Supersonic Expansion Discharge Source

4.5.1 Verification of Rotational Temperature Analysis

The mid-IR NICE-OHMS spectrometer described in Chapter 2 was used to probe the supersonic expansion discharge source. For this, the orientation of the source chamber and the optics table was rearranged so that the source chamber was placed in between the NICE-OHMS cavity mirrors (see Figure 4.11). In this setup, the source chamber is placed in between two optical breadboards that extend from the optics table. At the end of these breadboards are the concave mirrors (1 m radius of curvature) that form the optical cavity for NICE-OHMS. A CaF_2 beam splitter is used to catch the

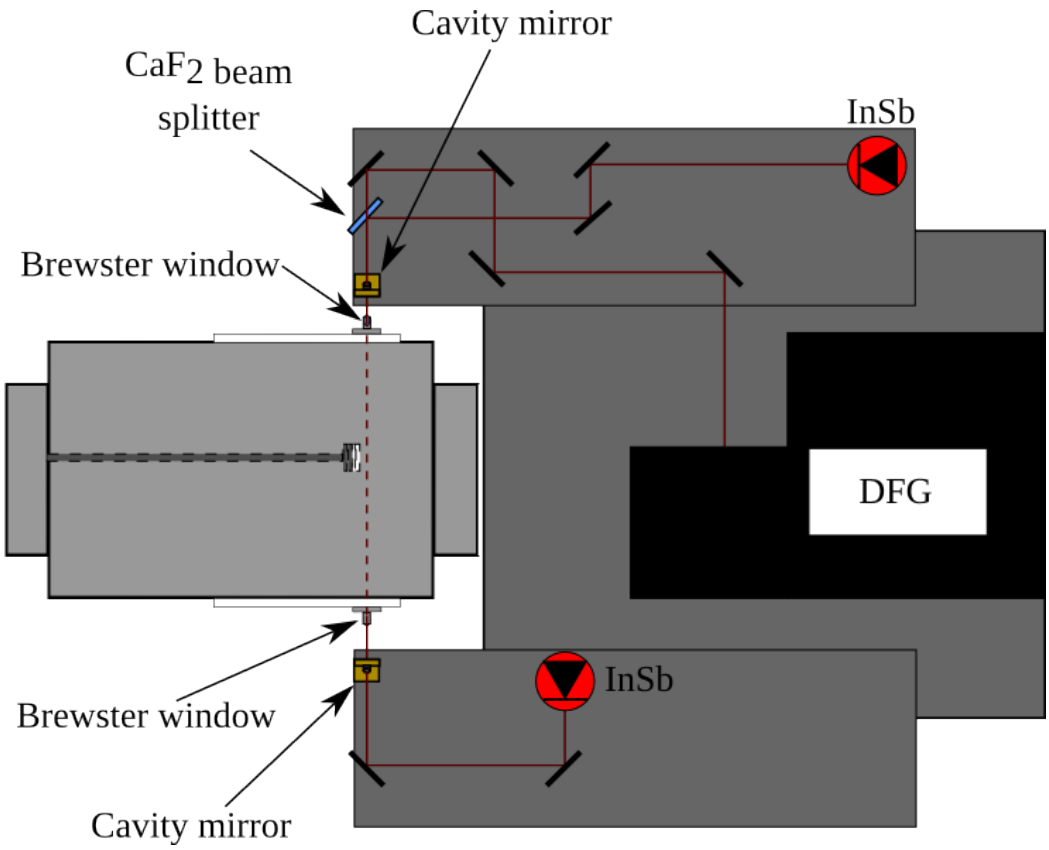

Figure 4.11: Instrumental layout of the NICE-OHMS spectrometer applied directly to the supersonic expansion discharge source.

back-reflection off of the cavity to direct it to a 30 MHz bandwidth InSb photodetector for Pound-Drever-Hall (PDH) cavity locking [60]. The laser transmitted through the cavity when locked is detected by a 120 MHz bandwidth InSb photodetector and sent to the heterodyne signal processing train described in Chapter 2.

Because one of the goals of studying the molecular ions formed by the supersonic expansion discharge source is to estimate a rotational temperature of the sample, one of the first tests of this system was to verify that an accurate rotational temperature could be determined with NICE-OHMS. The lineshapes and intensities of NICE-OHMS signals can be quite complicated, and verification that this technique could be used for temperature measurements seemed necessary. Rather than obtaining a molecular ion signal first, a verification experiment was performed by acquiring rovibrational transitions of room temperature methane and performing a Boltzmann plot analysis of the transitions. After plotting the natural logarithm of the line

strength-normalized intensities by the lower state energies of the transitions, the slope of a linear fit to the plot is inversely proportional to the rotational temperature. Natural gas from the laboratory tap was leaked into the source chamber to provide a sample of methane for the experiment. Table 4.2 shows the transitions that were acquired.

Rovibrational Transitions of Methane for Boltzmann Plot

Transition	Frequency (cm^{-1})	Einstein A coefficient (s^{-1})[a]
P(3)A_2	2988.795	34.47
P(6)A_2	2958.536	22.05
P(7)A_2	2948.107	21.05
P(9)A_2	2926.700	20.51

Table 4.2: Transitions obtained from the ν_3 band of methane for a Boltzmann plot using NICE-OHMS. [a]Einstein A coefficients obtained from HITRAN database [89].

In the initial scans of methane, the spectra contained discontinuities that would affect the Boltzmann plot analysis, as shown in Figure 4.12. These dis-

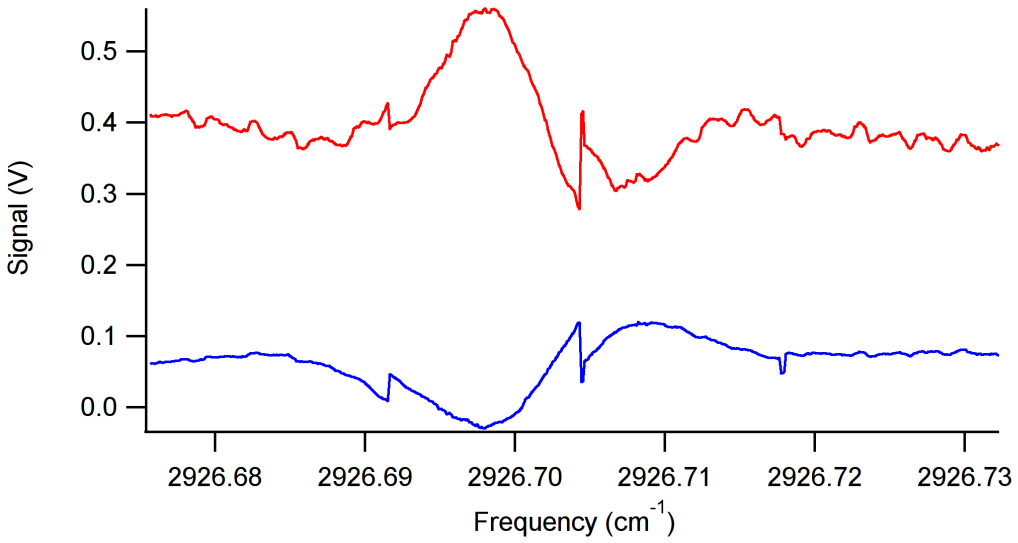

Figure 4.12: fm-NICE-OHMS spectrum of methane line. The two channels are separated by 90° in phase space. The narrow "spikes" throughout the scans coincide with pausing and re-locking the laser to the cavity.

continuities were mitigated, but not completely eliminated, through several methods of keeping the lock stronger. These methods included adjusting the filtering and amplification of the error signal, probing a more dilute sample

of methane to keep the error signal strong, improving the mode structure of the optical cavity to prevent mode-hopping, increasing the modulation amplitude to the locking EOM, and scanning more slowly with higher lock-in amplifier time constants to prevent the cavity lock from being lost. Implementing these methods resulted in only about one discontinuity per scan, generally on the line. In order to obtain the necessary intensity information for a Boltzmann plot, the starting point of the scan was adjusted so that the the peak-to-peak intensity of the line would be in one sweep of the piezoelectric transducer on the cavity. In other words, the scan was run so that the discontinuity would not occur between the maximum and minimum value of the line.

When initial Boltzmann plots yielded incorrect temperatures, other aspects of the setup were modified to obtain the room temperature value. Rather than a static cell setup in which the methane gas was leaked in and then closed off, a flowing cell system was used in which the gas was continually flowing and evacuated by a vacuum pump. With this flow cell, the pressure was kept constant by controlling the flow rate into the chamber with a needle valve, allowing the system to be more uniform. In addition, the sample pressure was lowered to ensure all measurements were conducted in the optically thin regime ($\leq$10% absorption). Because of the low number density of the sample in this regime, the more sensitive wm-NICE-OHMS was used instead. Finally, with the low number density, saturation of the NICE-OHMS signal became a concern. Saturation would have the effect of lowering the intensity of the absorption signals inconsistently across different lines. However, dispersion signals are minimally affected by saturation. Therefore, the detection phase of the system was adjusted in order to set one channel as close to dispersion as possible. With these additional modifications, a Boltzmann plot analysis yielded a rotational temperature of 300 ± 28 K, where 28 K is the uncertainty in the fit. The Boltzmann plot, along with an example wm-NICE-OHMS methane signal, is shown in Figure 4.13. The details of the Boltzmann plot calculation are in Appendix E.

With the Boltzmann plot analysis verifying that an accurate rotational temperature could be estimated from the NICE-OHMS intensities, NICE-OHMS was applied to the supersonic expansion discharge source itself. H_3^+ was the intended target, again due to its simple production. While performing methane wm-NICE-OHMS spectroscopy for the Boltzmann plot, periodic

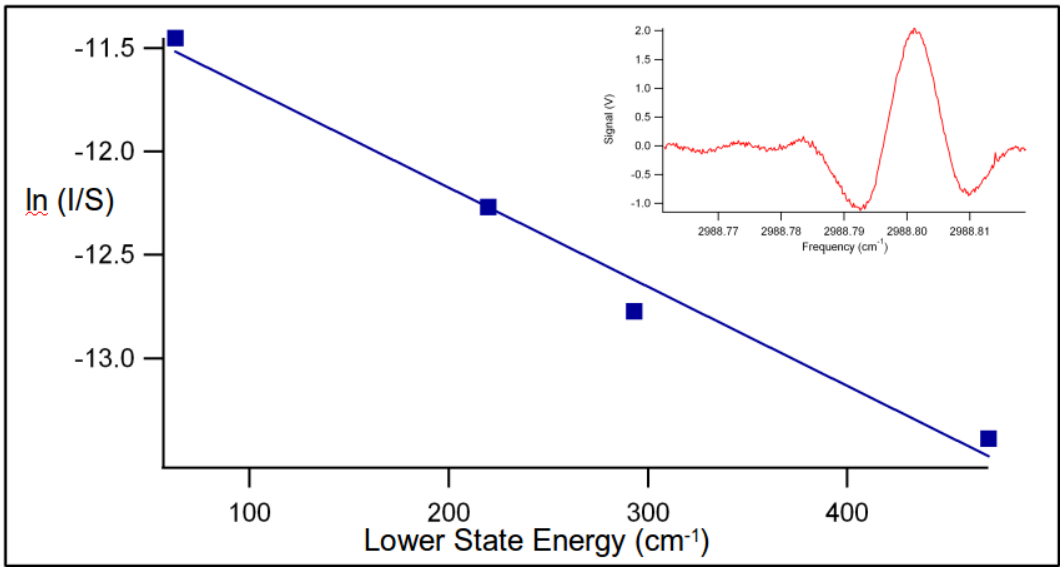

Figure 4.13: Boltzmann plot of methane transitions, where I is the peak-to-peak intensity of a line and S is the product of the Einstein A coefficient and upper state degeneracy for each line. Inset: a sample wm-NICE-OHMS signal from the P(3)A_2 line of methane.

fringing was observed. While this was not an issue for strong methane lines, the fringing was strong enough to mask an expected H_3^+ signal. Therefore, an alternative method of modulating the system was implemented.

4.5.2 Discharge Modulation

Rather than modulating the wavelength of the DFG to increase the sensitivity, the discharging of the expansion was modulated. This was done by constructing a circuit that uses an insulated-gate bipolar transistor (IGBT) to modulate the voltage to the cathode of the source at a frequency of 1–10 kHz. An electrical diagram of the circuit is shown in Figure 4.14. The circuit design and implementation were undertaken with the useful collaboration of Tom Houlahan, Jr., in the Electrical and Computer Engineering Department.

In the circuit, a TTL modulation signal from a function generator is used to trigger the switching of the IGBT. The function generator is isolated from the high voltage by an optocoupler. In this system, the voltage endurance specification of the optocoupler is essential and should be significantly larger than the high voltage applied to it as the ground on the output. Even if

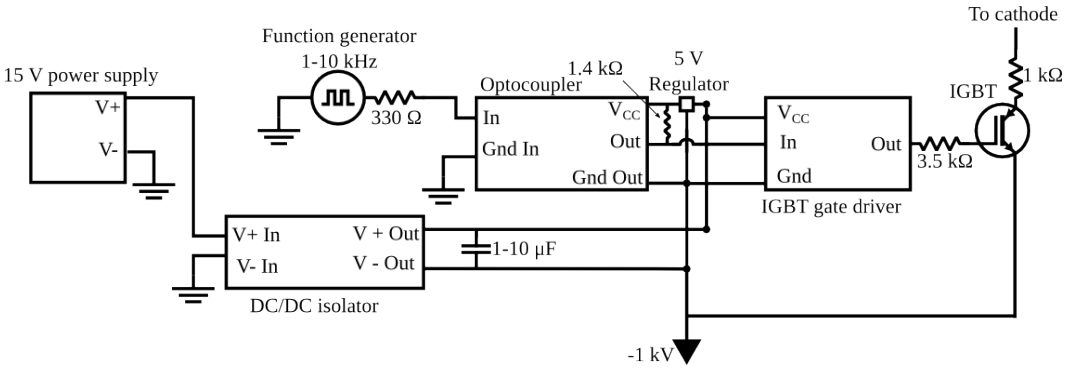

Figure 4.14: Electrical diagram of the IGBT circuit for fast switching of high voltage to the supersonic expansion discharge source. This circuit was placed in between the high voltage power supply (whose output voltage is the -1 kV ground in this circuit) and the ballast resistor (shown as here with a value of 1 kΩ) to the source. Adapted from a circuit diagram by Tom Houlahan, Jr.

the high voltage ground is less than the voltage endurance rating, voltage transients at some modulation frequencies can exceed the voltage endurance and destroy the optocoupler. Indeed, the first optocoupler model used in this circuit would invariably break when operating the circuit at low frequency, due to high transient voltage spikes produced by the high voltage power supply. A DC/DC isolator isolates the 15 V power supply from the high voltage ground of other components in the system, allowing the 15 V power supply to provide the necessary operating power for integrated circuits. The output of the optocoupler is sent to a gate driver chip to amplify the power before being sent to the gate of the IGBT. The output of the IGBT (the collector) is connected to the source via a ballast resistor. The ballast resistance was altered to 1 kΩ from 10 kΩ, in order to provide more current from the high voltage power supply while the voltage is set sufficiently low enough to avoid breaking the optocoupler. The current was varied from 30 mA up to 130 mA in a series of tests.

Modulation of the discharge with the IGBT circuit succeeded in mitigating the fringing observed with wm-NICE-OHMS. Figure 4.15 depicts a blank scan of the discharge modulated NICE-OHMS, comparing it to a blank scan of the same region using wm-NICE-OHMS. The discharge modulation clearly resulted in lower noise, showing the benefits of decoupling the modulation from the laser light. However, despite the gain in sensitivity, the noise in the discharge modulated NICE-OHMS was still too high to expect to see an H_3^+

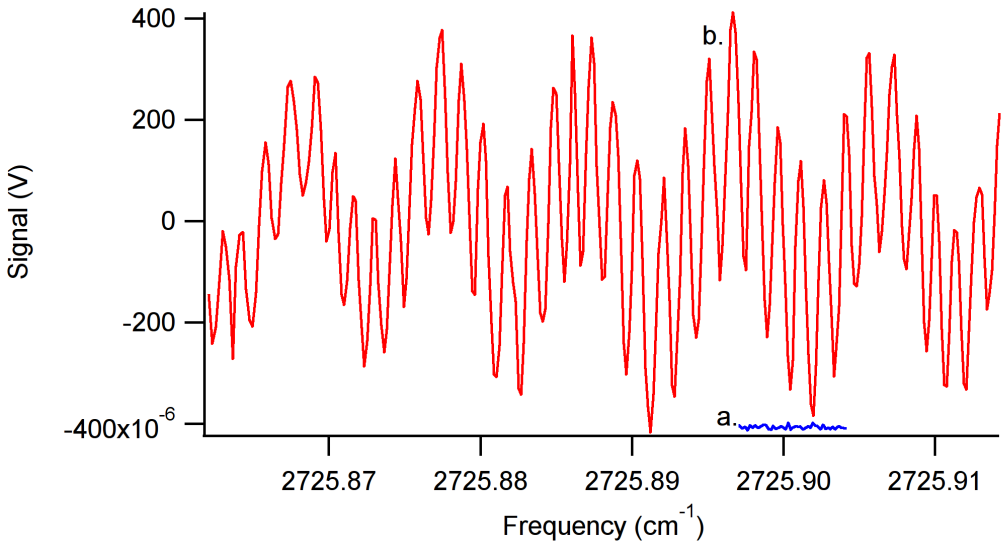

Figure 4.15: Blank NICE-OHMS scans around the R(1,0) line of H_3^+ with discharge modulation (blue, a.) and wavelength modulation (red, b.) implemented. The discharge modulation was set to 10 kHz. The wavelength modulation was implemented at 35 Hz with a modulation amplitude of 84–168 MHz. Both scans are scaled to account for their different lock-in amplifier sensitivities, and both were acquired with a 100 ms time constant.

signal. Other methods to decrease the fractional noise were thus undertaken. Reducing broadcasting from the box decreased the noise some more (in some cases, by a factor of 7–8). However, the noise was still debilitating even with the IGBT switching circuit off. An investigation into each piece of the detection system revealed that the 120 MHz InSb detector itself seemed to be outputting a broad spectrum noise. It was discovered that the high bandwidth of the detector comes at the cost of poor noise rejection; in fact, using a lower bandwidth detector (the 30 MHz InSb photodiode used for acquiring a PDH error signal) resulted in a significantly lower noise floor at the output of the detection train. Increasing the noise rejection of the 120 MHz detector was attempted, but unsuccessful. Useful gains in sensitivity, however, were made by optimizing the DFG power on the detector.

Increasing the focusing of the DFG beam on to the 120 MHz detector resulted in even lower fractional noise in the system. Because the detector has such a high bandwidth, the photodiode element is only 0.1 × 0.1 mm in area. Thus, in order to obtain a maximum signal, the DFG spot size must be lower than 0.1 mm in diameter. Therefore, by using the optical layout simulation

application OSLO [90], a beam- expanding Keplerian telescope was designed to expand the beam before focusing it on to the detector element. Expanding the beam before focusing results in a tighter focus. Knife-edge measurements using the 10/90 diameter (that is, the displacement of the knife-edge between the positions where the photodetector reads 90 and 10% of the total beam signal) verified the size of the beam. A commercial pyroelectric beam profiler failed to give an accurate beam diameter reading at this size (the target beam diameter was less than 16 pixels on the camera). Power losses through the Keplerian telescope led to the use of a single, shorter focal length lens (f=4 cm).

With the beam focused tightly on the 0.1 × 0.1 mm detector element and by scanning at a relatively high lock-in amplifier time constant (1 s), the fractional noise was low enough to expect to observe an H_3^+ signal.

4.5.3 H_3^+ NICE-OHMS Spectra and Temperature Analysis

Rovibrational spectra of H_3^+ were obtained using discharge modulated NICE-OHMS and the DFG light source. Three lines of the ν_2 band were acquired: R(1,0) at 2725.898 cm^{-1}, $R(1,1)^u$ at 2726.220 cm^{-1}, and $R(2,2)^l$ at 2762.070 cm^{-1}. The R(1,0) and $R(1,1)^u$ lines are shown in one spectrum in Figure 4.16. A rotational temperature was estimated from measurements of the intensities of the R(1,0) and $R(1,1)^u$ lines. In order to obtain a rotational temperature close to that observed previously in this supersonic expansion discharge source [44], the backing pressure, chamber pressure, and modulation frequency needed to be optimized. A backing pressure of 31 psig and a chamber pressure of ≈100 mTorr (roughly estimated from thermal conductivity differences between nitrogen and hydrogen) optimized the cooling. In addition, a modulation frequency of 1 kHz was used, due to current modulation instability at higher frequencies (see Chapter 5). With these parameters optimized, a rotational temperature of 117±19.7 K was obtained. Details of this calculation are given in Appendix E.

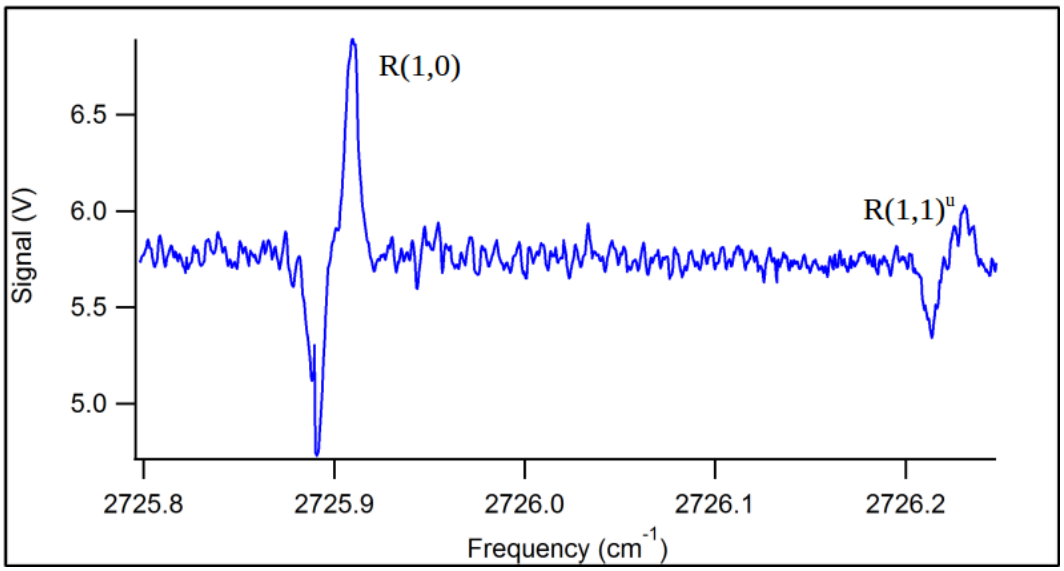

Figure 4.16: Discharge modulated NICE-OHMS spectrum of H_3^+, showing the R(1,0) and R(1,1)^u lines. Modulation frequency: 7.5 kHz. Lock-in amplifier sensitivity: 500 μV. Time constant: 1 s. Discharge current: 30 mA.

4.6 Summary and Conclusions

In molecular ion rovibrational spectroscopy, rotational cooling of the ion sample overcomes the problem of quantum dilution that plagues high temperature samples. In order to implement this cooling and apply it to an ion beam spectrometer, a continuous supersonic expansion discharge source [44] was integrated into the first couple of chambers of a redesigned mid-infrared DFG ion beam spectrometer. To accomplish this integration, a mount for the source, graphite beam skimmers, and a skimmer mount were designed and implemented in the source chamber. Initial tests of skimming the supersonic source resulted in the transmission of $\approx$2 μA of ion current at a significant nozzle-skimmer distance but inconclusive data close to the expected optimum skimmer-nozzle distance due to high pressure in the downstream chamber.

While a layout for the ion beam spectrometer with the supersonic expansion discharge source as the ion source was planned, analysis of the pressure in downstream chambers led to initial tests of the source being performed in just the first two chambers, with the hope for easier optimization of pressure conditions. Successful discharges of nitrogen and hydrogen using the source were observed. Spectroscopic studies of the source directly before

ion beam extraction were attempted using wavelength modulated frequency modulation spectroscopy to determine an estimated rotational temperature of the source, but were unsuccessful in detecting HN_2^+ or H_3^+. Cavity ring-down spectroscopy of the source was briefly explored to verify the rotational temperature of a sample with H_3^+ and SH^+.

Instead, the layout for the ion beam spectrometer was put on hold, and the source chamber and optics table were rearranged to perform NICE-OHMS on the supersonic expansion source itself. Accurate rotational temperature estimates of methane in the source chamber were acquired with wm-NICE-OHMS, but large fringing precluded detection of a molecular ion with this system. To decouple the second layer of modulation from the DFG beam in an attempt to mitigate the fringing, a discharge modulation circuit based on an insulated-gate bipolar transistor was used to modulate the discharge of the source while allowing for continuous flow of the gas. While this circuit mitigated the large fringing and decreased the overall noise in the detection, the noise was still too large to expect a molecular ion signal. Noise reduction methods such as eliminating broadcast from the new circuit and optimizing the DFG beam size on the detector brought the noise level down sufficiently to observe NICE-OHMS signals. H_3^+ spectra with discharge modulated NICE-OHMS were observed, and a rotational temperature matching the work of Reference [44] was determined.

In summary, while early work on the integration of the supersonic expansion discharge source was attempted but redirected due to unforeseen challenges, this work has successfully applied a form of concentration modulation NICE-OHMS to a supersonic expansion source for the first time (as had been proposed in the literature [43]), and thus has paved the way for the use of this sensitive method for studying cooled molecular ions.

CHAPTER 5

MID-INFRARED NICE-OHMS DEMONSTRATING ROTATIONAL COOLING OF HN_2^+ IN A CONTINUOUS SUPERSONIC EXPANSION DISCHARGE SOURCE

5.1 Introduction

The spectroscopic study of molecular ions continues to be an active area of research. These species play important roles in the chemistry and physics of combustion [91,92], atmospheric chemistry [1], and interstellar chemistry [5], among other fields. Laboratory spectroscopy is a useful and important tool for the study of molecular ions in these and other areas of interest. However, many challenges in performing spectroscopy of molecular ions in the laboratory need to be overcome. One challenge is the often-times low number density of ions in the sample to be probed. Only a fraction of the precursor gas is ionized, resulting in a low sample size, and thus, a low signal. Relatedly, because only a fraction of the gas is ionized, the majority of the sample consists of neutral molecules which will also be probed. Therefore, a method of discriminating between neutral and ionic spectral signals is often needed for molecular ion spectroscopy. Finally, most discharge sources for laboratory spectroscopic study produce these ions at high internal temperatures, resulting in smaller signals and a more complex spectrum due to quantum dilution. Effective acquisition of molecular ion spectra requires that some or all of these challenges be surmounted.

Over the past few decades, different techniques have been developed to overcome these challenges inherent in molecular ion spectroscopy. For example, discrimination between ion and neutral spectral signals has been achieved through velocity modulation spectroscopy [16]. In this technique, modulated

This chapter is to be submitted for publication with authors M. W. Porambo, C. N. Talicska, and B. J. McCall. The majority of this chapter was written by M. W. Porambo; Section 5.2 was chiefly authored by C. N. Talicska.

absorption signals from ions in an AC discharge are obtained through lock-in detection at the frequency of the AC discharge. To overcome the obstacle of low ion number density in the sample, a variety of highly sensitive spectroscopic techniques have been applied to molecular ions. These include cavity ring-down spectroscopy (CRDS) [21,22], frequency modulation spectroscopy (FMS) [26], and cavity-enhanced absorption spectroscopy (CEAS) [23–25]. Cavity-enhanced techniques such as CRDS and CEAS increase the optical pathlength through the sample, increasing the signal detected. FMS, on the other hand, significantly decreases the technical noise in the detected signal (theoretically, down to the shot noise limit). In both instances, the overall sensitivity of detection can be increased. FMS and CEAS were combined into one technique called noise-immune cavity-enhanced optical heterodyne molecular spectroscopy (NICE-OHMS) [27, 28] for even greater sensitivity. This NICE-OHMS technique was combined with velocity modulation spectroscopy for ion-neutral discrimination detection of molecular ions [19], and has been extended into the mid-infrared with broad tunability [20]. This technique was also applied to a fast ion beam spectrometer for ro-vibronic spectroscopy in the near-infrared [30]. Finally, the challenge of quantum dilution at high internal temperatures has been addressed with low temperature ion sources. These include cryogenically cooled hollow cathode [35, 36] and positive column discharge sources [20], cryogenic ion traps [93], and buffer gas cooling sources [76, 77]. Supersonic expansion discharge sources [38–43] can also achieve very low internal temperatures. In addition, these supersonic expansion discharge sources have the ability to effectively produce ions that other discharge methods can not, such as primary ions and ionic clusters. We have developed a continuous supersonic expansion discharge source [44] that has been characterized with the simple molecular ion H_3^+. Combinations of several of these techniques together can be especially powerful for accomplishing the sensitive detection of molecular ions.

This paper describes the implementation of discharge modulation on the continuous supersonic expansion discharge source described in Reference [44] and demonstrates effective rotational cooling with this source through analysis of HN_2^+ ro-vibrational spectra with NICE-OHMS. To our knowledge, this is the first time that the highly sensitive technique of NICE-OHMS has been applied to a supersonic expansion source. A Boltzmann plot analysis of several HN_2^+ transitions indicates a rotational temperature of $\sim$ 30–40 K,

extending the work of Reference [44] to an ion that cools efficiently. The rotational temperature is comparable to what has been achieved in similar discharge sources but probed with different spectroscopic methods. The combination of a highly sensitive technique with a method for producing cooled molecular ions has great promise for detecting primary ions and ionic clusters.

5.2 Experimental

Mid-IR NICE-OHMS is performed using an instrumental set-up previously described in detail [94]. Briefly, light tunable from 2.5–4 μm is produced by difference frequency generation (DFG) between a fixed-wavelength Nd:YAG (1064 nm) and tunable Ti:Sapph (700–1100 nm) laser in a periodically poled lithium niobate (PPLN) crystal. The light is coupled into an $\sim$ 1 m long cavity formed by identical spherical mirrors with high reflectivity in the 3.0–3.4 μm range and is locked to the cavity by the Pound-Drever-Hall method. To keep the DFG locked to the cavity while scanning slow corrections are made to the cavity length by a piezo controller (up to 70 Hz) and fast corrections are achieved by a double-pass acoustic optical modulator setup ($\sim$ 60 kHz) on the Ti:Sapph. Light transmitted through the cavity is focused onto a 120 MHz InSb detector (Kolmar) before being filtered and fed into two lock-in amplifiers fixed to be 90 degrees out of phase with each other. The signal from the lock-ins is then recorded by a custom data acquisition program. In this variation of the NICE-OHMS technique, an extra layer of modulation is achieved by electrically modulating the discharge via a square wave sent to a high voltage modulation circuit. The lock-in amplifiers are thus referenced to the function generator providing this gate signal, and the desired signal is demodulated at this frequency.

The overall design of the supersonic expansion source used in this work has also been described in detail in an earlier publication [44]. While the cathode used in this work has retained the dimensions and shape described there, it has been replaced by one machined from tungsten (previously stainless steel) in the hope of further improving the robustness of the source. It has been found previously that the density of H_3^+ ions produced varies with current supplied to the source (10^{10}-10^{12} cm^{-3} for 30–120 mA, respectively), and HN_2^+

was expected to be formed in similar quantities in a predominately hydrogen expansion. To help preserve the lifetime of the source in this study scans were run almost exclusively at 90 mA, which required -600 V be supplied from the power source to the cathode through a 1 kΩ 100 W ballast resistor.

Key to this study was the integration of a homebuilt high-voltage modulation circuit, shown in detail in Figure 4.14. In short the circuit uses an optoisolator (Avago ACNV2601) to separate the low-voltage input from the function generator from the high-voltage supplied by the power supply. The output of this optoisolator is then fed into a gate-driver (ON Semiconductor MC33153) for an insulated-gate bipolar transistor (IGBT) (Infineon IHW30N160R2) before being output through the ballast resistor to the cathode of the source. Measurements of signal intensity showed that at a 1 kHz modulation frequency the ion signal obtained was quite strong, and scans were conducted at this frequency for the majority of the study. The abilities of the modulation box were verified for modulation frequencies ranging from ≈25 Hz–85 kHz, with the circuit breaking down in the low frequency regime due to high transient voltage spikes. The modulating current requires a minimum amount of time to stabilize during a half-period of modulation. Therefore, the current (and the concentration of the molecular ions) will be more stable during a half-period of the modulation at lower modulation frequency. Figure 5.1 shows the output of the modulation circuit as read by a commercial Hall effect sensor at two different frequencies. To produce H_3^+ in the expansion, pure hydrogen was used at a backing pressure ranging from 30-36 psig. Significant cooling (80–120 K) was seen when the backing pressure was controlled to remain between 32-34 psig. The formation of HN_2^+ in the expansion utilized two gas cylinders (H_2 and N_2) that were individually regulated to control their respective gas flows before being combined by a Swagelok stainless steel tee just before being fed into the main pipeline of the source. The relative backing pressures between the two gases seemed to have an effect on both the intensity and shape of the obtained NICE-OHMS signal, with a mixture of 34/30 psig (H_2/N_2) giving the highest signal and least complex lineshape.

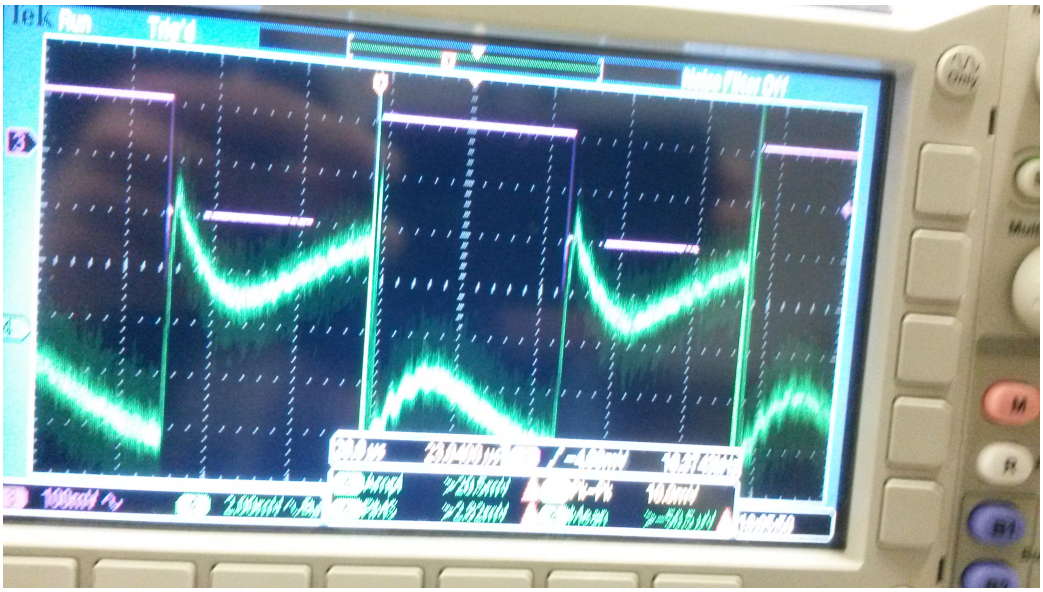

(a)

(b)

Figure 5.1: Oscilloscope traces of a Hall effect senor measuring the current output of the high-voltage modulation circuit (bottom, green) and the function generator output providing the trigger signal for the modulation circuit (top, pink) a. Modulation frequency of 10 kHz. b. Modulation frequency of 1 kHz.

5.3 Results and Discussion

Figure 5.2 shows a representative HN_2^+ scan obtained from the supersonic expansion discharge source with NICE-OHMS. The spectral line was acquired

at discharge modulation frequency of 10 kHz at a backing pressure of 34 psig. The discharge current was about 90 mA with a voltage of −600 V applied to the cathode. The rather complex lineshape is believed to be due to the convolution of two different velocity distributions in the expansion. One distribution is manifested as a red-shifted signal by the Doppler effect, and the other is manifested as a blue-shifted signal. The Doppler shift of each velocity distribution is just enough to cause interference between the two lineshapes. The lineshape was modeled with the equation:

$$S = y_0 + A\Big[\Big(\left(\chi^{abs}_{-1,-1} - \chi^{abs}_{1,-1}\right) + \left(\chi^{abs}_{-1,1} - \chi^{abs}_{1,1}\right)\Big)\cos\theta + \Big(\left(2\chi^{disp}_{0,-1} - \chi^{disp}_{1,-1} - \chi^{disp}_{-1,-1}\right) + \left(2\chi^{disp}_{0,1} - \chi^{disp}_{1,1} - \chi^{disp}_{-1,1}\right)\Big)\sin\theta\Big] \tag{5.1}$$

where

$$\chi^{abs}_{j,k} = \frac{1}{\sqrt{1+G}} e^{-x^2} \tag{5.2}$$

$$\chi^{disp}_{j,k} = \frac{2}{\sqrt{\pi}} e^{-x^2} \int_0^x e^{t^2}\,\mathrm{d}t \tag{5.3}$$

and where $x = \frac{2\sqrt{\ln 2}(\Delta\nu + j\nu_m + ks)}{\delta\nu}$, y_0 is the offset from zero signal, A is the signal amplitude, θ is the detection phase angle of the frequency modulation, G is a saturation parameter, $\Delta\nu = \nu - \nu_0$ is the detuning of the laser frequency ν from the line center ν_0, ν_m is the modulation frequency for the heterodyne signal processing, $\delta\nu$ is the linewidth of the transition (FWHM), and s is the Doppler shift of each velocity population from line center. This equation models two NICE-OHMS signals with ν_0, ν_m, $\delta\nu$, θ, A, G, y_0, and s as fitting parameters. The fitted Doppler shift s is ≈ 240 MHz. For a mainly hydrogen expansion, this corresponds to a velocity of 750 m/s.

At present, there is no firm understanding of why seemingly two velocity populations in the expansion would have such a large Doppler shift. Davis et al. [43] reported small effects of a non-uniform velocity distribution on an H_3^+ signal obtained in a hydrogen expansion from a concentration-modulated slit-jet source. A much more striking effect is observed in this work, however. An expansion in which an outer ionized shell surrounds a neutral inner core may explain the observed lineshape. In this scenario, the laser probes a population of ions with substantial velocity against its direction of propagation when it first enters the expansion, and it then probes a population of ions with velocity directed away from its direction of propagation when

it exits the expansion. This would result in both a redshift and blueshift of the signal. At certain velocities of these populations against and with the laser propagation, the two shifted signals would blend, forming the observed lineshape. Evidence in support of this hypothesis includes an observed normal NICE-OHMS signal when the edge of the expansion (as opposed to the center) is probed. This normal signal may be observed because the velocity in the direction of the laser is less at the edge of the expansion. See Figure 5.3. Recent column density measurements seem to indicate that the entire expansion is ionized, however. Another explanation may be that the probe laser and the expansion are not orthogonal. A Doppler splitting would occur in the optical cavity, with the forward-propagating beam detecting a red shift and the counter-propagating beam detecting a blue shift (or vice versa). The angle between the expansion and the probe laser may only be enough to cause an unresolved Doppler splitting. A smaller or immeasurable Doppler splitting is observed when the edge of the expansion (as opposed to the center) is probed, again as shown in Figure 5.3.

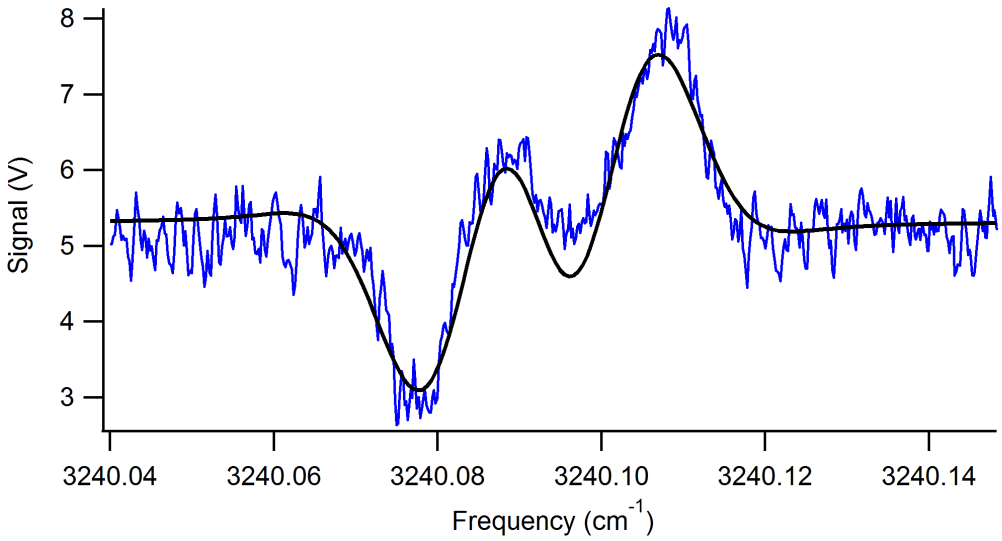

Figure 5.2: R(1) transition of the ν_1 band of HN_2^+ obtained with discharge modulated NICE-OHMS. The black line is a fit to the line assuming two Doppler-shifted velocity populations of ions are probed.

The transitions acquired for a Boltzmann plot are shown in Figure 5.4, with the Boltzmann plot from this data shown in Figure 5.5. The lower state energies for each transition were calculated using the formula for rotational energy levels and the rotational constants reported in [84]. The observed

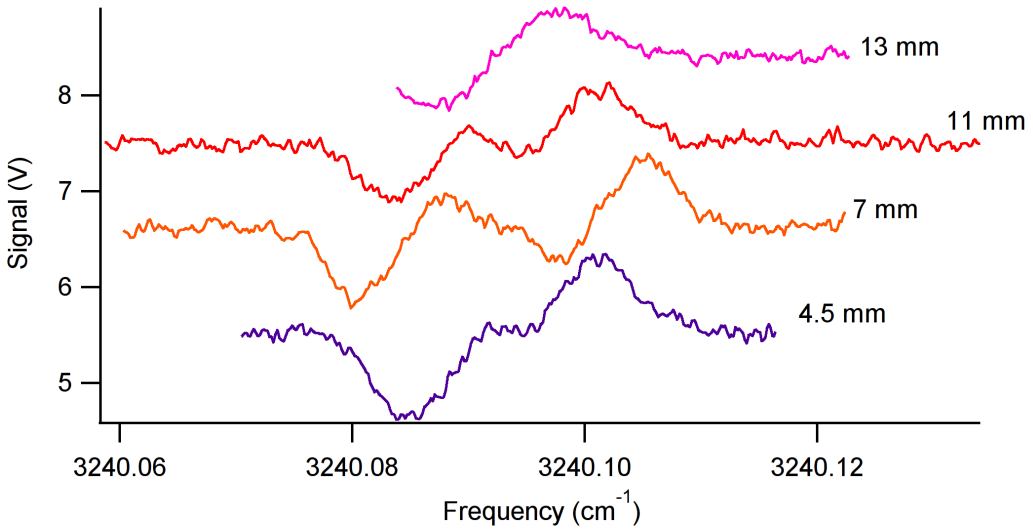

(a)

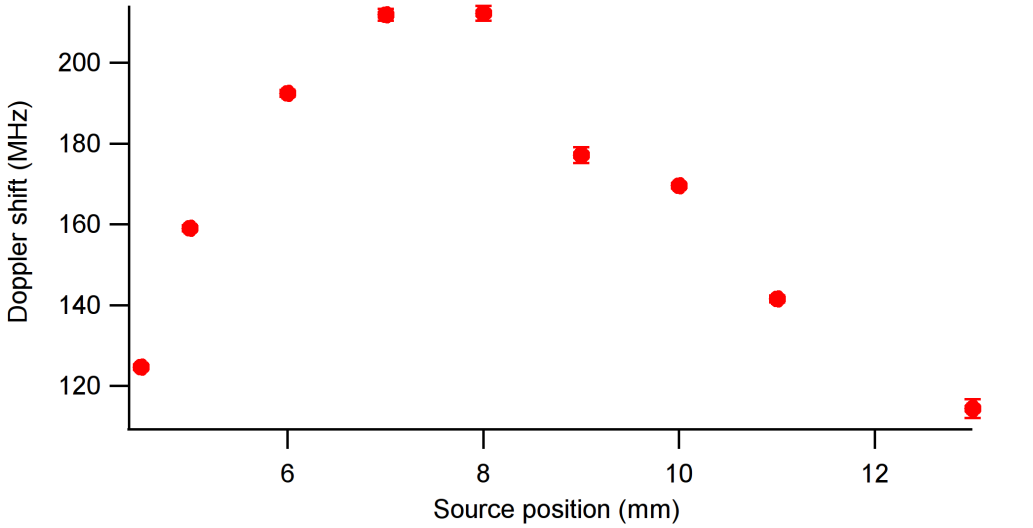

(b)

Figure 5.3: a. Scans of the R(1) transition at different vertical positions of the source (13 mm is on the edge of the expansion). b. A plot of the fitted Doppler-shift as a function of vertical source position.

peak-to-peak intensities are normalized to the transition dipole moments of each line as calculated from Equation 2-15 of Reference [95] and a permanent dipole moment of 3.4 D [96]. The slope of a linear fit to the Boltzmann plot is inversely proportional to the rotational temperature. With this Boltzmann plot, the rotational temperature was determined to be ≈36 K.

The rotational temperature of HN_2^+ determined from this source is fairly

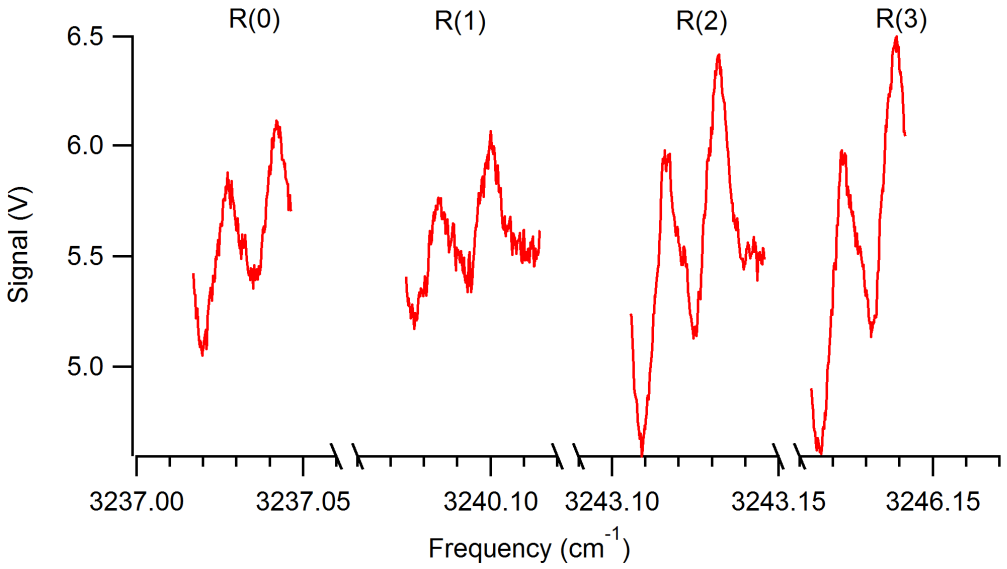

Figure 5.4: R(0) through R(3) of the ν_1 band of HN_2^+ used for a Boltzmann plot analysis to estimate the rotational temperature of the sample.

comparable to temperatures determined using the same Boltzmann plot technique in the mid-infrared in other sources. Yunjie et al. [41] obtained a temperature of 33 K for HN_2^+ in a corona slit nozzle discharge expansion. Two temperature regimes were actually observed in their Boltzmann plot for low and high J values. In a Boltzmann plot of just the low J values (J=0-3, as shown in Figure 5.5), the rotational temperature determined in this work is ≈36 K. In a pulsed slit discharge, Anderson et al. [42] obtained a temperature of 25 K for HN_2^+ at low J values.

Another concentration modulated supersonic expansion discharge source was reported in Davis et al. [43], though this source utilized a slit orifice instead of a pinhole. Ro-vibrational signals were obtained of H_3^+ at high signal-to-noise ratio [43], and subsequent studies with this source determined temperatures of H_2D^+/D_2H^+ [97], HD_2O^+ [98], and H_2DO^+ [99] to be ≈71 K, 34 K, and 40 K, respectively. The latter two temperatures are comparable to what has been obtained in the present source for HN_2^+, while the temperature obtained from H_2D^+/D_2H^+ is comparable to the temperature obtained for H_3^+ [44].

While the temperature obtained for HN_2^+ in this work is similar to the temperatures of molecular ions obtained in other work, the temperature is much lower than the rotational temperature reported for H_3^+ in the same source [44]. That work was done with no concentration modulation and with

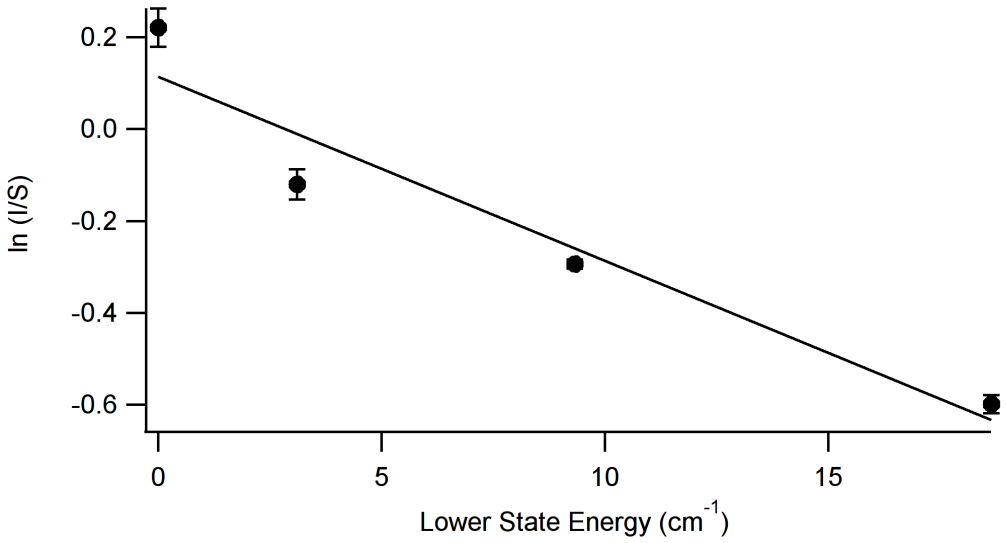

Figure 5.5: Boltzmann plot of HN_2^+ transitions. From the slope of the linear fit to the plot, the temperature is estimated to be ≈36 K.

cavity ring-down spectroscopy. Yunjie et al. [41] also observed a higher rotational temperature for H_3^+ (77 K) than for HN_2^+ (33 K), explaining that larger spacing of rotational levels results in more inefficient collisional energy transfer, making a set of rotational levels that are widely separated difficult to cool. These spacings will be related to the rotational constants, with a higher rotational constant resulting in larger rotational level spacings. The temperature is expected to be greater for H_3^+ than for HN_2^+, then, because of the higher rotational constant of H_3^+ (43.5605 cm^{-1} [85], compared to 1.5539 cm^{-1} for HN_2^+ [84]). Leutwyler et al. [100] have reported a similar phenomenon in supersonic expansion discharge cooling studies with H_2O^+, N_2^+, and N_2O^+, where determined rotational temperatures were 54–83 K, 25 K, and 10 K, respectively. The authors explained this pattern through the efficiency of rotation-translation (R-T) energy transfer. The R-T transfer becomes less efficient as collisions become more adiabatic, a condition that occurs when the collision time becomes long compared to the period of rotation of the molecule. This condition occurs at a higher temperature for H_2O^+ because of its larger rotational constant compared to the other two molecular ions. Similarly, H_3^+, which a larger rotational constant than HN_2^+, will enter a regime of adiabatic collisions at a higher temperature than HN_2^+. Therefore, H_3^+ will not cool to the same extent as HN_2^+, as is observed in this work. Yamazaki et al. [101], based on previous work from Pritchard et

al. [102], state that the probability of transition from one state to another is inversely proportional to the energy difference between the states raised to a power (Yamazaki et al. found the power to be 3/2 for collisions involving N_2). Therefore, the larger the energy separation between rotational levels, the lower the probability of de-exciting from higher energy states to lower energy states.

Different temperatures were determined for HN_2^+ at different expansion positions. At the vertical edge of the expansion, temperatures from Boltzmann analyses were higher, at ∼50 K. This may be due to heating at the edge of the expansion, where interaction with the expansion shock wave causes heating of the ions.

To the best of our knowledge, this work represents the first time that NICE-OHMS has been applied to a supersonic expansion discharge source. The NICE-OHMS technique has been used in the past to obtain highly sensitive spectra of molecules and molecular ions, limited in principle by shot noise. Minimum detectable absorption as low as 5.6×10^{-12} cm^{-1} Hz$^{-1/2}$ [29] has been achieved on C_2H_2. Past sensitivities on molecular ions include 2×10^{-11} cm^{-1} Hz$^{-1/2}$ on an N_2^+ ion beam in the near-infrared [30] and 9.8×10^{-10} cm^{-1} Hz$^{-1/2}$ on velocity-modulated molecular ions in the mid-infrared [20,33]. In the paper reporting the initial characterization of this system using methane [94], the sensitivity for Doppler-broadened fm-NICE-OHMS was reported as $\sim 1\times10^{-6}$ cm^{-1} Hz$^{-1/2}$ and $\sim 2\times10^{-7}$ cm^{-1} Hz$^{-1/2}$ for dispersion and absorption, respectively, and $\sim 6\times10^{-9}$ cm^{-1} Hz$^{-1/2}$ for the sub-Doppler dispersion wm-NICE-OHMS signals. It has since been discovered that these calculations did not take into account the AC/DC gain ratio of the InSb detector. Therefore, the values from the previous paper are corrected to $\sim 2\times10^{-5}$ cm^{-1} Hz$^{-1/2}$, $\sim 3\times10^{-6}$ cm^{-1} Hz$^{-1/2}$, and $\sim 3\times10^{-8}$ cm^{-1} Hz$^{-1/2}$, respectively.

In this concentration modulation setup, the highest sensitivity (lowest minimum detectable absorption) is found to be $\sim 2 \times 10^{-6}$ cm^{-1} Hz$^{-1/2}$. The theoretical shot-noise limited sensitivity [27] is $\sim 8\times10^{-9}$ cm^{-1} Hz$^{-1/2}$. The main sources of noise appear to be electronic noise that is dependent on the frequency modulation phase of detection. One source of significant noise that has been found is the InSb photodetector (Kolmar KISDP-0.1-E/KA120). Because of the high bandwidth necessary for NICE-OHMS detection (113 MHz), the detector has inherently poor noise rejection. In addition,

using a low power DFG limits the sensitivity. Improvements in the sensitivity of the system are planned by replacing the DFG-InSb optical system with one based on a cw optical parametric oscillator (OPO) and (HgCdZn)Te detector. Analysis indicates that, in principle, the sensitivity should be increased by at least an order of magnitude with higher mid-IR laser power irradiating the sample.

5.4 Summary and Future Work

In summary, efficient rotational cooling of molecular ions is demonstrated with a concentration modulated continuous supersonic expansion discharge source and NICE-OHMS system. Ro-vibrational transitions of HN_2^+ were acquired with NICE-OHMS using a difference frequency generation light source, and a rotational temperature analysis of these transitions by a Boltzmann plot indicates a rotational temperature of ≈36 K for the sample. This low temperature compares well with the cooling of similar molecular ions in pulsed discharge sources. This work also represents the first time that NICE-OHMS has been applied to a supersonic expansion source, and this system shows the promises and limits of applying NICE-OHMS to a concentration modulated supersonic expansion discharge source [43]. The limited sensitivity of $\sim 6 \times 10^{-7}$ cm^{-1} Hz$^{-1/2}$ seems to be due to limits of the mid-infrared detector and low-power light source used. Improvements in the sensitivity are planned by replacing the source and detector scheme with a cw OPO and HgCdTe detector. With a large expansion velocity, a supersonic expansion discharge source such as this is conducive for the production of primary molecular ions, which will not have enough time to react with other species present in the expansion before being probed by the laser. Future work with this source will include the study of primary molecular ions that are of interstellar interest, such as H_2CO^+.

The authors thank Jessica Pearson for work on the IGBT modulation circuit and designing the tungsten cathode, as well as Thomas Houlahan, Jr. for generous help in designing and troubleshooting the modulation circuit. The authors also thank the National Science Foundation (CHE-12-13811) and a Camille Dreyfus Teacher-Scholar Award for funding. M. W. P. acknowledges funding from the NASA Earth and Space Science Fellowship program.

CHAPTER 6

SUMMARY AND FUTURE WORK

The work presented in this dissertation has explored new instrumental setups for the spectroscopic study of molecular ions at low rotational temperatures. Molecular ions hold interest in a variety of fields, and tools to study the direct absorption spectra of ions under different conditions and at increased sensitivity can lead to insights in fields from combustion to interstellar chemistry. Two broad types of instrumental layout were explored in detail in this dissertation for the study of molecular ions: an ion beam spectrometer where ions are extracted from a supersonic expansion source, and laser spectroscopy applied to a supersonic expansion discharge source directly. An attempt was made to perform mid-infrared spectroscopy on an ion beam, but was unsuccessful. Likewise, integrating the supersonic expansion discharge source to the ion beam spectrometer was problematic. However, valuable insights were gained, and there may be reason to expect that this type of instrument may work in the future. Mid-infrared spectroscopy on the supersonic expansion discharge source itself, where NICE-OHMS was applied to a supersonic expansion discharge source for the first time, was successful in acquiring low temperature spectra of simple molecular ions, and this will be the next path to pursue on the project. This chapter summarizes the main points learned on the two layouts and explores ideas for future work.

6.1 Ion Beam Spectrometer Summary and Future Work

After the successful acquisition of rovibronic transitions in the near-infrared of an N_2^+ ion beam (see Appendix A), the NICE-OHMS system was redesigned for operation in the mid-infrared with the use of a difference frequency generation light source, as described in Chapter 2. Initial attempts

of spectroscopy were attempted on a hot ion beam of H_3^+ formed from a cold cathode source, but were unsuccessful. The details and reason for this is given in Chapter 3. Spectroscopic study of the hot ion beam in the mid-infrared was intended as a preliminary step toward mid-infrared spectroscopy of a cooled ion beam, where the cooled ions are formed in a supersonic expansion discharge source. When completed, this instrument would be known as Sensitive, Cooled, Resolved Ion BEam Spectroscopy (SCRIBES), and would combine the advantages of an ion beam spectrometer (rigorous ion-neutral discrimination, mass-dependent Doppler shifts, and TOF mass spectrometry) with the advantages of a cooled molecular ion sample (stronger and less complicated spectra). The disadvantage of low ion density in the ion beam would be overcome with sensitive, cavity-enhanced spectroscopy, such as NICE-OHMS.

The completion of SCRIBES was explored, but a different direction was ultimately decided for the project. Integration of the supersonic expansion discharge source was begun by constructing a mount, beam skimmers, and a beam skimmer mount and performing tests of expansions with simple discharges of nitrogen and hydrogen. Before full integration of the supersonic expansion discharge source with the ion beam spectrometer, preliminary spectroscopy directly on the supersonic expansion discharge source was deemed necessary to compare rotational temperatures in the source itself with temperatures that would be observed in the ion beam. Wavelength modulated frequency modulation spectroscopy (wm-FMS) was used in an attempt to probe the temperature of ions in the supersonic expansion discharge source this way. This technique, however, was not sensitive enough to acquire spectra of the simple molecular ion H_3^+. Therefore, efforts were directed away from ion beam spectroscopy and concentrating on applying the sensitive technique of NICE-OHMS to the supersonic expansion source directly. Furthermore, analysis of the proposed vacuum chamber layout for SCRIBES and tests of the skimmer transmission indicate that the high pressure downstream of the skimmer will be an issue regarding arcing in the ion optics and safe operation of the vacuum pumps in that section of the instrument.

Regarding future work on a mid-infrared ion beam spectrometer using a continuous supersonic expansion discharge source, two issues will need to be addressed: effective differential pumping and sufficient sensitivity to detect the low ion number density in the ion beam. Regarding effective pumping,

a combination of lower backing pressure in the source and higher pumping speed and conductance in the downstream vacuum chamber may circumvent the issue of overly high pressure. While experiments on the supersonic expansion source here and previously [44] were conducted with 2–3 atm backing pressure, other supersonic expansion discharge source experiments have been run at a backing pressure of ∼100 Torr [43, 83]. Using a 100 Torr backing pressure in the calculation of Appendix D results in an estimated chamber pressure downstream of the skimmer of ≈4 mTorr, which may not be low enough to prevent arcing of the ion optics. However, a higher effective pumping speed could be used by increasing the conductance between the vacuum pump and the output of the skimmer.

The sensitivity of the spectroscopy setup will also have to be increased in order to acquire mid-infrared spectra of molecular ions in the ion beam setup. Dispersion signals of N_2^+ produced by a cold cathode source were obtained in an ion beam with a near-infrared spectrometer that possessed a sensitivity of 2×10^{-11} cm $Hz^{-1/2}$. The expected N_2^+ fractional signals in this system (≈2–3×10^{-6}, shown in the Supplementary Material of Appendix A) were calculated to be similar to the expected H_3^+ fractional signal obtained in Chapter 3 (2.83×10^{-6}). A signal-to-noise ratio of ≈30 was obtained for the N_2^+ signals with the near-infrared system. For a detectable signal of H_3^+ (that is, a signal with a signal-to-noise ratio of 2), a spectrometer with a detection sensitivity of at least 3×10^{-10} cm $Hz^{-1/2}$ will be required. The sensitivity may also need to be even greater for a cooled H_3^+ ion beam skimmed from a supersonic expansion. While the low temperature should increase the signal strength, loss of ion density through the skimmer and other parts of the instrument may offset the gain at low temperature.

6.2 Supersonic Expansion Discharge Source Spectroscopy

Despite the setbacks in developing an ion beam spectrometer for the study of molecular ions, there are opportunities to study interesting molecular ions directly in the supersonic expansion discharge source with NICE-OHMS. This work has applied NICE-OHMS to a supersonic expansion discharge source for the first time, developing a a path for the spectroscopy of primary ions, large

ions, and cluster ions with unprecedented sensitivity. This work has demonstrated that NICE-OHMS can be used to accurately determine the rotational temperature of a molecular and molecular ion samples through Boltzmann plot analyses of methane. NICE-OHMS spectra of H_3^+ have been obtained, repeating experiments done before in the supersonic expansion source [44], though now with a technique that has the capability to be more sensitive. Furthermore, NICE-OHMS spectra of HN_2^+, which cools more efficiently, have been acquired, demonstrating that other ions can be cooled to even lower rotational temperatures than H_3^+. In addition, because wavelength-modulation NICE-OHMS is too noisy in this system due to fringing, a form of concentration modulation of the supersonic expansion discharge source was successfully implemented. Using NICE-OHMS to probe this type of expansion is a step toward obtaining the spectra of molecular ions and radicals at new sensitivities [43].

The supersonic expansion discharge NICE-OHMS spectrometer can be improved upon in a number of ways. One method that is underway as of this writing is the upgrading of the light source from the difference frequency generation system described in Chapter 2 to a commercial optical parametric oscillator (OPO) system similar to that described in Reference [20], which is tunable in the mid-infrared from 2.3–4.6 μm through the use of several modules. This light source (Lockheed Martin Argos 2400 SF-10) possesses more power ($\approx$1 W) to probe the supersonic source, which should improve the sensitivity. In addition, the InSb detector used with the DFG beam will be replaced by a (HgCdZn)Te detector (Vigo PVM-10.6-1$\times$1). This room temperature detector will not saturate at the higher power possible with the OPO. Despite the (HgCdZn)Te detector being less sensitive than the InSb, the higher expected power of the OPO will offset the lower detector sensitivity. The sensitivity of a NICE-OHMS system is given by [27]

$$\alpha_{min} = \frac{\pi}{F}\sqrt{\frac{eB}{\eta P_0}}\frac{1}{J_0 J_1} \tag{6.1}$$

where F is the finesse of the optical cavity, e is the charge of an electron in coulombs, B is the detection bandwidth in hertz, η is the detector responsivity in amperes per watt, P_0 is the power incident on the detector in watts, and J_0 and J_1 are Bessel functions of the zeroth and first kind evaluated at

the modulation index of the phase modulation. Assuming that the cavity and detection bandwidth would be equal between the two light source-detector systems (the DFG-InSb system and the OPO-(HgCdZn)Te system), the only difference would be between the product of the responsivity and power. The responsivities and incident powers, along with the corresponding shot-noise limited noise equivalent absorptions, are given in Table 6.1. Therefore, the

Constants for H_3^+ Temperature Estimate		
	DFG/InSb	OPO/(HgCdZn)Te
η (A/W):	2.8	0.0007
P_0 (W):	3×10^{-6}	4×10^{-1}
Noise equivalent absorption:	3×10^{-9}	5×10^{-10}

Table 6.1: Properties of the DFG/InSb and OPO/(HgCdZn)Te spectrometer systems. Noise equivalent sensitivities were calculated with Equation 6.1 and assumed common variables of $F = 170$, $B = 0.125$ Hz, and J_0 and J_1 evaluated at a modulation index of 0.79. The incident power of the OPO is based from an average of what has been seen in the system of Reference [20].

minimum detectable absorption should be about 6 times lower for the OPO-(HgCdZn)Te system. The OPO idler beam path described has already been directed to the supersonic expansion discharge source via a mid-infrared optical fiber cable. Preliminary work on this has yielded a higher beam power incident on the optical cavity ($\approx$160 mW, compared to $\approx$60 μW from the DFG), and there is hope for more improvement. In addition to an expected increase in sensitivity, the commercial turnkey OPO system has a practical advantage in tuning, peaking, and maintenance compared to the DFG.

Improvements can also be made to the supersonic expansion discharge source itself. Presently, the expansion occurs through a circular pinhole (0.500 mm at its narrowest). There are advantages to using a slit orifice, which have also been used for supersonic expansion discharges [41–43, 78]. There are three main advantages to using a slit discharge [103]. First, the planar expansion provides a long pathlength of sample, increasing the signal over a pinhole expansion. Secondly, the number density does not drop off as quickly in a slit expansion as it does in a pinhole. Finally, the Doppler-broadened linewidths of transitions in pinhole expansions are broader due to higher divergence from the expansion axis. A slit orifice, then, has the

potential for stronger and narrower spectral lines.

6.3 Molecular Ion Targets

One class of molecular ions that the supersonic source should be adept at producing are primary ions, where a neutral precursor molecule loses an electron. Because of the small time period that ions are present in the discharge, it is expected that a relatively significant amount of primary ions will remain unreacted [43] and can be probed. A simple primary ion to investigate first is H_2O^+. Rovibrational transitions of H_2O^+ have been acquired for the ν_1 [104] and ν_3 [104, 105] bands between 3117–3406 cm^{-1} and 3103–3422 cm^{-1}, respectively, which is well within the range of the OPO idler. H_2O^+ ions has been formed in a discharge of $He:H_2:O_2$ (100:1:1) [105] and in a discharge of $He:H_2O$ [104], and these mixtures can be readily used in the supersonic expansion discharge source. H_2O^+ will be a simple primary ion to acquire and analyze by Boltzmann plot, demonstrating that primary ions can be formed and cooled efficiently in the supersonic expansion discharge source.

Another primary ion that is of more astrochemical interest that can be investigated with the supersonic expansion discharge source is the formaldehyde radical cation, H_2CO^+. This radical cation has not yet been detected in the interstellar medium [106], despite the observed presence of formaldehyde [13] and protonated formaldehyde [15]. While this ion has been studied computationally [107–110] and experimentally with photoelectron spectroscopy [72, 73, 111], the most precise rotational energy levels and rotational constants were only determined to within an uncertainty of ≈600 MHz [73]. The uncertainty of these values must be decreased in order to expect to determine spectral signatures of the cation in the interstellar medium [112], and high resolution mid-infrared spectroscopy obtained with great precision and accuracy would be a useful tool in this pursuit. As discussed previously in a prospectus [113], the supersonic expansion discharge source can be used to ionize cooled formaldehyde for the study of the radical cation. To produce the cooled formaldehyde, paraformaldehyde can be heated to 350–400 K [72, 73, 111] beneath an inert gas to entrain the formaldehyde vapor into the supersonic expansion discharge source. Rovibrational transitions in the ν_1 vibrational band (∼2580 cm^{-1} [72]) can be probed with the

OPO. In order to obtain rovibrational transitions at high accuracy, the optical frequency comb used in past work [19, 30, 32] can be used to calibrate the wavelength of the OPO to an accuracy of <100 kHz [20], and fitted uncertainties of Doppler-broadened signals have been as low as ∼350 kHz. The spectrum can be fit to obtain precise levels and constants that can be used for the attempted detection of this ion in the interstellar medium.

The supersonic expansion discharge source has the potential to acquire spectra of many types of primary ions and other species at low temperature, overcoming the issue of quantum dilution in laboratory molecular ion spectroscopy. By combining a highly sensitive technique in discharge modulated NICE-OHMS with this supersonic expansion discharge source, ions that are difficult to produce or study in other sources can be investigated spectroscopically using this work. The effective spectroscopic study of these types of chemical species has the potential to increase insight and knowledge in interstellar chemistry and other scientific fields of interest.

APPENDIX A

ULTRA-SENSITIVE HIGH-PRECISION SPECTROSCOPY OF A FAST MOLECULAR ION BEAM

This Appendix contains a journal article describing studies in the near-infrared on the ion beam spectrometer reprinted with permission from Mills, Andrew A.; Siller, Brian M.; Porambo, Michael W.; Perera, Manori; Kreckel, Holger; and McCall, Benjamin J., *J. Chem. Phys.*, 135, 224201, (2011). Copyright 2011, American Institute of Physics.

Ultra-sensitive high-precision spectroscopy of a fast molecular ion beam

Andrew A. Mills,[1] Brian M. Siller,[1] Michael W. Porambo,[1] Manori Perera,[1,a)]
Holger Kreckel,[1] and Benjamin J. McCall[1,2,b)]
[1]*Department of Chemistry, University of Illinois, Urbana, Illinois 61801, USA*
[2]*Departments of Physics and Astronomy, University of Illinois, Urbana, Illinois 61801, USA*

(Received 9 October 2011; accepted 13 November 2011; published online 13 December 2011)

Direct spectroscopy of a fast molecular ion beam offers many advantages over competing techniques, including the generality of the approach to any molecular ion, the complete elimination of spectral confusion due to neutral molecules, and the mass identification of individual spectral lines. The major challenge is the intrinsic weakness of absorption or dispersion signals resulting from the relatively low number density of ions in the beam. Direct spectroscopy of an ion beam was pioneered by Saykally and co-workers in the late 1980s, but has not been attempted since that time. Here, we present the design and construction of an ion beam spectrometer with several improvements over the Saykally design. The ion beam and its characterization have been improved by adopting recent advances in electrostatic optics, along with a time-of-flight mass spectrometer that can be used simultaneously with optical spectroscopy. As a proof of concept, a noise-immune cavity-enhanced optical heterodyne molecular spectroscopy (NICE-OHMS) setup with a noise equivalent absorption of $\sim 2 \times 10^{-11}$ cm^{-1} Hz$^{-1/2}$ has been used to observe several transitions of the Meinel 1–0 band of N_2^+ with linewidths of ∼120 MHz. An optical frequency comb has been used for absolute frequency calibration of transition frequencies to within ∼8 MHz. This work represents the first direct spectroscopy of an electronic transition in an ion beam, and also represents a major step toward the development of routine infrared spectroscopy of rotationally cooled molecular ions. © *2011 American Institute of Physics*. [doi:10.1063/1.3665925]

I. INTRODUCTION

The study of molecular ions is important in a number of fields, including physical chemistry, combustion chemistry, atmospheric chemistry,[1] and astrochemistry.[2,3] Ions are transient and reactive species, so even in plasma discharges, neutral molecules are typically ∼6 orders of magnitude more abundant than the ions of interest. Early spectroscopic studies on glow discharges were often hampered by interfering signals from neutral absorbers.[4] The invention of velocity modulation spectroscopy (VMS),[5] which involves using a high voltage AC discharge to modulate the velocity of ions and a lock-in amplifier to isolate the modulated ionic absorption signals from the unmodulated neutral signals, has allowed for the spectroscopic study of scores of molecular ions.[4] However, due to harsh plasma conditions, molecular ions produced in VMS experiments often have high rotational and vibrational temperatures, typically on the order of several hundred Kelvin. For example, CH_3^+ has been studied by Oka and co-workers in a liquid nitrogen cooled discharge cell, where the rotational and vibrational temperatures were reported as 371 and 700 K, respectively.[6]

Until recently,[7] all VMS experiments produced Doppler-limited linewidths. For small diatomic molecules, the spectra remain relatively simple to assign and line intensities are fairly strong, but larger (e.g., $C_3H_3^+$) or highly fluxional (e.g., CH_5^+) molecular ions are more challenging targets, as each individual transition is weaker due to quantum dilution. Supersonically expanding discharges have been used to spectroscopically study rotationally cold molecular ions, but the reduced rotational temperature comes with the price of lost ion/neutral discrimination. Although concentration modulation can provide some discrimination from background precursors,[8] radicals[9] and excited states of stable neutrals can still congest and complicate the recorded spectrum.

The limitations of current techniques are highlighted by the case of CH_5^+, a molecular ion of considerable interest due to its lack of a classical structure[10] and as the prototypical non-classical carbocation.[11] The only published high-resolution spectrum of CH_5^+ was recorded by Oka and co-workers[12] in a liquid nitrogen cooled discharge of H_2 and CH_4, and was identified by a process of elimination, by removing the known spectral lines of H_3^+, CH_3^+, $C_2H_3^+$, HCO^+, $HCNH^+$, the Rydberg spectrum of H_2, and strong lines of CH_4 that remained due to a slight asymmetry in the AC plasma. This rich spectrum (∼900 lines, due to the fairly high rotational temperature) may still contain some transitions of other ions, and almost certainly is missing some CH_5^+ transitions due to overlap with CH_4 lines. As a result of the complexity of the spectrum, it remains completely unassigned more than a decade since its publication.

Nesbitt and co-workers have recorded[13] a spectrum of a supersonically expanding H_2:CH_4 plasma, the broad outline of which has been published.[14] Their spectrum evidently

a)Present address: Department of Chemistry, Illinois Wesleyan University, Bloomington, Illinois 61702, USA.
b)Author to whom correspondence should be addressed. Electronic mail: bjmccall@illinois.edu.

contains not only many transitions that coincide with those of Oka and co-workers, but also many transitions that do not. Because of the lack of a rigorous ion/neutral discrimination, it is possible that some of these transitions may be due to excited CH_4. They have proposed[13] the use of four-line combination differences to help assign the spectrum, but this effort requires higher precision in the determination of line centers.[15]

The ideal experiment for studying the spectra of complex ions such as CH_5^+ may be a combination of a supersonic expansion ion source with fast ion beam spectroscopy. This approach offers rigorous ion/neutral discrimination (by physically separating ions from neutrals) and reduced Doppler linewidths (from kinematic compression), and also allows mass identification of each spectral line (from Doppler splittings).

Although action spectroscopy of ion beams was successfully implemented as early as the 1970s (Ref. 16), the only direct ion beam spectrometer (prior to the present work) was developed in the late 1980s by Saykally and co-workers at Berkeley.[17] This instrument was successfully used to measure the mid-IR absorption spectra of HF^+, HN_2^+, HCO^+, H_3O^+, and NH_4^+ (Refs. 17–19), but was abandoned after a few years, as it did not have sufficient sensitivity to pursue the spectra of the larger and fluxional ions they were most interested in, given the rotational temperature of uncooled ion sources.

With an eye to applications such as CH_5^+, we have embarked on an effort to construct a second-generation direct ion beam spectrometer, which incorporates a number of technological advances from the past two decades and is also designed to be fed with a continuous supersonic expansion discharge source.[20] As this approach will combine ultra-high sensitivity, rotational cooling, and very high precision line center determination, we refer to it as sensitive, cooled, resolved ion beam spectroscopy (SCRIBES).

This paper describes an important step toward SCRIBES, in the form of a new ion beam instrument that uses a Ti:Sapphire laser (the future pump laser for a mid-IR difference frequency laser) in concert with NICE-OHMS[21] as a sensitive direct spectroscopic probe of the ion beam. This instrument uses a time-of-flight mass spectrometer (TOF-MS) to provide mass analysis of constituents of the ion beam at spectroscopically relevant beam energies. An optical frequency comb is used to accurately and precisely measure the frequencies of the observed transitions.

The initial proof of concept system studied in this work is the 1–0 band of the $A^2\Pi_u - X^2\Sigma_g^+$ Meinel system of N_2^+, which is an important species in atmospheric aurorae and electrical discharges. Because the line centers of many transitions in this band have already been measured at Doppler-limited resolution,[22] N_2^+ serves as a useful benchmark of the capabilities of our fast ion beam spectrometer.

II. EXPERIMENTAL

A. Overview

Figure 1 shows an overview of the entire experimental setup, which can be divided into two functional groups: (1) the ion beam setup, including the ion source, the ion optics and the mass spectrometer; and (2) the spectroscopic setup, consisting of the laser system and signal detection electronics. The two parts of the system interact in the central overlap region, where the laser cavity and the ion beam are superimposed.

In order to minimize vibrations in the spectroscopic setup, the optical components are mounted on a pneumatically stabilized laser table that is mechanically isolated from the ion beam setup. The mirrors of an optical cavity (finesse $\mathcal{F} \sim 450$) are positioned on breadboards that overhang the edge of the laser table and surround the ion beam drift region. Within the optical cavity, the laser is coupled through Brewster windows mounted on the ion beam chamber, and is overlapped with the ion beam within the drift region.

A cold cathode ion source, described in detail in Sec. II B, is used to produce a beam of N_2^+ at energies ranging from 2–6 kV. After the beam is extracted from the source, it is focused by an Einzel lens and steered by two sets of parallel electrostatic plates into a cylindrical electrostatic double-focusing deflector.[23] When this deflector is biased, the ion beam is turned 90° and focused into the drift tube. When the deflector plates are grounded, the ion beam proceeds straight through a hole in the outer deflector plate and into a Faraday cup that is used to optimize source conditions for maximum ion current, which is generally $\sim$10 μA.

After exiting the deflector chamber, the ion beam proceeds through a 27 cm long drift tube and two metal plates that are spaced 13 cm apart, centered in the drift region. The metal plates are attached to vertical linear manipulators; each plate has three 3-mm diameter apertures that are spaced 1.5 cm vertically and 1 mm horizontally. The apertures are aligned with the laser horizontally by choosing the hole that does not spoil the cavity finesse, and vertically within a hole by fine-tuning the vertical translation of the plates. After the appropriate apertures are centered on the laser, the ion beam is steered through the same apertures to make the laser and the ion beam collinear. The drift tube and the aperture plates are all electrically isolated from the surrounding chamber and connected to one another so they can all be used to modulate the velocity of the ion beam with an applied voltage. After the drift region, the ion beam enters the second 90° bender which guides the ions out of the laser cavity into the time-of-flight mass spectrometer, which is described in detail in Sec. II D.

Optical spectroscopy of the ion beam is performed using the NICE-OHMS[21] technique, which combines the long effective path length of cavity enhanced spectroscopy with the noise suppression of heterodyne spectroscopy. Further noise suppression is obtained by modulating the velocity of the ions by applying a square wave voltage to the drift tube. A more thorough description of the detection system is given in Sec. II E.

B. Ion source

Our instrument is engineered to accommodate a continuous supersonic expansion discharge source, such as the one we have previously characterized for H_3^+ spectroscopy.[20] To utilize such a source, our ion source chamber was designed

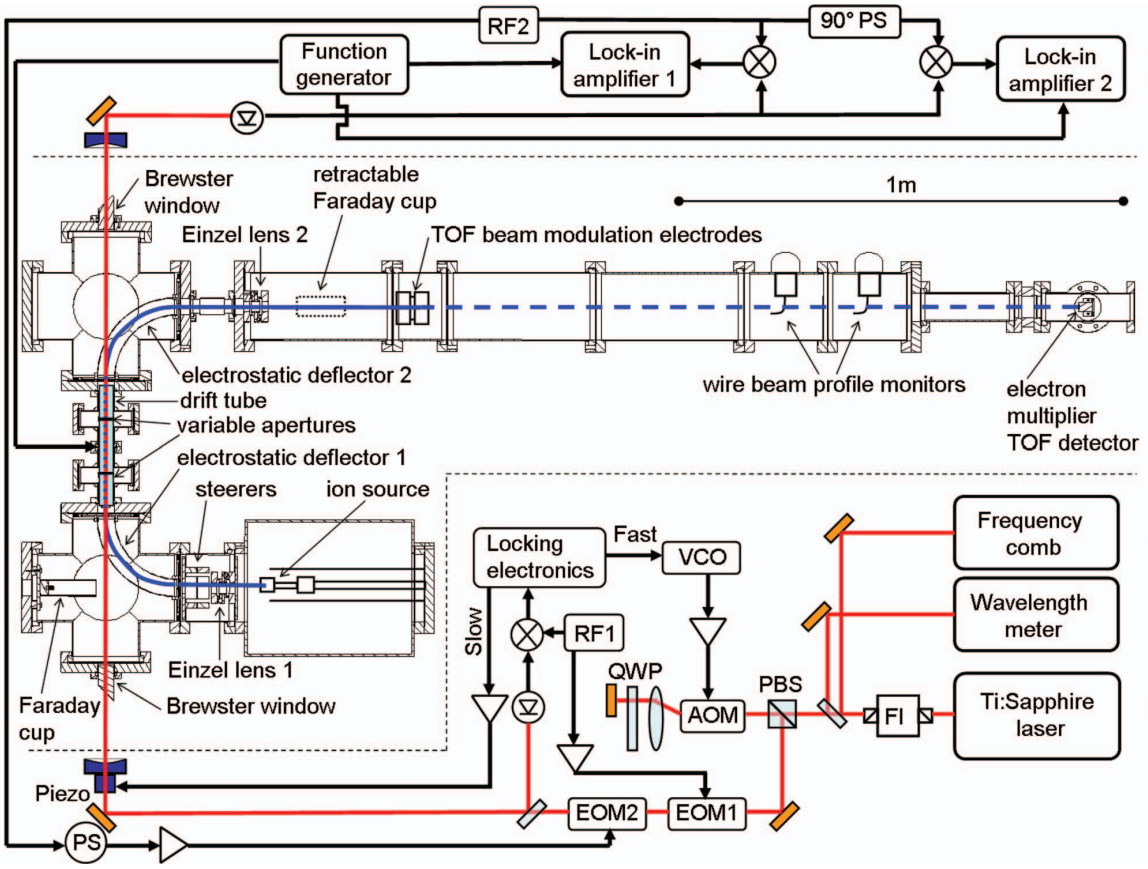

FIG. 1. Schematic of the fast ion beam spectrometer using NICE-OHMS detection. The following abbreviations are used: Faraday isolator (FI), polarizing beam splitter (PBS), double pass acousto optic modulator (AOM), quarter wave plate (QWP), electro optic modulator (EOM), radio-frequency synthesizer (RF), voltage controlled oscillator (VCO), phase shifter (PS), and time-of-flight (TOF). Amplifiers are indicated with triangles.

to be large in size, and to couple to a high-throughput Roots pumping system through large-diameter tubing. However, for the initial testing of the instrument described here, we have designed a modular cold cathode discharge source for simplicity.

Our cold cathode source was made with a fused silica tube held by two electrodes, with an opening at the back for sample gas inlet, and another at the front through which ions are extracted. The electrodes are constructed using stock Ultra-Torr (Swagelok) unions. High temperature silicone O-rings are used to make seals to the fused silica tube which has ground-polished ends. The front electrode uses a custom modified ferrule with a 1 mm diameter aperture to allow ions to be extracted, and a 22° bevel to reduce beam expansion induced by space-charge interaction.[24,25] A small circle of stainless steel mesh was used in the back electrode to produce a more uniform electric field while still allowing gas to flow through the inlet. This source has proven to be robust, operating for typically 40 hrs before the front ferrule needs to be cleaned and the fused silica tube interchanged.

A schematic view of the source and its electrical connections is shown in Figure 2. An aluminum cap holds the back electrode to provide mechanical stability and allow for electrical and water-cooling connections. The ions are extracted through a 0.25" diameter hole in a grounded stainless steel plate after the front electrode.

The front electrode (cathode) is biased to 2–6 kV by the "float power supply," which determines the ion beam voltage. The rear electrode (anode) is biased to an additional 3.5 kV above the beam voltage by the "discharge power supply," the ground of which is floated to the beam voltage by the float power supply. The discharge supply is powered through an isolation transformer, and fully enclosed in a polycarbonate box for safety.

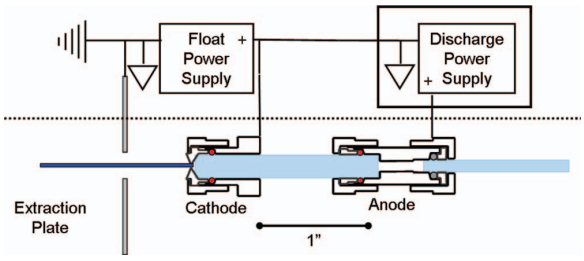

FIG. 2. A schematic of the cold cathode source and its electrical connections. Gas flows in from the right, and ions are extracted to the left. In this figure, the triangles indicate the "ground" connections of the power supplies; the polycarbonate isolation box for the discharge power supply is also indicated.

C. Ion optical system

The vacuum system, with the exception of the ion source chamber, is made from standard stainless steel Conflat components in order to achieve high vacuum conditions. The homebuilt ion source chamber, which is designed with a high-throughput expansion source in mind, is currently pumped by a 2000 L/s turbomolecular pump and has a pressure of $\sim 5 \times 10^{-6}$ Torr during operation.

The overlap and mass spectrometry regions are pumped by two 500 L/s turbomolecular pumps situated below the 90° deflector chambers, establishing typical pressures during operation of 6×10^{-7} Torr at deflector 1 and 8×10^{-8} Torr at deflector 2. The vacuum cross that houses the mass spectrometer detector is pumped by a 250 L/s turbomolecular pump, and has a typical pressure of $\sim 2 \times 10^{-8}$ Torr.

The ion optical configuration was designed to optimize the ion density in the laser/ion overlap region between the two electrostatic deflectors. All ion optical elements are electrostatic, so all particles with the same kinetic energy and charge state are guided on the same trajectory regardless of particle mass. The positive ions that emerge from the ion source with a voltage V_{beam} are initially focused by the first Einzel lens. In the next short vacuum nipple, the ion beam traverses a set of two parallel plate steerers. Each set of steerers can be used to deflect the ion beam both horizontally and vertically, allowing for an adjustment of the beam angle as well as for parallel offsets to the ion beam position. Each steerer plate is supplied by an independent bipolar power supply with voltages up to $\pm$ 1000 V. By applying voltages of the same sign to opposing steerer plates, it is also possible to induce additional horizontal or vertical focusing in the steerer section.

The cylindrical 90° deflectors follow a new design[23] that provides control of the ion beam focusing in both dimensions, unlike traditional cylindrical or quadrupole deflectors that create an astigmatic output beam. Our cylindrical deflectors use plates of differing heights to mimic the field of a spherical deflector at the ideal ion beam orbit without the cost and size of a true spherical deflector.

In operation, about 50% of the 10 μA ion beam current that is measured in the Faraday cup in the first ion deflector chamber can be transported through the overlap region and both deflectors and collected in the retractable Faraday cup after deflector 2. But once the 3 mm apertures are put into place in the drift region, only 1–2 μA of beam current make it through the system. After traversing the overlap region, the ion beam is turned by the second deflector, collimated by a second Einzel lens, and directed into the time-of-flight mass spectrometer.

D. Time-of-flight mass spectrometer

1. MS design

The Saykally ion beam instrument used a Wien velocity filter as a mass analyzer to identify the ions present in their beam and to optimize the current of the ion of interest. However, due to the relatively low mass resolution of the Wien filter, this optimization was performed at a lower beam energy than that at which spectroscopy was performed.[17–19]

In contrast, we have adopted a beam modulation[26,27] TOF-MS, which creates an ion packet from our continuous ion beam. This technique can perform mass and energy analysis at full beam energy, thereby avoiding the possibility that the ion beam composition may be dependent on the extraction voltage. Figure 1 shows the TOF-MS region, consisting of an Einzel lens and a pair of vertical electrostatic deflector plates. The deflection plates are held at an equal voltage but with opposite polarity. The polarity of the plates is then quickly reversed to sweep the ion beam over a 3.2 mm diameter aperture located near the detector. Two beam profilers aid in aligning the ion beam through the 1.53 m drift tube and onto the electron multiplier detector. At a beam voltage of 4 kV, our TOF-MS has a measured resolution of $m/\Delta m$ $\sim$400, which will be sufficient for optimizing the production of even large molecular ions such as $C_6H_7^+$.

2. MS results

The mass spectrometer is used to (1) identify the ion species in the plasma, (2) estimate the beam energy, and (3) calculate the energy spread of the ions created by the cold cathode plasma source. In a nitrogen plasma under typical conditions, the source produces mostly N_2^+ and N^+ in a ratio of $\sim$10:1, as shown in Figure 3. The field-free flight tube

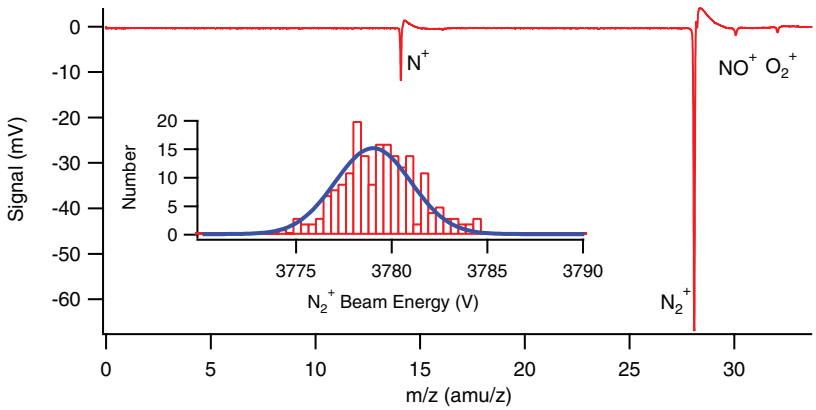

FIG. 3. Mass spectrum of an ion beam formed from a N_2 plasma, showing an N_2^+:N^+ ratio of $\sim$10:1. The inset shows the energy distribution of the N_2^+ ions.

length combined with arrival times of individual ions can be used to estimate both the average beam energy as well as the energy spread of the ions in the beam, as shown in Figure 3. For a beam voltage of ~3780 V, the energy spread was found to be 4.7 V (FWHM), which is consistent with the spectroscopic linewidths presented in Sec. III A.

E. Spectroscopy

1. Heterodyne detection

The Ti:Sapphire laser, optical cavity, locking scheme,[7,28] and the NICE-OHMS technique[29] have been described previously, so only a brief overview is given here. Two sets of RF sidebands are added by electro optic modulators (EOM). The first non-resonant EOM adds sidebands at ~30 MHz with a small modulation index. The signal from a back reflection off of the cavity is demodulated with an RF mixer to generate the Pound-Drever-Hall[30] error signal. An analog lockbox splits corrections from the error signal into slow and fast components. The slow corrections are sent to the cavity piezo to alter the cavity length, while the fast corrections are sent to the voltage controlled oscillator (VCO) that drives the acousto optic modulator (AOM) to make small changes in the laser frequency. As shown in Figure 1, the laser is double passed through an 85 MHz resonant AOM, which makes the pointing of the laser beam immune to changes in the AOM frequency[31] and induces a 170 MHz redshift to the laser light. The second EOM, resonant at 113 MHz, adds sidebands at exactly the free spectral range of the optical cavity with a modulation index $\beta \sim 0.83$. The laser is coupled into the cavity, and the light transmitted through the cavity is detected with a fast photodiode.

Heterodyne spectroscopy (including NICE-OHMS) is sensitive to both absorption and dispersion signals, which when unsaturated[32] are related to one another through the Kramers-Kronig relations. Since the two signals appear 90° out of phase with one another with respect to the RF modulation, it is possible to independently observe each signal with phase sensitive detection. To take advantage of this aspect of the spectroscopy, the AC component of the detector signal is amplified, split into two paths, and demodulated with two separate mixers which are set to be 90° out of phase with one another. The overall detection phase is adjusted using an RF phase shifter in the line between the RF generator and the amplifier that drives the 113 MHz EOM. The RF phase shifter is used to set one mixer to record solely the dispersion phase.

2. Modulation scheme and Doppler splittings

Because residual amplitude modulation induced by the EOM or external etalons can limit the sensitivity of NICE-OHMS, it is advantageous to use a second form of modulation.[34] In this work, the velocity of the ions is modulated by a square wave voltage at 4 kHz applied to the drift tube and aperture plates. After the heterodyne RF signal is demodulated with the mixers, the velocity modulation signal is demodulated using the lock-in amplifiers.

Because the laser propagates both parallel and antiparallel to the fast ion beam, each spectral line is both red (−) and blue (+) Doppler shifted away from the rest frequency (ν_0) to

$$\nu_\pm = \nu_0 \sqrt{\frac{1 \pm v/c}{1 \mp v/c}}, \tag{1}$$

where the velocity of the ions $v = \sqrt{2qV'/M}$, q is the charge of an electron, V' is the voltage of the ion beam in the drift tube, and M is the mass of the species. The voltage of the ion beam in the drift tube V' is determined from the modulation voltage (V_{mod}) by $V' = V_{beam} \pm V_{mod}$. (Note that the typical approximation $\nu_\pm \sim \nu_0(1 \pm v/c)$ is inaccurate by ~50 MHz at this frequency.) In a case where multiple ions are present, this Doppler splitting will provide mass identification of every spectral line.

For example, the red and blue components of a 1.985 kV ion beam of N_2^+ are separated by ~254 GHz (~8.47 cm^{-1}). With a 2 V_{pp} square wave driving the velocity modulation, the red and blue components are Doppler split again into components separated by 128 MHz. This splitting is not resolved, given the residual Doppler linewidth (observed to be 90 MHz for the ~2 kV beam) and the 113 MHz sideband spacing.

3. Frequency comb calibration

For ultra-high accuracy and precision on the frequency measurements, an erbium doped fiber amplifier frequency comb (MenloSystems FC1500/0060) is used to precisely calibrate the frequency of our Ti:Sapphire laser. For each point in our spectrum, the frequency of the Ti:Sapphire laser is determined by measuring the beat frequency between the Ti:Sapphire laser and the nearest comb mode.[28,29] In order to demonstrate the precision of the spectroscopic measurements, several frequency comb calibrated scans are shown in Sec. III A. The line center for the red Doppler shifted (ν_-) and the blue Doppler shifted (ν_+) components are measured by averaging scans of each component taken with both increasing and decreasing laser frequency, in order to compensate for apparent frequency shifts caused by the finite time constant of the lock-in amplifier. (Our scanning rate corresponds to only ~12 time constants from the minimum to the maximum of the dispersion profile, whereas a wait time of 10 time constants would be needed for the lock-in to reach 99% of its final value at the presently used 24 dB/octave roll-off.) As can be seen from Eq. (1), the rest frequency can then be determined as the geometric mean of the frequencies of the red- and blueshifted components, $\nu_0 = \sqrt{\nu_- \nu_+}$.

III. RESULTS

A. Spectroscopic results

Two typical scans of the $Q_{22}(14.5)$ line of the 1-0 band of the $A^2\Pi_u - X^2\Sigma_g^+$ Meinel system of N_2^+ are shown in Figure 4. Only the dispersion phase is displayed, because no signal was observed at the absorption detection phase due to optical saturation, as described below.

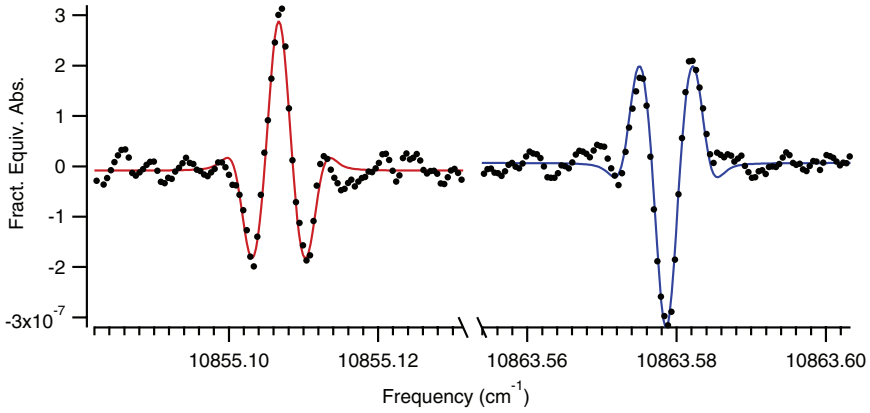

FIG. 4. Scans of red- and blue-shifted components of the $Q_{22}(14.5)$ line (black dots) collected at 1.985 kV beam voltage along with fits to Eq. (3) (solid curves). For clarity, only 1 in every 15 experimental points is shown. The Doppler shifted lines are 180° out of phase with one another, allowing for identification of the sign of a component's Doppler shift. The Doppler shifted components are separated by ~8.5 cm^{-1} as expected from Eq. (1). See the supplementary material[33] for more information about the vertical scale.

The line shape function for a dispersion signal for NICE-OHMS is given by[34]

$$\chi_{n-o}^{disp}(\nu_d) = \chi^{disp}(\nu_d - \nu_{fm}) - 2\chi^{disp}(\nu_d) + \chi^{disp}(\nu_d + \nu_{fm}), \quad (2)$$

where χ^{disp} is the general dispersion line shape function, ν_d is the de-tuning ($\nu_d = \nu - \nu_0$) of the carrier from the center frequency (ν_0) of the transition, and ν_{fm} is the RF modulation frequency (113 MHz).

The velocity modulation induces a second Doppler splitting (ν_{vm}) where the positive and negative splitting are 180° out of phase with one another. Therefore, the line shape for a dispersion signal for a NICE-OHMS velocity modulated ion beam signal is

$$\chi_{vm}^{disp}(\nu_d) = \chi_{n-o}^{disp}(\nu_d - \nu_{vm}) - \chi_{n-o}^{disp}(\nu_d + \nu_{vm}). \quad (3)$$

The Gaussian dispersion line shape, derived from a peak-normalized Gaussian line shape, is given by[32,35]

$$\chi^{disp}(\nu_d) = -\frac{2}{\sqrt{\pi}} e^{-\gamma^2} \int_0^{\gamma} e^{\gamma'^2} d\gamma', \quad (4)$$

where $\gamma = 2\nu_d\sqrt{\ln 2}/\Delta\nu$ and $\Delta\nu$ is the FWHM for the Gaussian profile.

When the spectra are fit to Eq. (3), the line center, FWHM, and peak-normalized Gaussian amplitude are obtained. An example of the red- and blue-shifted components of a NICE-OHMS signal are shown in Figure 4. The average linewidth for a 4 kV beam was ~120 MHz, which is consistent with the beam energy spread observed with the TOF-MS. Some slight asymmetry is seen between the amplitudes of the positive and negative velocity modulation components, and appears to be dependent on the alignment and overlap of the ion beam with the laser beam, which we have not yet fully optimized. We expect to have more useful diagnostic information regarding this asymmetry when we move to mid-infrared spectroscopy, as the narrower linewidth will enable a full resolution of the heterodyne and velocity modulation splittings.

Figure 5 shows an example of how spectra calibrated with the frequency comb are used to determine the line center. For each red- and blueshifted component of the NICE-OHMS signal, scans in opposite directions were collected, as described above. The average of the blue-shifted transitions was $\nu_+ = 10865.19163$ cm^{-1} and the average of the red-shifted transitions was found to be $\nu_- = 10\,853.49936$ cm^{-1}. The geometric mean of these two values gives a rest transition frequency of $\nu_0 = 10859.34392$ cm^{-1}, which is within 8 MHz of the rest frequency of 10859.34418 cm^{-1} measured with sub-Doppler resolution and frequency comb calibration in a positive column discharge.[29] This accuracy appears to be limited primarily by the asymmetry in the observed lineshapes (the optical frequency comb itself has an accuracy $\ll$1 MHz), and so we expect this to be further improved in the future.

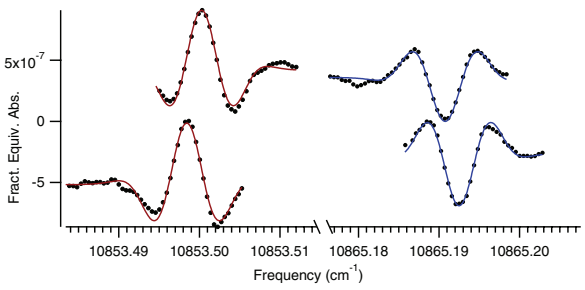

FIG. 5. Scans of red- and blue-shifted components of the $Q_{22}(14.5)$ line (black dots) collected at 3.781 kV beam voltage along with fits to Eq. (3) (solid curves) where the frequency axis is calibrated with the frequency comb. For clarity, only 1 in every 15 experimental points is shown. The top two traces are scanned toward the rest frequency and the bottom are scanned away from the rest frequency. As discussed in the text, the apparent frequency shifts are artifacts of the lock-in detection. The spectra have been offset vertically for clarity.

B. Sensitivity and saturation

For a baseline scan obtained with a 3 s lock-in time constant (and a 24 dB/octave roll-off, with a resulting detection bandwidth of 0.03 Hz), the observed noise equivalent absorption is $\sim 2 \times 10^{-11}$ cm^{-1} Hz$^{-1/2}$, which is a factor of 50 lower than the Saykally ion beam instrument.[17] The improvement comes from several factors: a lower fractional noise level at the detector (1.3×10^{-8} vs. 2×10^{-7}), thanks in part to heterodyne detection; a higher cavity finesse ($\mathcal{F}$, 450 vs. 100); and a longer laser/ion overlap length (L, 27 cm vs. 15 cm).

The shot noise limit for the instrument is given by[36]

$$\sigma_{\text{shot noise}} = \frac{\pi}{\mathcal{F} \times L}\sqrt{\frac{qB}{\eta P_0}}\frac{1}{J_0(\beta)J_1(\beta)}, \tag{5}$$

where q is the charge of an electron, B is the bandwidth of detection, η is the detector responsivity, P_0 is the power incident on the detector, and $J_n(\beta)$ are Bessel functions of the heterodyne modulation index, β. The effective path length through the ion beam is the laser/ion beam interaction length ($L = 27$ cm) times the number of round trip passes ($\mathcal{F}/\pi$). At a typical power level (incident on the detector) of 1.10 mW, the expected fractional shot noise is $\sim 2 \times 10^{-12}$ cm^{-1}. Thus, the observed noise in the instrument ($\sim 3 \times 10^{-12}$ cm^{-1}) is within a factor of $\sim$1.5 of the shot noise limit.

Absorption signals are not observable in this experiment due to the high degree of optical saturation, which is due to the high intracavity laser power and the lack of any relaxation process for the ions in the beam. For typical experimental conditions, we estimate the saturation parameter[32] of $G_0 \sim 30000$ for the carrier and $G_1 \sim 6300$ for the sidebands. The absorption signal should be reduced by a factor of $\sqrt{1 + G_1} \sim 80$, and is not detectable given our signal-to-noise ratio.

The impact of saturation on the dispersion signal in NICE-OHMS is strongly dependent on the ratio between the homogenous linewidth in the absence of saturation and the Doppler width (this ratio is denoted y in Ref. 32). Assuming the homogenous linewidth is set by the transit time (~ 1.6 μs for a 4 kV beam), and that the Doppler width is 120 MHz (from our fits), we expect $y \sim 0.0038$, and the dispersion signal should be reduced by only a factor of $\sim$2 at these saturation parameters.

However, the observed dispersion signals are a factor of $\sim$6 weaker than would be expected based on the ion number density, the transition strength, and the signal reduction from saturation, as described in the supplementary material.[33] At present, we can only speculate as to the reason for this discrepancy; possible reasons include: (1) not all N_2^+ ions may be in the vibronic ground state, (2) the actual Doppler-width may be narrower than the observed width if the latter has contributions from jitter in the beam energy caused by the power supplies, and (3) the overlap between the ion beam and the laser beam may be imperfect (as suggested by the asymmetries in the lines). We anticipate that future experiments in the mid-infrared will shed further light on this discrepancy.

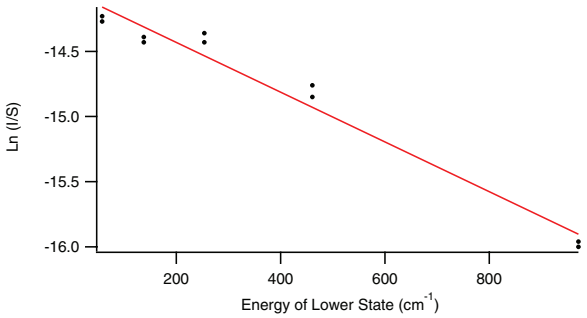

FIG. 6. Boltzmann diagram for observed N_2^+ transitions; for each transition, a separate measurement is shown for each of the red- and blue-shifted components to illustrate the reproducibility of the intensities. The calculated rotational temperature is 753 ± 45 K.

C. Discussion

In order to characterize the rotational distribution of the N_2^+ ions produced by our ion source, spectra of the ${}^qQ_{22}(J)$ lines (with $J = 4.5$, 7.5, 10.5, 14.5, and 21.5) with lower energies ranging from 60 to 970 cm^{-1} were collected. The spectra were fit to Eq. (3). The observed intensities (I) were normalized to the strength (S) of the transition, which was obtained along with the lower state energies from PGOPHER[37] using constants from Ref. 22. Figure 6 shows a Boltzmann diagram for the five observed transitions. From the slope of the linear regression fit, the rotational temperature is 753 ± 45 K.

While we only observed several transitions, this highly resolved technique could easily be applied to the observation of tens or hundreds of transitions. As the previous work[22] observed Doppler-limited transitions with linewidths of 1-1.4 GHz, the line centers were only determined to a precision around 60 MHz, with an accuracy of 150 MHz. With modest improvements to our current system, the accuracy of line center determination could be improved by at least a factor of 50 compared to the Doppler-limited measurements. This would greatly improve the overall RMS of the current effective Hamiltonian fit (RMS $\sim$100 MHz) and the individual observed–calculated values for many blended lines.

Finally, it should be noted that ion beam spectra enjoy a completely rigorous ion/neutral discrimination, both from the spatial separation of the ions from the neutrals and from the velocity modulation. While our previous cavity-enhanced velocity modulation technique studies[7,28,29] showed a discrimination between ions and neutrals in the lock-in detection phase, the ion beam technique is rigorously insensitive to absorbing or dispersing neutrals.

IV. CONCLUSIONS AND FUTURE DIRECTIONS

We have demonstrated the construction of a fast ion beam spectrometer which provides rigorous spatial and velocity modulation discrimination against neutral signals. We have demonstrated the instrument's capabilities by showing narrow ($\sim$120 MHz) spectral lines from the $A^2\Pi_u - X^2\Sigma_g^+$

system of N_2^+; this represents the first direct spectroscopy of an electronic transition in an ion beam. The ion beam instrument has a high-resolution mass spectrometer that provides online mass spectra at spectroscopically relevant beam energies. The dispersion line shape of the NICE-OHMS signal has been described, as well as the sensitivity and the observed noise. With the current detectors and laser power, the noise is close to the shot noise limit. The NICE-OHMS instrument reported in this article has been shown to be a factor of 50 more sensitive than the previous direct absorption ion beam instrument.[17] The rotational temperature of ions in the ion beam was found to be ~750 K.

The laser spectroscopy reported here was based on using two EOMs on a frequency tunable Ti:Sapphire laser. By combining the output of this Ti:Sapphire with a cw Nd:YAG laser in a periodically poled lithium niobate crystal, a mid-IR laser with appropriate sidebands can be generated. This will enable the extension of this NICE-OHMS ion beam spectroscopy technique into the mid-IR to record the fundamental vibrational bands of a wide variety of molecular ions in the 2.8–4.8 μm region.

Finally, it is expected that a continuous supersonic expansion discharge source[20] and skimmer will replace the cold cathode ion source in the near future. The use of a supersonic expansion will enable the spectroscopy of larger and more fluxional molecular ions (e.g., CH_5^+ and $C_3H_3^+$), for which quantum dilution at higher rotational temperatures has complicated previous attempts to apply velocity modulation spectroscopy.

ACKNOWLEDGMENTS

The design, construction, and commissioning of this ion beam spectrometer involved substantial contributions from a number of current and previous members of our group. In particular, we wish to thank Susanna Widicus Weaver, Matthew Zwier, Jeffrey Carter, and Kyle Ford. This work would not have been possible without the skilled craftsmanship of the School of Chemical Sciences Machine Shop and Electronics Shop. The authors also wish to acknowledge helpful conversations regarding ion beam spectrometer design with Jim Coe and Rich Saykally.

This work has been supported by a National Science Foundation (NSF) CAREER Award (CHE 04-49592), an Air Force Young Investigator Award (FA9550-07-1-0128), the National Aeronautics and Space Administration (NASA) Laboratory Astrophysics program (NNX08AN82G and NNG05GE59G), a David and Lucile Packard Fellowship, a Camille and Henry Dreyfus New Faculty Award, and the University of Illinois. M.W.P. has been supported by a Robert C. and Carolyn J. Springborn Fellowship from the University of Illinois.

[1] E. E. Ferguson and F. Arnold, Acc. Chem. Res. **14**, 327 (1981).
[2] E. Herbst and W. Klemperer, Astrophys. J. **185**, 505 (1973).
[3] T. Oka and M. F. Jagod, J. Chem. Soc., Faraday Trans. **89**, 2147 (1993).
[4] S. K. Stephenson and R. J. Saykally, Chem. Rev. **105**, 3220 (2005).
[5] C. S. Gudeman, M. H. Begemann, J. Pfaff, and R. J. Saykally, Phys. Rev. Lett. **50**, 727 (1983).
[6] M. F. Jagod, C. M. Gabrys, M. Rosslein, D. Uy, and T. Oka, Can. J. Phys. **72**, 1192 (1994).
[7] B. M. Siller, A. A. Mills, and B. J. McCall, Opt. Lett. **35**, 1266 (2010).
[8] S. Davis, M. Farnik, D. Uy, and D. J. Nesbitt, Chem. Phys. Lett. **344**, 23 (2001).
[9] D. T. Anderson, S. Davis, T. S. Zwier, and D. J. Nesbitt, Chem. Phys. Lett. **258**, 207 (1996).
[10] K. C. Thompson, D. L. Crittenden, and M. J. T. Jordan, J. Am. Chem. Soc. **127**, 4954 (2005).
[11] G. A. Olah, G. Klopman, and R. H. Schlosberg, J. Am. Chem. Soc. **91**, 3261 (1969).
[12] E. T. White, J. Tang, and T. Oka, Science **284**, 135 (1999).
[13] C. Savage, F. Dong, and D. J. Nesbitt, paper presented at 61st International Symposium on Molecular Spectroscopy, The Ohio State University, Columbus, OH, 2006.
[14] X. Huang, A. B. McCoy, J. M. Bowman, L. M. Johnson, C. Savage, F. Dong, and D. J. Nesbitt, Science **311**, 60 (2006).
[15] D. J. Nesbitt, paper presented at the 8th International Conference of Computational Methods in Sciences and Engineering, Kos, Greece, 3 October 2010.
[16] W. H. Wing, G. A. Ruff, W. E. Lamb, Jr., and J. J. Spezeski, Phys. Rev. Lett. **36**, 1488 (1976).
[17] J. V. Coe, J. C. Owrutsky, E. R. Keim, N. V. Agman, D. C. Hovde, and R. J. Saykally, J. Chem. Phys. **90**, 3893 (1989).
[18] J. C. Owrutsky, E. R. Keim, J. V. Coe, and R. J. Saykally, J. Phys. Chem. **93**, 5960 (1989).
[19] E. R. Keim, M. L. Polak, J. C. Owrutsky, J. V. Coe, and R. J. Saykally, J. Chem. Phys. **93**, 3111 (1990).
[20] K. N. Crabtree, C. A. Kauffman, and B. J. McCall, Rev. Sci. Instrum. **81**, 086103 (2010).
[21] J. Ye, L. S. Ma, and J. L. Hall, J. Opt. Soc. Am. B **15**, 6 (1998).
[22] D. W. Ferguson, K. N. Rao, P. A. Martin, and G. Guelachvili, J. Mol. Spectrosc. **153**, 599 (1992).
[23] H. Kreckel, H. Bruhns, K. A. Miller, E. Wahlin, A. Davis, S. Hockh, and D. W. Savin, Rev. Sci. Instrum. **81**, 063304 (2010).
[24] J. H. Moore, C. C. Davis, and M. A. Coplan, *Building Scientific Apparatus* (Perseus Books, Cambridge, MA, 2002), p. 371.
[25] J. R. Pierce, J. Appl. Phys. **11**, 548 (1940).
[26] J. M. B. Bakker, J. Phys. E **6**, 785 (1973).
[27] J. M. B. Bakker, J. Phys. E **7**, 364 (1974).
[28] A. A. Mills, B. M. Siller, B. J. McCall, Chem. Phys. Lett. **501**, 1 (2010).
[29] B. M. Siller, M. W. Porambo, A. A. Mills, and B. J. McCall, Opt. Express **19**, 24822 (2011).
[30] R. W. P. Drever, J. L. Hall, F. V. Kowalski, J. Hough, G. M. Ford, A. J. Munley, and H. Ward, Appl. Phys. B **31**, 97 (1983).
[31] E. A. Donley, T. P. Heavner, F. Levi, M. O. Tataw, and S. R. Jefferts, Rev. Sci. Instrum. **76**, 063112 (2005).
[32] W. Ma, A. Foltynowicz, and O. Axner, J. Opt. Soc. Am. B **25**, 1144 (2008).
[33] See supplementary material at http://dx.doi.org/10.1063/1.3665925 for details of the calculation of both observed and expected fractional equivalent absorption.
[34] A. Foltynowicz, F. M. Schmidt, W. Ma, and O. Axner, Appl. Phys. B **92**, 313 (2008).
[35] A. Foltynowicz, W. G. Ma, F. M. Schmidt, and O. Axner, J. Opt. Soc. Am. B **25**, 1156 (2008).
[36] J. Ye, "Ultrasensitive high resolution laser spectroscopy and its application to optical frequency standards," Ph.D. dissertation (University of Colorado Department of Physics, 1997).
[37] C. M. Western, PGOPHER, a program for simulating rotational structure, University of Bristol, 2009, see http://pgopher.chm.bris.ac.uk.

APPENDIX B

NOISE IMMUNE CAVITY ENHANCED OPTICAL HETERODYNE VELOCITY MODULATION SPECTROSCOPY

This Appendix contains a journal article reprinted with permission from Siller, Brian M.; Porambo, Michael W.; Mills, Andrew A.; and McCall, Benjamin J., *Opt. Exp.*, 19, 24822–24827, (2011).

Noise immune cavity enhanced optical heterodyne velocity modulation spectroscopy

Brian M. Siller,[1] Michael W. Porambo,[1] Andrew A. Mills[1] and Benjamin J. McCall[1,2,*]

[1]*Department of Chemistry, University of Illinois at Urbana-Champaign, Urbana, IL, 61801*
[2]*Departments of Astronomy and Physics, University of Illinois at Urbana-Champaign, Urbana, IL, 61801*
[*]*bjmccall@illinois.edu*

http://bjm.scs.illinois.edu/

Abstract: The novel technique of cavity enhanced velocity modulation spectroscopy has recently been demonstrated as the first general absorption technique that allows for sub-Doppler spectroscopy of molecular ions while retaining ion-neutral discrimination. The previous experimental setup has been further improved with the addition of heterodyne detection in a NICE-OHMS setup. This improves the sensitivity by a factor of 50 while retaining sub-Doppler resolution and ion-neutral discrimination. Calibration was done with an optical frequency comb, and line centers for several N_2^+ lines have been determined to within an accuracy of 300 kHz.

OCIS codes: (300.1030) Absorption; (300.6320) Spectroscopy, high-resolution; (300.6460) Spectroscopy, saturation; (300.6380) Spectroscopy, modulation; (300.6390) Spectroscopy, molecular; (300.6340) Spectroscopy, infrared.

References and links

1. S. K. Stephenson and R. J. Saykally, "Velocity modulation spectroscopy of ions," Chem. Rev. **105**, 3220–3234 (2005).
2. B. M. Siller, A. A. Mills, and B. J. McCall, "Cavity-enhanced velocity modulation spectroscopy," Opt. Lett. **35**, 1266–1268 (2010).
3. A. A. Mills, B. M. Siller, and B. J. McCall, "Precision cavity enhanced velocity modulation spectroscopy," Chem. Phys. Lett. **501**, 1 – 5 (2010).
4. J. Ye, L. S. Ma, and J. L. Hall, "Ultrasensitive detections in atomic and molecular physics: demonstration in molecular overtone spectroscopy," J. Opt. Soc. Am. B **15**, 6–15 (1998).
5. A. Foltynowicz, F. M. Schmidt, W. Ma, and O. Axner, "Noise-immune cavity-enhanced optical heterodyne molecular spectroscopy: Current status and future potential," Appl. Phys. B **92**, 313–326 (2008).
6. R. D. L. Kronig, "On the theory of dispersion of x-rays," J. Opt. Soc. Am. **12**, 547–556 (1926).
7. A. Foltynowicz, W. Ma, F. M. Schmidt, and O. Axner, "Wavelength-modulated noise-immune cavity-enhanced optical heterodyne molecular spectroscopy signal line shapes in the Doppler limit," J. Opt. Soc. Am. B **26**, 1384–1394 (2009).
8. E. A. Donley, T. P. Heavner, F. Levi, M. O. Tataw, and S. R. Jefferts, "Double-pass acousto-optic modulator system," Rev. Sci. Instrum. **76**, 063112 (2005).
9. R. W. P. Drever, J. L. Hall, F. V. Kowalski, J. Hough, G. M. Ford, A. J. Munley, and H. Ward, "Laser phase and frequency stabilization using an optical-resonator," Appl. Phys. B **31**, 97–105 (1983).
10. W. Ma, A. Foltynowicz, and O. Axner, "Theoretical description of doppler-broadened noise-immune cavity-enhanced optical heterodyne molecular spectroscopy under optically saturated conditions," J. Opt. Soc. Am. B **25**, 1144–1155 (2008).

#151471 - $15.00 USD Received 28 Jul 2011; revised 10 Oct 2011; accepted 17 Oct 2011; published 18 Nov 2011

11. M. S. Child, *Molecular Collision Theory* (Academic Press Inc, 1974).
12. R. G. DeVoe and R. G. Brewer, "Laser-frequency division and stabilization," Phys. Rev. A. **30**, 2827–2829 (1984).

1. Introduction

1.1. Velocity modulation spectroscopy

Laboratory spectroscopy of molecular ions is of great interest to a variety of fields, but is typically difficult because even in laboratory plasmas designed to observe a particular ion, the ion of interest has a very low concentration, typically orders of magnitude lower than that of any ambient neutral molecules in discharge cells. Velocity Modulation Spectroscopy (VMS) in positive column discharge cells has been the most commonly used technique in this field over the past few decades because it combines the advantages of relatively high ion density and ion-neutral discrimination [1].

Recently, a new method of performing VMS has been demonstrated by placing the plasma discharge cell within an optical cavity in a technique we call Cavity Enhanced Velocity Modulation Spectroscopy (CEVMS) [2, 3]. The optical cavity provides two major advantages over traditional VMS: greatly increased path length (about an order of magnitude greater than any previous VMS experiments, even with a cavity finesse of only 300) and the ability to observe a sub-Doppler Lamb dip for each spectral line (due to the high intracavity laser power and the perfectly overlapped counterpropagating beams induced by the optical cavity).

Although CEVMS showed much promise, its sensitivity was ultimately limited by noise in the laser-cavity lock, particularly noise that was induced by the high voltage AC plasma discharge. In the current work, the sensitivity limitations of CEVMS have been greatly improved by combining the technique with Noise Immune Cavity Enhanced Optical Heterodyne Molecular Spectroscopy (NICE-OHMS).

1.2. NICE-OHMS

NICE-OHMS is a technique that was first developed in the late 1990s [4], and has since been used with great success by several groups to observe spectra of many different neutral molecules with sensitivity unprecedented by other direct absorption spectroscopic techniques [5].

The principle of NICE-OHMS is that while the laser carrier frequency is locked to an optical cavity mode, a set of FM sidebands are added to the laser, spaced at an integer multiple of the cavity free spectral range (FSR). Thus the carrier (laser center frequency) and both sidebands get coupled into, and out of, the cavity simultaneously. The transmitted beam is detected with a fast photodiode and demodulated at the heterodyne modulation frequency.

Because the two sidebands have the same intensity when no absorbers are present within the cavity and are 180° out of phase with one another, the positive and negative RF beat signals created by the sideband frequencies beating against the carrier frequency cancel each other out, causing NICE-OHMS to be a zero-background technique. When the frequency modulated laser is coupled through the optical cavity and the sideband spacing is set to be exactly equal to the cavity FSR, any noise in the laser-cavity lock is the same for the carrier and both sidebands, so the demodulated signal is unaffected. Thus, NICE-OHMS allows for the path length enhancement of an optical cavity, a factor of $(2 \cdot Finesse/\pi)$, while not introducing any additional noise in the system beyond that of ordinary single-pass heterodyne spectroscopy.

An absorption signal is observed when one of the RF sidebands is absorbed more than the other, causing an imbalance in the two heterodyne beats, so they no longer add to zero. For any absorption, there is a corresponding dispersion, related by the Kramers-Kronig relations [6]. With heterodyne detection, it is possible to observe this dispersion signal, because a phase shift

#151471 - $15.00 USD Received 28 Jul 2011; revised 10 Oct 2011; accepted 17 Oct 2011; published 18 Nov 2011

in the carrier frequency or either of the sideband frequencies also creates an imbalance in the beat signals, leading to a net signal. The net signal obtained from a phase shift of one of the laser frequencies is 90° out of phase with that obtained from absorption of one of the sidebands, so through phase-sensitive detection, it is possible to observe absorption and dispersion independently of one another.

2. Experimental

The experimental setup is shown in Fig. 1. It is similar to that previously used for cavity-enhanced velocity modulation experiments [2, 3], with the addition of a second electro optic modulator (EOM) and a high speed photodiode for heterodyne detection.

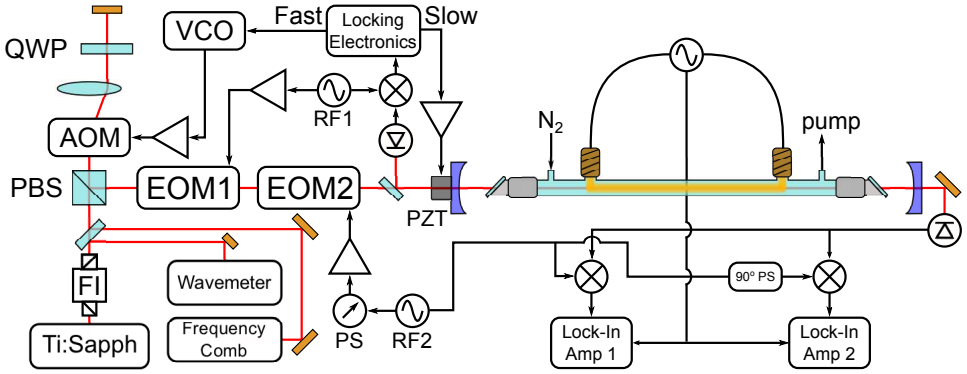

Fig. 1. Experimental Layout. FI: Faraday isolator; PBS: polarizing beamsplitter; AOM: acousto optic modulator; QWP: quarter wave plate; VCO: voltage controlled oscillator; EOM: electro optic modulator; PZT: piezo electric transducer; RF: radio frequency generator; PS: phase shifter.

The laser is double-passed through an acousto optic modulator that is resonant at 85 MHz, which red-shifts the laser frequency by 170 MHz and makes the pointing of the beam immune to changes in the acousto optic modulator (AOM) drive frequency [8].

The laser is then passed through two electro optic modulators, which add two sets of RF sidebands to the laser frequency. The first EOM, which is non-resonant, adds 30 MHz sidebands with a small modulation index ($\beta \sim 0.01$). These sidebands are detected in the back-reflected signal off of the cavity, and are demodulated with an RF mixer to generate a Pound-Drever-Hall [9] error signal. That error signal is then processed with analog electronics, and split off into two components; slow corrections (up to 100 Hz) are sent to the cavity piezo, while faster corrections (up to 60 kHz) are sent to the voltage controlled oscillator (VCO) that drives the acousto optic modulator AOM.

The second EOM, which is resonant, adds sidebands spaced at an integer multiple of the FSR of the optical cavity. The light transmitted through the cavity is detected with a fast photodiode. The AC portion of the detector signal is sent through an RF amplifier, then a power splitter that sends the signal to two mixers. The mixers are referenced to the sideband RF signal, but are set to be 90° out of phase with one another through a phase delay induced by a difference in cable lengths between the reference signal and the local oscillator (LO) input of the mixers. The overall detection phase is adjusted using an RF phase shifter in the line between the RF generator and the amplifier that drives the heterodyne EOM.

Two different experimental setups were used to observe several lines in the $v = 1 \leftarrow 0$ band of the Meinel system ($A^2\Pi_u - X^2\Sigma_g^+$) of N_2^+. One setup used a 1 GHz resonant EOM to space the

#151471 - $15.00 USD Received 28 Jul 2011; revised 10 Oct 2011; accepted 17 Oct 2011; published 18 Nov 2011

heterodyne sidebands at 9 cavity FSRs for observation of Doppler profiles and demonstration of ion-neutral discrimination. The other setup used a 113 MHz resonant EOM to space the sidebands at 1 cavity FSR for sub-Doppler studies of the observed Lamb dips.

The optical cavity used in both setups had a finesse of 300, which gave a cavity linewidth of 450 kHz. Throughout the course of a scan, the cavity length would change by 12 μm as the piezo was scanned, causing the FSR to change by approximately 1 kHz. To avoid increased noise near the end of the piezo travel, a feed-forward loop was implemented, in which the piezo voltage was scaled down, inverted, and sent to the DC FM input of the RF driver so the sideband spacing would track with the cavity FSR as the cavity length was scanned.

3. Results & discussion

3.1. Sub-Doppler lineshape analysis

Each laser frequency present in the cavity can act as a pump and/or a probe for sub-Doppler spectroscopy. For example, the carrier can act as a pump while a sideband acts as a probe, producing a Lamb dip spaced halfway between the two frequencies. Thus, Lamb dips are observed spaced at half the sideband spacing. For significant modulation depth ($\beta \sim 1$), where maximum heterodyne signal intensity is obtained, second-order sidebands also add small contributions to the outer edges of the signals. The overall sub-Doppler lineshape function is given by

$$\begin{aligned}\chi(\nu_d) = \{&A_1[\chi_a(\nu_d - \frac{\nu_{fm}}{2}) - \chi_a(\nu_d + \frac{\nu_{fm}}{2})] + A_2[\chi_a(\nu_d - \nu_{fm}) - \chi_a(\nu_d + \nu_{fm})] \\ &+ A_3[\chi_a(\nu_d - \frac{3\nu_{fm}}{2}) - \chi_a(\nu_d + \frac{3\nu_{fm}}{2})]\} \sin\theta_{fm} \\ &+ \{A_0[\chi_d(\nu_d)] + A_1[\chi_d(\nu_d - \frac{\nu_{fm}}{2}) + \chi_d(\nu_d + \frac{\nu_{fm}}{2})] \\ &+ A_2[\chi_d(\nu_d - \nu_{fm}) + \chi_d(\nu_d + \nu_{fm})]\} + A_3[\chi_d(\nu_d - \frac{3\nu_{fm}}{2}) + \chi_d(\nu_d + \frac{3\nu_{fm}}{2})]\} \cos\theta_{fm}\end{aligned} \tag{1}$$

where $\nu_d = \nu - \nu_0$ is the detuning of the laser center frequency, ν, from the transition center frequency, ν_0. ν_{fm} is the heterodyne modulation frequency and θ_{fm} is the heterodyne detection phase. $A_{0,1,2,3}$ are amplitudes related to the overall laser power and the modulation depth. In this work, these amplitudes are used as fit parameters with the constraint $A_i > A_{i+1}$.

χ_a and χ_d are general lineshape functions for absorption and dispersion profiles, respectively. In this work, the Lamb dips appear to be Gaussian, so χ_a is the general peak-normalized Gaussian lineshape, while χ_d is derived from χ_a transformed by the Kramers-Kronig relations [6]. The lineshape functions are given by [7]

$$\chi_a(\nu) = e^{-4\gamma^2} \qquad \text{and} \qquad \chi_d(\nu) = \frac{2}{\sqrt{\pi}} e^{-\gamma^2} \int_0^\gamma e^{\gamma'^2} d\gamma' \tag{2}$$

where w is the Gaussian full width at half maximum (FWHM), ν_0 is the line center, and $\gamma = 2(\ln 2)^{1/2}(\nu - \nu_0)/w$.

The combination of concentration and velocity modulation of N_2^+ causes the observed Doppler profile to be much different from those seen in other NICE-OHMS setups that observe neutral molecules. In this work, no attempt was made at fitting the overall Doppler broadened lineshapes; the Doppler broadened profile was approximated by a third order polynomial near the line center that was used as a baseline for sub-Doppler fitting.

3.2. 1 GHz sideband spacing

The 1 GHz system, with sidebands spaced at 9 FSRs, was used for Doppler-broadened scans. Figure 2 shows a typical scan with this system, collected with a 300 ms lock-in time constant,

#151471 - $15.00 USD Received 28 Jul 2011; revised 10 Oct 2011; accepted 17 Oct 2011; published 18 Nov 2011

100 ms delay between points, and approximately 10 MHz step size. With this setup, only a single mixer and lock-in amplifier were used, and the RF phase was set to be nearly pure dispersion, as evidenced by the presence of a strong central Lamb dip, which is expected to be absent from the pure absorption signal.

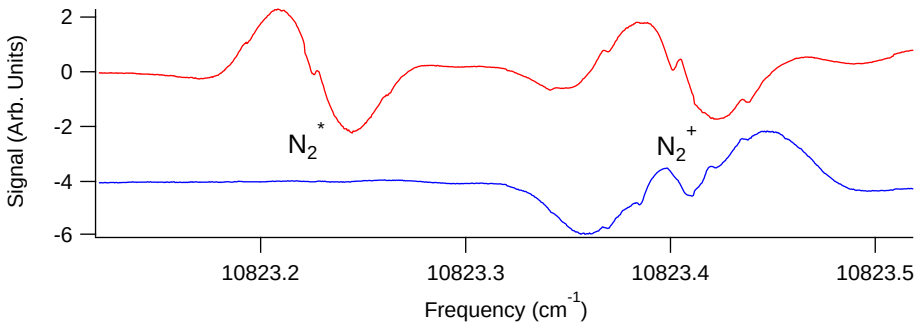

Fig. 2. A scan with 1 GHz sideband spacing, demonstrating discrimination between N_2^+ and N_2^*. At the left is an unassigned transition of electronically excited neutral N_2. At the right is an unresolved blend of two N_2^+ lines, $Q_{12}(6)$ and $Q_{11}(14)$. The top and bottom traces are the X and Y channels of the lock-in amplifier, rotated in post-processing by 64°.

During data collection, the lock-in amplifier phase was set to zero. After collection of the data, computer software was used to rotate the phase of the signal with respect to the plasma frequency in order to minimize the amount of N_2^* signal present in the Y channel. Note that just the concentration of N_2^* is modulated in the plasma, so its Doppler-broadened profile is similar to other NICE-OHMS lineshapes that are typically observed for neutral molecules [10]. With N_2^+, however, both the velocity and concentration are being modulated simultaneously, which leads to a more complex lineshape that cannot be isolated into a single phase.

3.3. 113 MHz sideband spacing

For spectroscopy with sidebands spaced at a single cavity FSR, both RF mixers were used, and the lengths of cables going to the LO inputs of the two mixers were made such that the relative phases were 90° apart. The overall phase of the system was adjusted to optimize the isolation of absorption and dispersion signals using an electronic phase shifter on the input to the amplifier that drives EOM2.

A typical scan with the 113 MHz system, calibrated with an optical frequency comb, as described in [3], is shown in Fig. 3. A single scan produces four orthogonal signals: absorption and dispersion, each with X and Y components. Absorption and dispersion signals are first separated using the 90° phase difference in the RF mixer references, then each of these is split into two components separated by 90° relative to the plasma frequency by mixers within the lock-in amplifiers. Fits were performed on the Lamb dips of the comb-calibrated scans using Eq. (1), along with a cubic sloped baseline to approximate the Doppler profile near the line center. Note that the residuals show that the actual lineshape is more complex than that given in Eq. (1) due to the combination of concentration modulation and velocity modulation occurring in the plasma. A more thorough lineshape analysis will be the subject of future studies.

Based on fits of several scans in alternating directions, calibrated with an optical frequency comb, the measured line center frequency was found to have a standard deviation of approximately 2 MHz. Because of the delayed response of the lock-in amplifiers used for demodulation, the determined line centers tend to be shifted in the direction of the scanning. By pairing

#151471 - $15.00 USD Received 28 Jul 2011; revised 10 Oct 2011; accepted 17 Oct 2011; published 18 Nov 2011

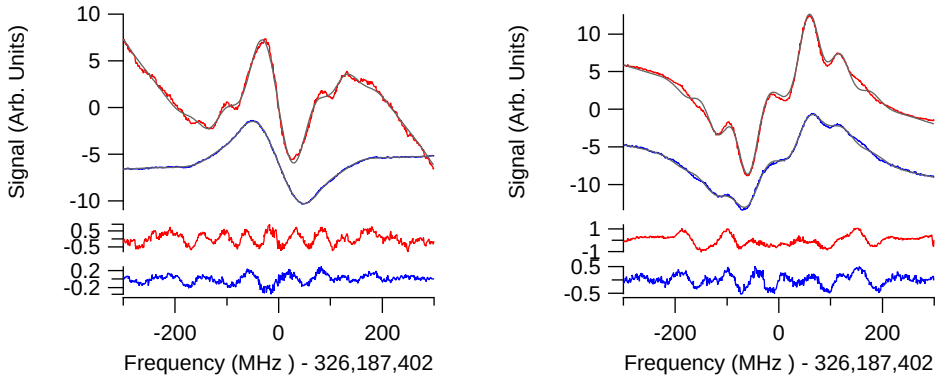

Fig. 3. Dispersion (left) and absorption (right) Lamb dips of the $Q_{22}(13)$ line of N_2^+ observed in the 113 MHz configuration, calibrated with an optical frequency comb. Top, red: Y channel outputs of lock-ins. Bottom, blue: X channel outputs of lock-ins, offset vertically for clarity. Residuals are shown at the bottom.

and averaging pairs of scans in opposite directions, the measurement standard deviation can be reduced to ∼300 kHz. It was found that the line center frequencies determined previously in Ref [3] were all too high by 20 MHz due to an ambiguity in the determination of the sign of the comb carrier-envelope offset.

The pressure broadening of ∼8 MHz/Torr of the observed Lamb dips observed in Ref [3] and in the current work is consistent with the expected broadening given by the total collision cross section given by Eq. (5.69) of Ref [11] integrated over the Maxwell-Boltzmann distribution for the estimated plasma temperature (∼600 K), but the extrapolated ∼32 MHz linewidth at zero pressure is still not fully understood.

4. Conclusions & future work

The technique of cavity enhanced velocity modulation spectroscopy has been further improved by the addition of heterodyne detection to minimize the noise induced by the laser-cavity lock. This modification has improved upon the achievable sensitivity of CEVMS by nearly two orders of magnitude while retaining ion-neutral discrimination. Combined with an optical frequency comb, line centers can be determined to within 300 kHz.

Further improvement to this technique can be realized by moving to a higher finesse cavity to increase both the effective path length and the intracavity optical power. Moving to a higher finesse cavity would cause this technique to be more sensitive to mismatches in the cavity FSR and RF sideband frequency due to the narrower cavity resonances. This effect could be compensated for by actively locking the RF sideband frequency to the cavity FSR using the DeVoe-Brewer [12] method, rather than the less precise feed-forward loop that was used in this work. This technique could also be extended to mid-infrared wavelengths by using a high power optical parametric oscillator (OPO) to observe a much greater variety of molecular ions.

Acknowledgments

This work has been supported by an NSF CAREER award (CHE 04-49592), an Air Force Young Investigator award (FA9550-07-1-0128), the NASA Laboratory Astrophysics program (NNX08AN82G), a David and Lucile Packard Fellowship, and the University of Illinois. Michael Porambo has been supported by a Robert C. and Carolyn J. Springborn Fellowship.

#151471 - $15.00 USD Received 28 Jul 2011; revised 10 Oct 2011; accepted 17 Oct 2011; published 18 Nov 2011

APPENDIX C

REFRACTIVE INDEX MEASUREMENTS OF SOLID PARAHYDROGEN

This Appendix contains a journal article reprinted with permission from Perera, Manori; Tom, Brian A.; Miyamoto, Yuki; Porambo, Michael W.; Moore, Lauren E.; Evans, William R.; Momose, Takamasa; and McCall, Benjamin J., *Opt. Lett.*, 36, 840–842, (2011).

Refractive index measurements of solid parahydrogen

Manori Perera,[1,9] Brian A. Tom,[1,2] Yuki Miyamoto,[3,4] Michael W. Porambo,[1] Lauren E. Moore,[1,5] William R. Evans,[6] Takamasa Momose,[3,7] and Benjamin J. McCall[1,6,8,10]

[1]*Department of Chemistry, University of Illinois at Urbana–Champaign, 600 South Mathews Avenue, Urbana, Illinois 61801, USA*

[2]*Currently with the Department of Chemistry, United States Air Force Academy, Colorado 80840, USA*

[3]*Department of Chemistry, Kyoto University, Kyoto 606-8502, Japan*

[4]*Currently with Graduate School of Natural Science and Technology, Okayama University, 3-1-1, Tsushima-Naka, Okayama 700-8530, Japan*

[5]*Currently with Celanese Corporation, 9502 Bayport Boulevard, Pasadena, Texas 77507, USA*

[6]*Department of Physics, University of Illinois at Urbana–Champaign, 1110 West Green Street, Urbana, Illinois 61801, USA*

[7]*Currently with Department of Chemistry, University of British Columbia, 2036 Main Mall, Vancouver, British Columbia V6T 1Z1, Canada*

[8]*Department of Astronomy, University of Illinois at Urbana-Champaign, 1002 West Green Street, Urbana, Illinois 61801, USA*

[9]*e-mail: mperera@illinois.edu*

[10]*e-mail: bjmccall@illinois.edu*

Received December 22, 2010; accepted January 31, 2011;
posted February 11, 2011 (Doc. ID 140160); published March 9, 2011

Solid para-H_2 is a promising gain medium for stimulated Raman scattering, due to its high number density and narrow Raman linewidth. In preparation for the design of a cw solid hydrogen Raman laser, we have made the first measurements, to our knowledge, of the index of refraction of a solid para-H_2 crystal, in the wavelength range of 430–1100 nm. For a crystal stabilized at 4.4 K, this refractive index is measured to be $n_{p\text{-}H_2} = 1.130 \pm 0.001$ at 514 nm. A slight, but significant, dependence on the final crystal-growth temperature is observed, with higher $n_{p\text{-}H_2}$ at higher crystal-growth temperatures. Once a crystal is grown, it can be heated up to 10 K with no change in $n_{p\text{-}H_2}$. The refractive index varies only slightly over the observed wavelength range, and no significant birefringence was observed.

OCIS codes: 290.3030, 120.4530, 260.1180, 160.4760, 290.5910.

Molecular hydrogen has long been considered a particularly useful gain medium for stimulated Raman scattering, because of its large vibrational frequency. As early as 1986, sequential Stokes conversion in a multipass cell of gaseous H_2 was used to convert a pulsed dye laser into a continuously tunable laser in the 1–12 μm region [1]. Similar setups have been used successfully by many groups, but they depend on multipass mirrors with both high damage thresholds and high reflectivity over a wide wavelength range, which are difficult to obtain.

Solid para-H_2 has recently been demonstrated to be a suitable medium for Raman shifting pulsed lasers, without the need for specialized optics. Because of its higher density ($n \sim 2.6 \times 10^{22}$ cm^{-3}) and smaller Raman linewidth ($\Gamma \sim 7$ MHz [2]), solid H_2 would be expected to have a much higher Raman gain than gaseous H_2. Indeed, measurements by Katsuragawa and Hakuta [3] have shown that the solid's Raman gain coefficient is 7000 times higher than that of the gas. In the last decade, solid H_2 Raman pulsed lasers have been demonstrated [3–5] and are now in routine use in spectroscopic applications [6,7].

However, the high resolution spectroscopic study of molecular vibrations requires cw lasers with narrower bandwidth than can be obtained by transform-limited pulsed lasers. Carlsten *et al.* [8] have demonstrated a cw Raman laser in gaseous H_2, using a high-finesse cavity to produce sufficient intracavity power to drive the stimulated Raman scattering. Their lasers have achieved wide tunability [9] and high conversion efficiency [10], but are technically complicated due to the need for a high-finesse cavity. To our knowledge, these lasers have not been used by other groups.

Our long-term goal is to develop a cw Raman laser based on solid para-H_2. The high Raman gain of the solid should permit such a laser to have a considerably lower finesse cavity than the gaseous H_2 lasers, thereby making them easier to align and maintain. The high gain of the solid may also facilitate the extension of the cw Raman H_2 laser to longer wavelengths, where the stimulated Raman scattering process is less efficient.

To design such a laser, it is essential to minimize Fresnel losses at interfaces inside the laser cavity, in particular between the solid H_2 gain medium and the cell windows (typically sapphire) that contain the H_2 crystal. The angles of these interfaces can be chosen to be at or near Brewster's angle for minimal reflective losses, but this requires knowledge of the refractive index of solid para-H_2; to our knowledge, this quantity (which we refer to as $n_{p\text{-}H_2}$) has not been previously measured. In this Letter, we describe the procedure used independently in our labs in Illinois and Kyoto to generate a uniform para-H_2 crystal and to measure $n_{p\text{-}H_2}$. The dependence of $n_{p\text{-}H_2}$ on wavelength and the polarization angle of light, as well as the temperature of the crystal, is also discussed.

Solid para-H_2 crystals were grown in a cell (illustrated in Fig. 1) consisting of a 1.27 cm hole bored in a 5.1 cm stainless steel body. One end of the cell was machined at an angle ($\phi = 10.0°$ in Illinois; $\phi = 20.2°$ in Kyoto) to induce a deflection in a laser beam propagating through the crystal; the measurement of this deflection enabled the measurement of $n_{p\text{-}H_2}$. The ends of the cell were sealed with sapphire windows using indium gaskets. The cell was mounted to an oxygen-free high-conductivity (OFHC) copper plate machined with a small pin that

0146-9592/11/060840-03$15.00/0

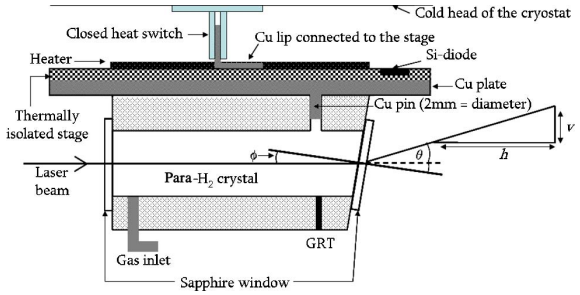

Fig. 1. (Color online) Schematic of the cell and the laser path in the presence of the para-H_2 crystal.

protrudes into the cell body (sealed with an indium gasket), to serve as a nucleation point for crystal growth. The OFHC plate in turn was mounted to the thermally isolated stage of a liquid-helium-cooled cryostat.

The temperature of the cell was controlled by adjusting the thermal contact with the cold head by opening a heat switch, and/or by using a resistive heater on the cell. The temperature gradient within the cell was monitored using a germanium resistance thermometer (GRT) mounted on the bottom of the cell and a silicon diode mounted on the thermally isolated stage where the cell rests. The temperature difference between the two sensors was typically less than 1 K, and because the thermal conductivity of solid para-H_2 (1.5 W cm^{-1} K^{-1} at 4 K [11]) is so much higher than that of stainless steel (0.003 W cm^{-1} K^{-1} [12]), the H_2 crystal would be expected to be at a temperature very close to that of the silicon diode. The cell was filled through narrow stainless steel tubing, which passed along the radiation shield of the cryostat before connecting to the cell body.

The crystal was grown with 99.98% pure para-H_2 [13] following the pressurized crystal-growth method [14], which is known to yield a transparent single crystal. Para-H_2 gas was condensed into the cell at 15–20 K, while the liquid level was watched. Once the cell was filled, the cryostat's gas line was connected to a small (150 mL) tank and the cell was heated to 30–45 K to boil off the liquid and pressurize the tank. Fresh para-H_2 gas was then condensed into the cell, and, finally, pressurized gas from the small tank (~200 psi in Illinois, ~290 psi in Kyoto) was applied to the condensed para-H_2 liquid. The temperature was slowly lowered to the final temperature over a 1 h period as the crystal grew. The crystallization was initiated from the coldest point (the copper pin at the top of the cell) and the crystal growth was observed as the liquid–solid boundary (crystallizing surface) slowly moved downward. The same procedure was repeated to create crystals with higher final growth temperatures, which required lower backing pressures [15].

Hydrogen's ability to yield such a large single crystal stems from the fact that solid para-H_2 is a quantum crystal, with a "self-annealing" property, similar to solid helium [16]. We observed a similar liquid–solid boundary during crystal growth as in previous studies ([14], Fig. 2), and our observation of a single crystallizing surface is strong evidence that a single crystal was in fact formed. In other trial runs (with different crystal-growth procedures, inadequate backing pressure, or impurities in the sample), a single crystallizing surface was not observed: the resulting samples were not completely transparent; laser beams sent through those samples suffered complex scattering patterns, and cracks would result as the temperature dropped, separating individual crystals. With proper care in the crystal-growth process, however, a transparent single crystal always resulted. Previous work has established that high purity para-H_2 crystallizes to form a hexagonal close-packed lattice at low temperature and high pressure [15] and that the c axis follows the largest thermal gradient [4,17]; in the present case this is the vertical axis.

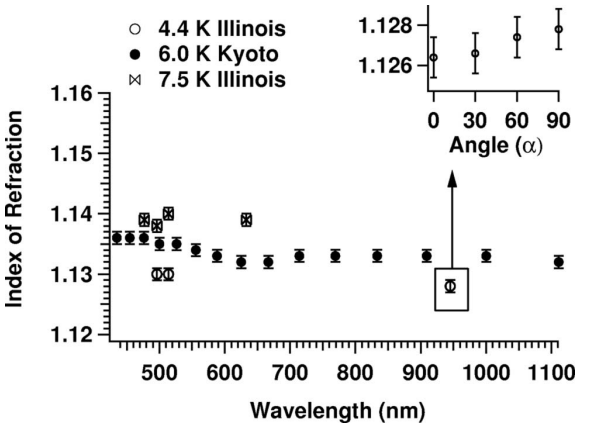

Fig. 2. Index of refraction data taken at various growth temperatures of the crystal. The inset shows the dependence on α, the angle (in degrees) between the polarization axis of the light and the c axis of the crystal.

The optical setup used for measurements of $n_{p\text{-}H_2}$ in Illinois consisted of three lasers: an argon ion laser with 476, 496, and 514 nm emission; a He–Ne laser with 632 nm emission; and a tunable diode laser at 945 nm. After the crystal was fully grown, the laser light was passed through the crystal. The angle of the deflected beam (θ) was determined by measuring its distance (labeled v) from the horizontal at two positions separated by 1.5 m (labeled h), as shown in Fig. 1. The beam position was determined by monitoring the voltage of a photodiode as it was translated vertically. The measured beam positions are accurate to within ± 0.013 cm, the precision of the micrometer mount used. In Kyoto, a master oscillator power oscillator laser was used to measure $n_{p\text{-}H_2}$ at 15 different wavelengths between 430 nm and 1100 nm. In that measurement, the deflected angle (θ) was measured by locating the laser spot (visually) on a screen 6.5 m from the cryostat.

Snell's law, $n_{p\text{-}H_2} \sin(\phi) = n_{\text{vac}} \sin(\theta + \phi)$, was used to infer $n_{p\text{-}H_2}$. Here, ϕ includes both the tilt of the cryostat stage with respect to the incident laser beam as well as the angle of the intentionally tilted window. The dependence of $n_{p\text{-}H_2}$ on the polarization angle of the incident laser was measured by inserting a half-wave plate in the laser path prior to the cryostat and changing its angle in increments of 15°. The results are presented in Fig. 2.

The measurements show only a slight dependence of $n_{p\text{-}H_2}$ on wavelength. The 6.0 K data, which have the largest wavelength coverage, show that $n_{p\text{-}H_2}$ decreases slightly with increasing wavelength up to ~650 nm and then levels off, becoming consistent with a constant

value of 1.132±0.001. The 4.4 K and 7.5 K data sets are each consistent with a constant $n_{p\text{-}H_2}$, but these data have sparser wavelength coverage. The constancy of $n_{p\text{-}H_2}$ with wavelength is expected, since para-H_2 has no absorptions between the far-IR and the UV.

The inset of Fig. 2 shows how $n_{p\text{-}H_2}$ varies with the polarization angle, α, of the incoming laser beam (at 945 nm and 4.4 K). Although there is a hint of an increase of $n_{p\text{-}H_2}$ with α, the trend is not statistically significant, given our measurement uncertainties; we adopt an upper limit of 0.002 for the magnitude of birefrigence.

The data indicate that $n_{p\text{-}H_2}$ increases with the final temperature of crystal growth. This is surprising, as the density of solid para-H_2 is known [14,15] to decrease slightly with increasing temperature in this range. One might therefore anticipate that $n_{p\text{-}H_2}$ would decrease with decreasing density (as the temperature increases), but our observations show that $n_{p\text{-}H_2}$ instead increases.

To test the sensitivity of $n_{p\text{-}H_2}$ to the rate of crystal growth, we grew a crystal at a faster rate, lowering the temperature to 4.4 K in only 10 min, rather than 1 h. This crystal had a slightly higher $n_{p\text{-}H_2}$ (at 514 nm) of 1.134 ± 0.001, compared with 1.130 ± 0.001 for the slowly grown crystal. One might expect the slowly grown crystal to attain a higher density than the quickly grown crystal, as the former has more time to rearrange its lattice. These observations are consistent with the other measurements, in the sense that in both cases $n_{p\text{-}H_2}$ increases with decreasing density (due to either higher growth temperature or faster growth rate).

After crystal growth is complete, raising the temperature does not change $n_{p\text{-}H_2}$. For a crystal stabilized at a final growth temperature of 4.4 K, we gradually increased the temperature up to 10 K (in increments of ~0.5 K) and observed no change in the deflection of the laser. Once the crystal is completely grown, the lattice cannot expand because it is completely confined in the cell, and the constant density leads to a constant $n_{p\text{-}H_2}$.

The observed temperature dependence of $n_{p\text{-}H_2}$ is significantly larger than can be accounted for by the measurement uncertainties. For example, in order for the measured $n_{p\text{-}H_2}$ of the 4.4 K crystal to fall within the uncertainties of the data at 6.0 K, the measured deflection angle would have to have been mismeasured by 0.14°, which corresponds to an error in the vertical beam deflection (v) of 0.23 cm, or 18 times our precision. We therefore conclude that the surprising inverse dependence of $n_{p\text{-}H_2}$ on density is not due to systematic errors in the measurements, but we cannot offer a physical explanation of the effect at this time.

In summary, we have measured the refractive index of solid para-H_2 for the first time, to our knowledge. Measurements were performed for final crystal-growth temperatures of 4.4, 6.0, and 7.5 K, over a wavelength range of 430–1100 nm. The refractive index (at 514 nm) is $n_{p\text{-}H_2} = 1.130 \pm 0.001$ for a crystal stabilized at 4.4 K and increases to 1.140 ± 0.001 at 7.5 K. Our measurements suggest that $n_{p\text{-}H_2}$ is dependent on the density of the crystal, with higher values at lower densities. A small dependence of $n_{p\text{-}H_2}$ on wavelength was observed, but no significant dependence on polarization was seen. These measurements can be expected to facilitate the development of a cw Raman laser using solid para-H_2 as the gain medium, which may ultimately lead to a new widely tunable and narrow linewidth laser source in the mid-IR region.

The authors wish to thank Siddhartha Bhasker for his assistance with the early stages of the experimental development in Illinois. The work in Illinois has been supported by the David and Lucile Packard Foundation and by the University of Illinois.

References

1. P. Rabinowitz, B. N. Perry, and N. Levinos, IEEE J. Quantum Electron. **22**, 797 (1986).
2. T. Momose, D. P. Weliky, and T. Oka, J. Mol. Spectrosc. **153**, 760 (1992).
3. M. Katsuragawa and K. Hakuta, Opt. Lett. **25**, 177 (2000).
4. M. Fushitani, S. Kuma, Y. Miyamoto, H. Katsuki, T. Wakabayashi, T. Momose, and A. F. Vilesov, Opt. Lett. **28**, 37 (2003).
5. B. J. McCall, A. J. Huneycutt, R. J. Saykally, C. M. Lindsay, T. Oka, M. Fushitani, Y. Miyamoto, and T. Momose, Appl. Phys. Lett. **82**, 1350 (2003).
6. K. E. Kuyanov, T. Momose, and A. F. Vilesov, Appl. Opt. **43**, 6023 (2004).
7. H. Hoshina, D. Skvortsov, B. G. Sartakov, and A. F. Vilesov, J. Chem. Phys. **132**, 074302 (2010).
8. J. K. Brasseur, K. S. Repasky, and J. L. Carlsten, Opt. Lett. **23**, 367 (1998).
9. L. S. Meng, K. S. Repasky, P. A. Roos, and J. L. Carlsten, Opt. Lett. **25**, 472 (2000).
10. L. S. Meng, P. A. Roos, K. S. Repasky, and J. L. Carlsten, Opt. Lett. **26**, 426 (2001).
11. R. G. Bohn and C. F. Mate, Phys. Rev. B **2**, 2121 (1970).
12. NIST Cryogenic Technologies Group, Material Properties Compilation, available at: http://cryogenics.nist.gov.
13. B. A. Tom, S. Bhasker, Y. Miyamoto, T. Momose, and B. J. McCall, Rev. Sci. Instrum. **80**, 016108 (2009).
14. M. Suzuki, M. Katsuragawa, R. S. D. Sihombing, J. Z. Li, and K. Hakuta, J. Low Temp. Phys. **111**, 463 (1998).
15. P. C. Souers, *Hydrogen Properties for Fusion Energy* (University of California, 1986).
16. T. Momose, J. Low Temp. Phys. **111**, 469 (1998).
17. D. P. Weliky, K. E. Kerr, T. J. Byers, Y. Zhang, T. Momose, and T. Oka, J. Chem. Phys. **105**, 4461 (1996).

APPENDIX D

ESTIMATED PRESSURE CALCULATION

Shown here is the calculation for estimating the pressure in the vacuum chamber after the skimmer while operating the supersonic expansion discharge source, as discussed in Chapter 4.

D.1 Throughput through Skimmer

The skimmer has an orifice diameter of 3 mm. The following calculation is based on a hydrogen expansion (a little bit of N_2 is seeded in H_2 to make HN_2^+). The *throughput* or mass flow rate of the hydrogen gas expansion through the skimmer is calculated by

$$\text{Throughput} = \text{Molecule velocity} \times \text{Number density} \times \text{Area of orifice} \quad \text{(D.1)}$$

This gives a throughput in moles/s or molecules/s. If number density is converted to pressure, the throughput is expressed in units of Torr·L/s.

The area of the orifice is $\pi(1.5\text{ mm})^2$ or 7×10^{-6} m^2.

The average velocity of the molecules is calculated using the equation for the speed of sound for an ideal gas:

$$c_{\text{ideal}} = \sqrt{\frac{\gamma kT}{m}} \quad \text{(D.2)}$$

The heat capacity ratio γ is 7/5 for a diatomic gas; the temperature T is assumed to be 20 K in the supersonic expansion; and the mass of H_2 m is 3.35×10^{-27} kg. This gives a speed of sound c_{ideal} of 340 m/s. From Figure 2.5 of Reference [80], the Mach number at centerline for a diatomic gas at a characteristic distance of $x/d = 3.33$ (corresponding to a source-skimmer distance of about 1 cm) is $M \sim 5$. Thus, the molecular velocity at

the skimmer orifice is approximately 1700 m/s.

The number density of H_2 at the skimmer orifice is estimated using Equation 2.6 from Reference [80]:

$$(\rho/\rho_0) = (n/n_0) = (T/T_0)^{1/(\gamma-1)} = (1 + \frac{\gamma-1}{2}M^2)^{-1/(\gamma-1)} \tag{D.3}$$

where ρ is the number density, n is the number of molecules, the subscript 0 denotes a property at stagnation (in the source before the nozzle), and M is the Mach number. Putting $M = 5$ and $\gamma = 7/5$ into Equation D.3 gives a number density ratio of 0.0113. Multiplying this by the stagnant number density should then give the approximate molecular number density at the skimmer orifice. If we assume a stagnant pressure of 2 bar [44] , the stagnant number density can be approximated by the ideal gas law. At 300 K, the stagnant number density is ≈80 mol/m^3. Multiplying this by 0.0113 gives a molecular number density at the skimmer orifice of 5.48×10^{23} m^{-3}, or 5.48×10^{17} cm^{-3}. This can be converted into pressure, assuming ideal gas conditions, with the ideal gas law. Again assuming a T of 20 K, the ideal gas law gives a pressure of ≈1.1 Torr.

Multiplying the pressure, area, and gas velocity gives

$$\begin{aligned}
\text{Throughput} &= \text{Molecule velocity} \times \text{Area} \times \text{Pressure} \\
&= 1700 \text{ m/s} \times (7 \times 10^{-6}) \text{ m}^2 \times 1.1 \text{ Torr} \\
&= 0.013 \text{ Torr m}^3/\text{s} \\
&= 13 \text{ Torr L/s, because } 1 \text{ m}^3 = 1000 \text{ L}
\end{aligned}$$

D.2 Effective Pumping Speed and Conductance

The pumping speed of the Leybold pump is 2000 L/s. However, it should be conductance-limited by the six-way cross and the 8" CF tee. The effective pumping speed (EPS) can be calculated by

$$\frac{1}{EPS} = \frac{1}{PS} + \frac{1}{C} \tag{D.4}$$

where C is the total conductance of the vacuum nipples, tees, and crosses. After measuring or estimating the diameters and lengths of the sections of

chambers through which the gas would flow, a table from Reference [114] is used to estimate the conductances. These were then added in series to get the total conductance.

C_1 is the conductance of the right angle from the port of the pump to the flange attached to the tee. It can be estimated by summing the lengths of the two segments of the right angle, finding the conductance, and dividing by 2. First, the expression L/a is found as follows:

$$\begin{aligned} L &= 3\tfrac{9}{16}\text{"} \times 2 = 7.125\text{ "} = 18.1\text{ cm} \\ a\text{(inner tube radius)} &= 7.26\text{ cm} \\ L/a &= 2.49 \end{aligned}$$

From the table, the conductance should be between 922.8 L/s and 644.9 L/s. Interpolation with a linear fit gives the value to be 896.9 L/s. Half of this is $C_1 = 448.5$ L/s.

C_2 is the conductance of the 8" CF tee between the source chamber and the first bender. At $13\frac{13}{16}$" long, C_2 is

$$\begin{aligned} L &= 13\tfrac{13}{16}\text{"} = 35.1\text{ cm} \\ L/a &= 35.1\text{ cm}/7.26\text{ cm} = 4.8 \end{aligned}$$

From a similar interpolation of the table, $C_2 \approx 684.9$ L/s.

Because these conductances are in series, the combined conductance C_{TOTAL} is

$$\frac{1}{C_{TOTAL}} = \frac{1}{C_1} + \frac{1}{C_2} \tag{D.5}$$

which gives $C_{TOTAL} = 285$ L/s.

The effective pumping speed, then, is

$$\begin{aligned}\frac{1}{EPS} &= \frac{1}{PS} + \frac{1}{C_{TOTAL}} \\ &= \frac{1}{2000 \text{ L/s}} + \frac{1}{285 \text{ L/s}} \\ &= 0.00419 \text{ s/L} \\ EPS &= 250 \text{ L/s}\end{aligned}$$

D.3 Pressure

Finally,

$$\begin{aligned}\text{Pressure} &= \frac{\text{Throughput}}{EPS} \\ &= \frac{13 \text{ Torr L/s}}{250 \text{ L/s}} \\ &\approx 0.050 \text{ Torr} = 50 \text{ mTorr}\end{aligned} \tag{D.6}$$

APPENDIX E

ESTIMATED ROTATIONAL TEMPERATURE DATA

This appendix shows the data used and explains details for estimating the rotational temperature for CH_4, H_3^+, and HN_2^+

E.1 CH_4 Rotational Temperature Estimate

The peak-to-peak intensity (I_{pp}) of a methane rovibrational transition acquired with wm-NICE-OHMS was taken as the minimum of the line on the blue (that is, high frequency) side of the line to the maximum of the line, as shown in Figure E.1 The blue side of the line was chosen because it was

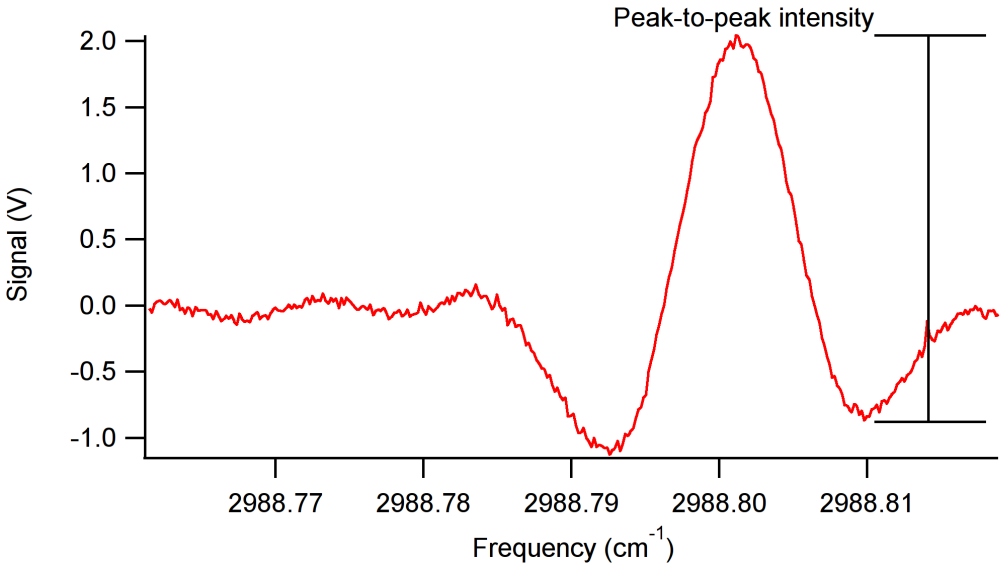

Figure E.1: Wavelength modulation NICE-OHMS scan of methane demonstrating what was taken as the peak-to-peak intensity.

ensured that the frequency range from the blue side minimum intensity value to the maximum value was obtained in one cavity sweep, so that any change in the NICE-OHMS baseline would not affect the peak-to-peak intensity

measurement. Only the dispersion lineshape was considered because the absorption lineshape may have been affected by optical saturation in this setup. Each peak-to-peak intensity (in volts) was scaled for the sensitivity setting of the lock-in amplifier (2 mV for each scan) to obtain an adjusted value. This value was then normalized by the amplification of the heterodyne detection system (a gain equal to $10^{18/20} \approx 7.9$) and to the mean DC voltage from the detector while scanning off of the line to normalize for laser power at each wavelength, obtaining a normalized intensity. Three scans for each transition were acquired, normalized in this way, and averaged, giving I_{avgpp}^{norm}. The average intensity for each transition was then normalized by a measure of the intrinsic linestrength, given by

$$\begin{aligned} S &= g''(\frac{g'}{g''})A_{21} \\ &= g'A_{21} \end{aligned} \tag{E.1}$$

where g'' is the lower state degeneracy of the transition, g' is the upper state degeneracy of the transition, and A_{21} is the transition's Einstein A coefficient. All three of these values were obtained from HITRAN [89]. The product $\frac{g'}{g''}A_{21}$ is proportional to the transition dipole moment squared, as detailed in Reference [115] explaining the HITRAN entries. The natural logarithm of the ratio I_{avgpp}^{norm}/S was taken and this value is plotted against the lower state energy for each transition. The rotational temperature T is obtained from the slope of the linear fit, which is equal to $-1/kT$. The temperature determined from this fit is 300 ± 30K. The intensities listed in the HITRAN entry for methane were tested with this calculation and the resultant temperature came to within 4 K of the input temperature of 296 K.

The data used for the Boltzmann analysis of methane shown in Figure 4.13 are given in Table E.1.

Data for Boltzmann Plot of Methane

Transition	Frequency (cm^{-1})	Einstein A coefficient (s^{-1})[a]	g''^a	g'^a	Lower State Energy (cm^{-1})[a]	I_{avgpp}^{norm}
P(3)A_2	2988.795	23.47	35	25	62.8781	0.00623
P(6)A_2	2958.536	22.05	65	55	219.9197	0.00569
P(7)A_2	2948.107	21.05	75	65	293.1541	0.00388
P(9)A_2	2926.700	20.51	95	85	470.8727	0.00268

Table E.1: Data for the methane Boltzmann analysis in Figure 4.13.
[a]Values obtained from the HITRAN database [89].

E.2 H_3^+ Rotational Temperature Estimate

Below, Table E.2 shows the peak-to-peak intensity data used to calculate the estimated temperature of H_3^+ in Chapter 4. Here, I_{pp} is the peak-to-peak

Intensities of H_3^+ Transitions

Transition	I_{pp} (V)	DC Voltage (V)	I_{pp}^{norm}
R(1,0)	3.7727	0.227	16.6198237885
R(1,0)	3.7812	0.227	16.6572687225
R(1,0)	3.7197	0.227	16.3863436123
R(1,0)	3.5594	0.227	15.6801762115
R(1,0)	3.6422	0.227	16.0449339207
R(1,1)^u	1.0741	0.165	6.5096969697
R(1,1)^u	1.1136	0.165	6.7490909091
R(1,1)^u	1.0608	0.165	6.4290909091
R(1,1)^u	1.0329	0.165	6.2600000000
R(1,1)^u	1.1422	0.165	6.9224242424

Table E.2: Intensity measurements of several scans of the R(1,0) and R(1,1)^u lines of H_3^+ obtained in the supersonic expansion discharge source.

intensity measured for each line, and I_{pp}^{norm} is the peak-to-peak intensity normalized to the DC voltage from the InSb detector recorded for each scan. The average R(1,0) intensity is calculated to be 16.3±0.4 V (with an uncertainty of one standard deviation), and the average R(1,1)^u intensity is calculated

as 6.6±0.3 V. The rotational temperature is then estimated by [116]:

$$\begin{aligned} \frac{\mu^2_{\mathrm{R(1,1)}^u}}{\mu^2_{\mathrm{R(1,0)}}}\frac{I_{\mathrm{R(1,0)}}}{I_{\mathrm{R(1,1)^u}}} &= \frac{g_{\mathrm{R(1,0)}}}{g_{\mathrm{R(1,1)^u}}}\exp(-\frac{E_{(1,0)}-E_{(1,1)}}{k_B T_{ex}}) \\ T_{ex} &= \frac{-(E_{(1,0)}-E_{(1,1)})}{k_B \ln\left[\frac{g_{\mathrm{R(1,1)^u}}}{g_{\mathrm{R(1,0)}}}\frac{\mu^2_{\mathrm{R(1,1)}^u}}{\mu^2_{\mathrm{R(1,0)}}}\frac{I_{\mathrm{R(1,0)}}}{I_{\mathrm{R(1,1)^u}}}\right]}, \end{aligned} \tag{E.2}$$

where μ is the transition dipole moment in D, I is the peak-to-peak intensity observed in the spectrum, g represents the nuclear spin degeneracy, E is the lower state energy of a transition, k_B is the Boltzmann constant, and T_{ex} is the excitation temperature that is used as an estimate of the rotational temperature. The constants used in this equation are listed in Table E.3. Substituting in the appropriate average intensity for $I_{\mathrm{R(1,0)}}$ and $I_{\mathrm{R(1,1)^u}}$ and

Constants for H_3^+ Temperature Estimate	
$E_{(1,0)}$	86.96 cm^{-1}
$E_{(1,1)^u}$	64.121 cm^{-1}
$g_{\mathrm{R(1,0)}}$	4
$g_{\mathrm{R(1,1)^u}}$	2
$\mu^2_{\mathrm{R(1,0)}}$	0.0259 D^2
$\mu^2_{\mathrm{R(1,1)}^u}$	0.0158 D^2
k_B	0.695 cm^{-1}/K

Table E.3: Constants used in Equation E.2 The lower state energies are from Reference [85] and the square of the transition dipole moments are from Reference [117].

propagating the uncertainty results in an estimated temperature of 120 ± 20 K.

E.3 HN_2^+ Rotational Temperature Estimate

A Boltzmann plot was constructed to estimate the rotational temperature of HN_2^+ produced from the supersonic expansion discharge source. Table E.4 shows the intensities of HN_2^+ lines obtained from the two lock-in amplifiers (the input of each lock-in amplifier is output from a different electronic mixer, with each referenced 90° from each other in phase). The peak-to-peak intensities were normalized to the DC voltage obtained off of the line. The

average normalized intensity for each transition is then normalized by the linestrength of each transition, giving I/S. For the purpose of this analysis, the linestrength is represented by the square of the transition dipole moment, given by Equation 2-15 of Reference [95] (for l=0):

$$|\mu_{ij}|^2 = \mu^2 \frac{(J+1)}{2J+1} \tag{E.3}$$

Here, $|\mu_{ij}|^2$ is the square of the transition dipole moment, μ^2 is the square of the permanent dipole moment, and J is the total angular momentum quantum number. The permanent dipole moment has been reported as 3.4 D [96]. The natural logarithm of I/S is then plotted as a function of the lower state energy of each transition. The lower state energy is calculated from Equation 7 of Reference [84]:

$$E = B[J(J+1) - l_2^2] - D[J(J+1) - l_2^2]^2 + H[J(J+1) - l_2^2]^3 \tag{E.4}$$

Reference [84] gives a lower state B constant of 1.553922 cm^{-1} and a D constant of 2.893×10^{-6} for the ground vibrational state; H and l will be zero for this state.

Table E.5 presents the results of these calculations for each transition. The Boltzmann plot from this data for Lock-in Amplifier 2 is shown in Figure 5.5. The slopes of the fit lines are -0.035 ± 0.009 for Lock-in Amplifier 1 and -0.040 ± 0.008 for Lock-in Amplifier 2. Because the slopes are equal to $\frac{1}{k_B T}$, the corresponding temperatures are 40±10 and 36±7 K, respectively.

Intensities of HN_2^+ Transitions

Transition	I_{pp} (V)	DC Voltage (V)	I_{pp}^{norm}	Average I_{pp}^{norm}
Lock-in Amplifier 1:				
R0	1.0189	0.075	13.585	
R0	0.9403	0.075	12.54	
R0	0.9819	0.075	13.09	
				13.1(5)
R1	0.79751	0.043	18.547	
R1	0.78155	0.043	18.176	
R1	0.80074	0.043	18.622	
				18.4(2)
R2	1.7106	0.071	24.093	
R2	1.7107	0.071	24.094	
R2	1.7778	0.071	25.039	
				24.4(5)
R3	1.9339	0.076	25.446	
R3	1.8082	0.076	23.792	
R3	1.9373	0.076	25.491	
				24.910(968)
Lock-in Amplifier 2:				
R0	1.0536	0.075	14.048	
R0	1.0556	0.075	14.075	
R0	1.1331	0.075	15.108	
				14.4(6)
R1	0.89259	0.043	20.758	
R1	0.90232	0.043	20.984	
R1	0.84825	0.043	19.727	
				20.5(7)
R2	1.8159	0.071	25.576	
R2	1.8456	0.071	25.994	
R2	1.8462	0.071	26.003	
				25.9(2)
R3	1.8864	0.076	24.821	
R3	1.9523	0.076	25.688	
R3	1.9529	0.076	25.696	
				25.4(5)

Table E.4: Intensity measurements of several scans of the R(0), R(1), R(2), R(3) lines of HN_2^+ obtained in the supersonic expansion discharge source. Uncertainties on the averages are plus and minus one standard deviation.

HN_2^+ Boltzmann Analysis Data				
Transition	Lower state energy (cm^{-1})	$\lvert\mu_{ij}\rvert^2$ (D^2)	Average I_{pp}^{norm}	ln $\frac{I_{pp}^{norm}}{\lvert\mu_{ij}\rvert^2}$
Lock-in Amplifier 1:				
R0	0	11.56	13.1	0.12(4)
R1	3.108	7.707	18.4	−0.23(1)
R2	9.324	6.936	24.4	−0.35(2)
R3	18.65	6.606	24.9	−0.62(4)
Lock-in Amplifier 2:				
R0	0	11.56	14.4	0.22(4)
R1	3.108	7.707	20.5	−0.12(3)
R2	9.324	6.936	25.9	−0.294(9)
R3	18.65	6.606	25.4	−0.60(2)

Table E.5: Data used for the Boltzmann plot of HN_2^+.

REFERENCES

[1] Fulvio Cacace and Giulia de Petris. Mass spectrometric study of simple main group molecules and ions important in atmospheric processes. *International Journal of Mass Spectrometry*, 194(1):1–10, 2000.

[2] Nicholas S. Shuman, Donald E. Hunton, and Albert A. Viggiano. Ambient and modified atmospheric ion chemistry: From top to bottom. *Chemical Reviews*. Article ASAP.

[3] Nora M. Semo and Walter S. Koski. Some ion-molecule reactions pertinent to combustion. *The Journal of Physical Chemistry*, 88(22):5320–5324, 1984.

[4] C. Vinckier, Michael P. Gardner, and Kyle D. Bayes. A study of some primary and secondary chemi-ionization reactions in hydrocarbon oxidations. *Symposium (International) on Combustion*, 16(1):881–889, 1977.

[5] Wolf D. Geppert and Mats Larsson. Experimental investigations into astrophysically relevant ionic reactions. *Chemical Reviews*, 113(12):8872–8905, 2013.

[6] D. A. Williams and T. W. Hartquist. *The Cosmic-Chemical Bond: Chemistry from the Big Bang to Planet Formation*. The Royal Society of Chemistry, 2013. p. 12.

[7] B. J. McCall. *Spectroscopy of H_3^+ in Laboratory and Astrophysical Plasmas*. PhD thesis, University of Chicago, 2001. p. 73.

[8] Edmund T. White, Jian Tang, and Takeshi Oka. CH_5^+: The infrared spectrum observed. *Science*, 284(5411):135–137, 1999.

[9] Oskar Asvany, Koichi M. T. Yamada, Sandra Brnken, Alexey Potapov, and Stephan Schlemmer. Experimental ground-state combination differences of CH_5^+. *Science*, 347(6228):1346–1349, 2015.

[10] Nick Indriolo and Benjamin J. McCall. Investigating the cosmic-ray ionization rate in the galactic diffuse interstellar medium through observations of H_3^+. *The Astrophysical Journal*, 745(1):91, 2012.

[11] Nick Indriolo, D. A. Neufeld, M. Gerin, P. Schilke, A. O. Benz, B. Winkel, K. M. Menten, E. T. Chambers, John H. Black, S. Bruderer, E. Falgarone, B. Godard, J. R. Goicoechea, H. Gupta, D. C. Lis, V. Ossenkopf, C. M. Persson, P. Sonnentrucker, F. F. S. van der Tak, E. F. van Dishoeck, Mark G. Wolfire, and F. Wyrowski. Herschel survey of galactic OH^+, H_2O^+, and H_3O^+: Probing the molecular hydrogen fraction and cosmic-ray ionization ratedif. *The Astrophysical Journal*, 800(1):40, 2015.

[12] D. Chomiak, A. Taleb-Bendiab, S. Civiš, and T. Amano. Millimetre-wave laboratory detection of H_2COH^+. *Canadian Journal of Physics*, 72(11-12):1078–1081, 1994.

[13] Lewis E. Snyder, David Buhl, B. Zuckerman, and Patrick Palmer. Microwave detection of interstellar formaldehyde. *Phys. Rev. Lett.*, 22:679–681, Mar 1969.

[14] T. Amano and H. E. Warner. Laboratory detection of protonated formaldehyde (H_2COH^+). *Astrophys. J.*, 342:L99–L101, July 1989.

[15] Masatoshi Ohishi, Shin-ichi Ishikawa, Takayoshi Amano, Hidehiko Oka, William M. Irvine, James E. Dickens, L. M. Ziurys, and A. J. Apponi. Detection of a new interstellar molecular ion, H_2COH^+ (protonated formaldehyde). *The Astrophysical Journal Letters*, 471(1):L61, 1996.

[16] Christopher S. Gudeman, Marianne H. Begemann, Jürgen Pfaff, and Richard J. Saykally. Velocity-modulated infrared laser spectroscopy of molecular ions: The ν_1 band of HCO^+. *Physical Review Letters*, 50:727–731, Mar 1983.

[17] Mark W. Crofton and Takeshi Oka. Infrared studies of molecular ions. I. The ν_3 band of NH_4^+. *The Journal of Chemical Physics*, 79(6):3157–3158, 1983.

[18] Serena K. Stephenson and Richard J. Saykally. Velocity modulation spectroscopy of ions. *Chemical Reviews*, 105(9):3220–3234, 2005.

[19] Brian M. Siller, Michael W. Porambo, Andrew A. Mills, and Benjamin J. McCall. Noise immune cavity enhanced optical heterodyne velocity modulation spectroscopy. *Optics Express*, 19(24):24822–24827, Nov 2011.

[20] Kyle N. Crabtree, James N. Hodges, Brian M. Siller, Adam J. Perry, Joseph E. Kelly, Paul A. Jenkins II, and Benjamin J. McCall. Sub-Doppler mid-infrared spectroscopy of molecular ions. *Chemical Physics Letters*, 551(0):1–6, 2012.

[21] Giel Berden, Rudy Peeters, and Gerard Meijer. Cavity ring-down spectroscopy: Experimental schemes and applications. *International Reviews in Physical Chemistry*, 19(4):565–607, 2000.

[22] Anthony O'Keefe and David A. G. Deacon. Cavity ring-down optical spectrometer for absorption measurements using pulsed laser sources. *Review of Scientific Instruments*, 59(12):2544–2551, 1988.

[23] K. Nakagawa, T. Katsuda, A.S. Shelkovnikov, M. de Labachelerie, and M. Ohtsu. Highly sensitive detection of molecular absorption using a high finesse optical cavity. *Optics Communications*, 107(5–6):369–372, 1994.

[24] Richard Engeln, Giel Berden, Rudy Peeters, and Gerard Meijer. Cavity enhanced absorption and cavity enhanced magnetic rotation spectroscopy. *Review of Scientific Instruments*, 69(11):3763–3769, 1998.

[25] G. Gagliardi and L. Gianfrani. Trace-gas analysis using diode lasers in the near-IR and long-path techniques. *Optics and Lasers in Engineering*, 37(5):509–520, 2002.

[26] G.C. Bjorklund, M.D. Levenson, W. Lenth, and C. Ortiz. Frequency modulation (FM) spectroscopy. *Applied Physics B*, 32(3):145–152, 1983.

[27] Jun Ye. *Ultrasensitive High Resolution Laser Spectroscopy and its Application to Optical Frequency Standards*. PhD thesis, University of Colorado Boulder, 1997.

[28] Jun Ye, Long-Sheng Ma, and John L. Hall. Ultrasensitive detections in atomic and molecular physics: demonstration in molecular overtone spectroscopy. *J. Opt. Soc. Am. B*, 15(1):6–15, Jan 1998.

[29] Patrick Ehlers, Isak Silander, Junyang Wang, and Ove Axner. Fiber-laser-based noise-immune cavity-enhanced optical heterodyne molecular spectrometry instrumentation for Doppler-broadened detection in the 10^{-12} cm^{-1} $Hz^{-1/2}$ region. *Journal of the Optical Society of America B: Optical Physics*, 29(6):1305–1315, Jun 2012.

[30] Andrew A. Mills, Brian M. Siller, Michael W. Porambo, Manori Perera, Holger Kreckel, and Benjamin J. McCall. Ultra-sensitive high-precision spectroscopy of a fast molecular ion beam. *The Journal of Chemical Physics*, 135(22):224201, 2011.

[31] J. K. G. Watson, S. C. Foster, A. R. W. McKellar, P. Bernath, T. Amano, F. S. Pan, M. W. Crofton, R. S. Altman, and T. Oka. The infrared spectrum of the ν_2 fundamental band of the H_3^+ molecular ion. *Canadian Journal of Physics*, 62(12):1875–1885, 1984.

[32] Brian M. Siller. *New Techniques for Sub-Doppler Spectroscopy of Molecular Ions*. PhD thesis, University of Illinois, 2013.

[33] James N. Hodges, Adam J. Perry, Paul A. Jenkins, Brian M. Siller, and Benjamin J. McCall. High-precision and high-accuracy rovibrational spectroscopy of molecular ions. *The Journal of Chemical Physics*, 139(16):164201, 2013.

[34] Adam J. Perry, James N. Hodges, Charles R. Markus, G. Stephen Kocheril, and Benjamin J. McCall. Communication: High precision sub-Doppler infrared spectroscopy of the HeH^+ ion. *The Journal of Chemical Physics*, 141(10):101101, 2014.

[35] T. Amano. Difference-frequency laser spectroscopy of molecular ions with a hollow-cathode cell: extended analysis of the ν_1 band of H_2D^+. *J. Opt. Soc. Am. B*, 2(5):790–793, May 1985.

[36] Kyle N. Crabtree, Carrie A. Kauffman, Brian A. Tom, Eftalda Beka, Brett A. McGuire, and Benjamin J. McCall. Nuclear spin dependence of the reaction of H_3^+ with H_2. II. experimental measurements. *The Journal of Chemical Physics*, 134(19):194311, 2011.

[37] Christopher M. Lovejoy and David J. Nesbitt. Slit pulsed valve for generation of long-path-length supersonic expansions. *Review of Scientific Instruments*, 58(5):807–811, 1987.

[38] Terry A. Miller, B. R. Zegarski, Trevor J. Sears, and V. E. Bondybey. Gas-phase emission spectra of supercooled organic ions. *The Journal of Physical Chemistry*, 84(24):3154–3156, 1980.

[39] P. C. Engelking. Corona excited supersonic expansion. *Review of Scientific Instruments*, 57(9):2274–2277, 1986.

[40] L. I. Yeh, M. Okumura, J. D. Myers, J. M. Price, and Y. T. Lee. Vibrational spectroscopy of the hydrated hydronium cluster ions $H_3O^+ \cdot (H_2O)_n$ (n=1, 2, 3). *The Journal of Chemical Physics*, 91(12):7319–7330, 1989.

[41] Xu Yunjie, M. Fukushima, T. Amano, and A.R.W. McKellar. Infrared absorption spectroscopy of molecular ions in a corona-discharge slit expansion. *Chemical Physics Letters*, 242:126–131, 1995.

[42] David T. Anderson, Scott Davis, Timothy S. Zwier, and David J. Nesbitt. An intense slit discharge source of jet-cooled molecular ions and radicals ($T_{rot} \leq 30$ K). *Chemical Physics Letters*, 258(1–2):207–212, 1996.

[43] Scott Davis, Michal Fárník, Dairene Uy, and David J. Nesbitt. Concentration modulation spectroscopy with a pulsed slit supersonic discharge expansion source. *Chemical Physics Letters*, 344:23–30, 2001.

[44] Kyle N. Crabtree, Carrie A. Kauffman, and Benjamin J. McCall. Note: A modular and robust continuous supersonic expansion discharge source. *Review of Scientific Instruments*, 81(8):086103, 2010.

[45] Alan Carrington and Peter J. Sarre. Electronic absorption spectrum of CO^+ in an ion beam. *Molecular Physics*, 33(5):1495–1497, 1977.

[46] E. Alvarez, A. Arnesen, A. Bengtson, R. Hallin, C. Mayige, C. Nordling, T. Noreland, and Ö. Staaf. Hyperfine structure of the $5p^5\ ^2P_{3/2}5d[7/2]^\circ_4$,$^2P_{3/2}5d[3/2]^\circ_2$, and $^2P_{3/2}6p[5/2]_3$ levels in Cs II measured with beam-laser technique. *Opt. Lett.*, 4(9):268–270, Sep 1979.

[47] M. Carre, M. Druetta, M.L. Gaillard, H.H. Bukow, M. Horani, A.L. Roche, and M. Velghe. Laser spectroscopy of the O_2^+ molecular ion using a fast ion beam: Fine structure and predissociation lifetimes in the $b\ ^4\Sigma_g^-$ state. *Molecular Physics*, 40(6):1453–1480, 1980.

[48] William H. Wing, George A. Ruff, Willis E. Lamb, and Joseph J. Spezeski. Observation of the infrared spectrum of the hydrogen molecular ion HD^+. *Phys. Rev. Lett.*, 36:1488–1491, Jun 1976.

[49] J. V. Coe, J. C. Owrutsky, E. R. Keim, N. V. Agman, D. C. Hovde, and R. J. Saykally. Sub-Doppler direct infrared laser absorption spectroscopy in fast ion beams: The fluorine hyperfine structure of HF^+. *The Journal of Chemical Physics*, 90(8):3893–3902, 1989.

[50] Kenji Anzai, Xiaoming Gao, Hiroyuki Sasada, and Naohiro Yoshida. Narrow Lamb dip of 3.4 μm band transition of methane with difference frequency generation and enhancement cavity. *Japanese Journal of Applied Physics*, 45(4R):2771, 2006.

[51] Weiguang Ma, Aleksandra Foltynowicz, and Ove Axner. Theoretical description of Doppler-broadened noise-immune cavity-enhanced optical heterodyne molecular spectroscopy under optically saturated conditions. *Journal of the Optical Society of America B: Optical Physics*, 25(7):1144–1155, Jul 2008.

[52] Ove Axner, Weiguang Ma, and Aleksandra Foltynowicz. Sub-Doppler dispersion and noise-immune cavity-enhanced optical heterodyne molecular spectroscopy revised. *Journal of the Optical Society of America B: Optical Physics*, 25(7):1166–1177, Jul 2008.

[53] Nicola J. van Leeuwen and Andrew C. Wilson. Measurement of pressure-broadened, ultraweak transitions with noise-immune cavity-enhanced optical heterodyne molecular spectroscopy. *J. Opt. Soc. Am. B*, 21(10):1713–1721, Oct 2004.

[54] L. S. Ma, J. Ye, P. Dube, and J. L. Hall. Ultrasensitive frequency-modulation spectroscopy enhanced by a high-finesse optical cavity: Theory and application to ovetone transitions of C_2H_2 and C_2HD. *J. Opt. Soc. Am. B*, 16:2255–2268, 1999.

[55] C. Ishibashi and H. Sasada. Highly sensitive cavity-enhanced sub-Doppler spectroscopy of a molecualr overtone band with a 1.66 μm tunable diode laser. *Japan. J. Appl. Phys. Part 1*, 38:920–922, 1999.

[56] F. M. Schmidt, A. Foltynowicz, W. Ma, and O. Axner. Fiber-laser-based noise-immune cavity-enhanced optical heterodyne molecular spectrometry for Doppler-broadened detection of C_2H_2 in the parts per trillion range. *J. Opt. Soc. Am. B*, 24:1392–1405, 2007.

[57] F. M. Schmidt, A. Foltynowicz, W. Ma, T. Lock, and O. Axner. Doppler-broadened fiber-laser-based NICE-OHMS–Improved detectability. *Opt. Ex.*, 15:10822–10831, 2007.

[58] M. S. Taubman, T. L. Myers, B. D. Cannon, and R. M. Williams. Stabilization, injection and control of quantum cascade lasers, and their application to chemical sensing in the infrared. *Spectrochim. Acta A*, 60:3457–3468, 2004.

[59] E. A. Donley, T. P. Heavner, F. Levi, O. Tataw, and S. R. Jefferts. Double-pass acousto-optic modulator system. *Rev. Sci. Instrum.*, 76:063112, 2005.

[60] R. W. P. Drever, J. L. Hall, F. V. Kowalski, J. Hough, G. M. Ford, A. J. Munley, and H. Ward. Laser phase and frequency stabilization using an optical resonator. *Appl. Phys. B*, 31:97–105, 1983.

[61] A. Foltynowicz, F.M. Schmidt, W. Ma, and O. Axner. Noise-immune cavity-enhanced optical heterodyne molecular spectroscopy: Current status and future potential. *Applied Physics B*, 92(3):313–326, 2008.

[62] Edward A. Whittaker, Manfred Gehrtz, and Gary C. Bjorklund. Residual amplitude modulation in laser electro-optic phase modulation. *Journal of the Optical Society of America B: Optical Physics*, 2(8):1320–1326, Aug 1985.

[63] N. C. Wong and J. L. Hall. Servo control of amplitude modulation in frequency-modulation spectroscopy: Demonstration of shot-noise-limited detection. *J. Opt. Soc. Am. B*, 2:1527–1533, 1985.

[64] J. F. Kelly, R. L. Sams, T. A. Blake, M. Newburn, J. Moran, M. L. Alexander, and H. Kreuzer. A capillary absorption spectrometer for stable carbon isotope ratio ($^{13}C/^{12}C$) analysis in very small samples. *Review of Scientific Instruments*, 83(2):023101, 2012.

[65] H. Kreckel, H. Bruhns, K. A. Miller, E. Whlin, A. Davis, S. Hckh, and D. W. Savin. A simple double-focusing electrostatic ion beam deflector. *Review of Scientific Instruments*, 81(6):063304, 2010.

[66] Andrew Allen Mills. *Design, Construction, and Characterization of an Ultra-sensitive, High-precision Fast Ion-beam Spectrometer for the Study of Molecular Ions*. PhD thesis, University of Illinois at Urbana-Champaign, 2011.

[67] Brian M. Siller, Andrew A. Mills, and Benjamin J. McCall. Cavity-enhanced velocity modulation spectroscopy. *Opt. Lett.*, 35(8):1266–1268, Apr 2010.

[68] H_3^+ Resource Center. http://h3plus.uiuc.edu/. Accessed: 05-01-2015.

[69] Takeshi Oka. Observation of the infrared spectrum of h_3^+. *Phys. Rev. Lett.*, 45:531–534, Aug 1980.

[70] Brian M. Siller, James N. Hodges, Adam J. Perry, and Benjamin J. McCall. Indirect rotational spectroscopy of HCO^+. *The Journal of Physical Chemistry A*, 117(39):10034–10040, 2013. PMID: 23758579.

[71] C. Western. Pgopher, a program for simulating rotational structure, 2009. University of Bristol.

[72] B. Niu, D. A. Shirley, and Y. Bai. High resolution photoelectron spectroscopy and femtosecond intramolecular dynamics of H_2CO^+ and D_2CO^+. *J. Chem. Phys.*, 98:4377–4390, 1993.

[73] A. M. Schulenburg, M. Meisinger, P. P. Radi, and F. Merkt. The formaldehyde cation: Rovibrational energy level structure and Coriolis interaction near the adiabatic ionization threshold. 250:44–50, 2008.

[74] Ricardo Perez, John M. Brown, Yurii Utkin, Jiaxiang Han, and Robert F. Curl. Observation of hot bands in the infrared spectrum of H_2CO. *Journal of Molecular Spectroscopy*, 236(2):151–157, 2006.

[75] Oskar Asvany, Sandra Brnken, Lars Kluge, and Stephan Schlemmer. Coltrap: a 22-pole ion trapping machine for spectroscopy at 4 K. *Applied Physics B*, 114(1-2):203–211, 2014.

[76] S. E. Maxwell, N. Brahms, R. deCarvalho, D. R. Glenn, J. S. Helton, S. V. Nguyen, D. Patterson, J. Petricka, D. DeMille, and J. M. Doyle. High-flux beam source for cold, slow atoms or molecules. *Phys. Rev. Lett.*, 95:173201, Oct 2005.

[77] L. Santamaria, V. Di Sarno, I. Ricciardi, S. Mosca, M. De Rosa, G. Santambrogio, P. Maddaloni, and P. De Natale. Assessing the time constancy of the proton-to-electron mass ratio by precision ro-vibrational spectroscopy of a cold molecular beam. *Journal of Molecular Spectroscopy*, 300(0):116–123, 2014. Spectroscopic Tests of Fundamental Physics.

[78] Georg Hilpert, Harold Linnartz, Martina Havenith, J.J. ter Meulen, and W.Leo Meerts. Tunable infrared and far-infrared direct absorption spectroscopy of molecular ions in a supersonic jet expansion. *Chemical Physics Letters*, 219(5–6):384–388, 1994.

[79] Sang Kuk Lee. Pinhole-type glass nozzle for corona excited supersonic expansion. *Chemical Physics Letters*, 358(1–2):110 – 114, 2002.

[80] David R. Miller. *Atomic and Molecular Beam Methods*, volume 1, ed. by Giacinto Scoles, chapter 2: Free Jet Sources, pages 14–53. Oxford University Press, 1988.

[81] R. Campargue. Progress in overexpanded supersonic jets and skimmed molecular beams in free-jet zones of silence. *The Journal of Physical Chemistry*, 88(20):4466–4474, 1984.

[82] D. C. Jordan, R. Barling, and R. B. Doak. Refractory graphite skimmers for supersonic free-jet, supersonic arc-jet, and plasma discharge applications. *Review of Scientific Instruments*, 70(3):1640–1648, 1999.

[83] Eric R. Keim. *Infrared Laser Absorption Spectroscopy of Fast Ion Beams: Cluster Ions*. PhD thesis, University of California at Berkeley, 1992.

[84] Y. Kabbadj, T.R. Huet, B.D. Rehfuss, C.M. Gabrys, and T. Oka. Infrared spectroscopy of highly excited vibrational levels of protonated nitrogen, HN_2^+. *Journal of Molecular Spectroscopy*, 163(1):180–205, 1994.

[85] C. Michael Lindsay and Benjamin J. McCall. Comprehensive evaluation and compilation of H_3^+ spectroscopy. *Journal of Molecular Spectroscopy*, 210(1):60–83, 2001.

[86] E. R. Keim, M. L. Polak, J. C. Owrutsky, J. V. Coe, and R. J. Saykally. Absolute infrared vibrational band intensities of molecular ions determined by direct laser absorption spectroscopy in fast ion beams. *The Journal of Chemical Physics*, 93(5):3111–3119, 1990.

[87] S. Civiš, C.E. Blom, and Per Jensen. Diode laser infrared spectra and potential energy curve for SH^+. *Journal of Molecular Spectroscopy*, 138(1):69–78, 1989.

[88] Philip R. Brown, Paul B. Davies, and Simon A. Johnson. Infrared laser spectroscopy of SH^+. *Chemical Physics Letters*, 132(6):582–584, 1986.

[89] The HITRAN Database. https://www.cfa.harvard.edu/hitran/.

[90] Lambda Research Corporation. OSLO. http://www.lambdares.com/oslo.

[91] Richard D. Thomas. When electrons meet molecular ions and what happens next: Dissociative recombination from interstellar molecular clouds to internal combustion engines. *Mass Spectrometry Reviews*, 27(5):485–530, 2008.

[92] A. Kiendler, St. Aberle, and F. Arnold. Negative chemiions formed in jet fuel combustion: new insights from jet engine and laboratory measurements using a quadrupole ion trap mass spectrometer apparatus. *Atmospheric Environment*, 34(16):2623–2632, 2000.

[93] Oskar Asvany, Frank Bielau, Damian Moratschke, Jrgen Krause, and Stephan Schlemmer. Note: New design of a cryogenic linear radio frequency multipole trap. *Review of Scientific Instruments*, 81(7):076102, 2010.

[94] Michael W. Porambo, Brian M. Siller, Jessica M. Pearson, and Benjamin J. McCall. Broadly tunable mid-infrared noise-immune cavity-enhanced optical heterodyne molecular spectrometer. *Optics Letters*, 37(21):4422–4424, Nov 2012.

[95] Charles H. Townes and Arther L. Schawlow. *Microwave Spectroscopy*. McGraw-Hill, 1955.

[96] M. Havenith, E. Zwart, W. Leo Meerts, and J. J. ter Meulen. Determination of the electric dipole moment of HN_2^+. *The Journal of Chemical Physics*, 93(12):8446–8451, 1990.

[97] Michal Fárník, Scott Davis, Maxim A. Kostin, Oleg L. Polyansky, Jonathan Tennyson, and David J. Nesbitt. Beyond the Born-Oppenheimer approximation: High-resolution overtone spectroscopy of H_2D^+ and D_2H^+. *The Journal of Chemical Physics*, 116(14):6146–6158, 2002.

[98] Feng Dong, Dairene Uy, Scott Davis, Mark Child, and David J. Nesbitt. Supersonically cooled hydronium ions in a slit-jet discharge: High-resolution infrared spectroscopy and tunneling dynamics of HD_2O^+. *The Journal of Chemical Physics*, 122(22):224301, 2005.

[99] Feng Dong and David J. Nesbitt. Jet cooled spectroscopy of H_2DO^+: Barrier heights and isotope-dependent tunneling dynamics from H_3O^+ to D_3O^+. *The Journal of Chemical Physics*, 125(14):144311, 2006.

[100] Samuel Leutwyler, Dieter Klapstein, and John P. Maier. Anomalous rotational distributions in electronic emission of supersonically cooled H_2O^+ ($\tilde{A}\ ^2A_1 \rightarrow \tilde{X}\ ^2B_1$). *Chemical Physics*, 74(3):441–445, 1983.

[101] Satoshi Yamazaki, Masahiro Taki, and Yoshiyasu Fujitani. Rotational relaxation in free jet expansion for n_2 from 300 to 1000 k. *The Journal of Chemical Physics*, 74(8):4476–4479, 1981.

[102] David E. Pritchard, Neil Smith, Richard D. Driver, and Timothy A. Brunner. Power law scaling for rotational energy transfer. *The Journal of Chemical Physics*, 70(5):2115–2120, 1979.

[103] Scott Davis, Feng Dong, and David J. Nesbitt. *Low Temperatures and Cold Molecules*, chapter 5: Molecular Spectroscopy at Low Temperatures: A High Resolution Infrared Retrospective, pages 231–294. Imperial College Press, 2008.

[104] T. R. Huet, C. J. Pursell, W. C. Ho, B. M. Dinelli, and T. Oka. Infrared spectroscopy and equilibrium structure of $H_2O^+(\tilde{X}\ ^2B_1)$. *The Journal of Chemical Physics*, 97(9):5977–5987, 1992.

[105] Bianca M. Dinelli, Mark W. Crofton, and Takeshi Oka. Infrared spectroscopy of the ν_3 band of H_2O^+. *Journal of Molecular Spectroscopy*, 127(1):1–11, 1988.

[106] Molecules in space. I. Physikalisches Institut, Universität zu Köln, https://www.astro.uni-koeln.de/cdms/molecules, Accessed May 26, 2015.

[107] P. J. Bruna, R. J. Hachey, and F. Grein. The electronic structure of the H_2CO^+ radical and higher Rydberg states of H_2CO. *Mol Phys.*, 94:917–928, 1998.

[108] P. Blowers and R. I. Masel. Calculated vibrational spectra for CH_nOH_m species. *J. Phys. Chem. A*, 104:34–44, 2000.

[109] K. C. Sears, J. W. Ferguson, T. J. Dudley, R. S. Houk, and M. S. Gordon. Theoretical investigation of small polyatomic ions observed in inductively coupled plasma mass spectrometry: H_xCO^+ and $H_xN_2^+$ (x = 1,2,3). *J. Phys. Chem. A*, 112:2610–2617, 2008.

[110] J. W. Ferguson, T. J. Dudley, K. C. Sears, S. M. McIntyre, M. S. Gordon, and R. S. Houk. Polyatomic ion in inductively coupled plasma-mass spectrometry part ii: Origins of N_2H^+ and H_xCO^+ ions using experimental measurements combined with calculated energies and structures. *Spectrochimica Acta Part B*, 64:690–696, 2009.

[111] R. T. Wiedmann, M. G. White, K. Wang, and V. McKoy. Rotationally resolved photoionization of polyatomic hydrides: CH_3, H_2O, H_2S, H_2CO. 100:4738–4746, 1994.

[112] W. Klemperer. Astronomical chemistry. *Annu. Rev. Phys. Chem.*, 62:173–184, 2011.

[113] M. W. Porambo. Molecular ion spectroscopy: New methods and the proposed study of H_2CO^+, 2011. Prospectus for Preliminary Examination, http://bjm.scs.illinois.edu/miscpubs/Porambo2011.pdf.

[114] Saul Dushman. *Scientific Foundations of Vacuum Technique*. John Wiley & Sons, Inc., 2nd edition, 1962. p. 99.

[115] L. S. Rothman, C. P. Rinsland, A. Goldman, S. T. Massie, D. P. Edwards, J.-M. Flaud, A. Perrin, C. Camy-Peyret, V. Dana, J.-Y. Mandin, J. Schroeder, A. McCann, R. R. Gamache, R. B. Wattson, K. Yoshino, K. V. Chance, K. W. Jucks, L. R. Brown, V. Nemtchinov, and P. Varanasi. The HITRAN molecular spectroscopic database and HAWKS (HITRAN Atmospheric Workstation): 1996 edition. *Journal of Quantitative Spectroscopy and Radiative Transfer*, 60(5):665–710, 1998.

[116] Kyle Crabtree. Design of a continuous supersonic expansion discharge source for the acquisition of a rotationally-cold vibrational spectrum of CH_5^+ with the SCRIBES instrument, 2009. Prospectus for Preliminary Examination, http://bjm.scs.illinois.edu/miscpubs/Crabtree2009.pdf.

[117] Miwa Goto, Benjamin J. McCall, Thomas R. Geballe, Tomonori Usuda, Naoto Kobayashi, Hiroshi Terada, and Takeshi Oka. Absorption line survey of H_3^+ toward the galactic center sources I. GCS 3-2 and GC IRS3. *Publications of the Astronomical Society of Japan*, 54(6):951–961, 2002.